

# DISSERTATION

submitted to the  
Combined Faculty of Natural Sciences and Mathematics  
of the University of Heidelberg, Heidelberg, Germany  
for the degree of  
Doctor of Natural Sciences (Dr. rer. nat.)

presented by  
**Dipl.-Chem. Alexander Efremov**  
born in Abakan, Krasnoyarskiy Kray, Russia

Oral examination: 13<sup>th</sup> of June, 2014



# **Fabrication and application of hydrophilic-hydrophobic micropatterned polymer surfaces**

The dissertation was carried out at the  
**Institute of Applied Physical Chemistry**  
University of Heidelberg, Heidelberg, Germany

and reviewed by  
**Prof. Dr. Michael Grunze**  
Institute of Applied Physical Chemistry, University of Heidelberg  
**Prof. (apl.) Dr. Hans-Robert Volpp**  
Institute of Physical Chemistry, University of Heidelberg

### **Published or under-preparation projects related to this thesis:**

- Efremov AN, Stanganello E, Welle A, Scholpp S, Levkin PA. Micropatterned superhydrophobic structures for the simultaneous culture of multiple cell types and the study of cell-cell communication. *Biomaterials*. 2013, 34: 1757-1763.
- Efremov AN, Grunze M, Levkin PA. Digital liquid patterning: a versatile method for maskless generation of liquid patterns and gradients. *Advanced Materials Interfaces*. 2014. DOI: 10.1002/admi.201300075, *epub ahead of print*.
- Efremov AN, Grunze M, Levkin PA. Anisotropically wettable surfaces for direct liquid patterns generation. *Advanced Materials Interfaces*. 2014 (in preparation).

### **Other contributions as a Ph.D. student:**

- Nedashkivska V\*, Efremov AN\*, Braun F, Gudadhe A, Grunze M, Levkin PA. Facile fabrication of rough superhydrophilic and superhydrophobic polymer surfaces. *Langmuir*. 2014 (in preparation). \*These authors contributed equally to this study.
- Autenrieth T, Nedashkivska, Zhang P, Jaggy M, Efremov AN, Bastmeyer M, Blattner C, Levkin PA. 2014. Highly rough polymeric surfaces for prolonged maintenance of the stem cell pluripotency. *Biomaterials*. 2014 (in preparation).
- Shankara GK, Li L, Efremov AN, Levkin PA. Oxidation-responsive oligosulfide based nanoparticles activated by pathological levels of hydrogen peroxide. *Biomacromolecules*. 2014 (in preparation).



# Acknowledgements

This work was performed in the Group of Chemical Engineering and Biofunctional Materials headed by Dr. Pavel Levkin at the Institute of Applied Physical Chemistry (APC) at the University of Heidelberg and at the Institute of Toxicology and Genetics (ITG) at Karlsruhe Institute of Technology (KIT) Campus North in Eggenstein-Leopoldshafen. It was funded by a Helmholtz Association's Initiative and Networking Fund (Helmholtz-University Young Investigators Group grant VH-NG-621).

I am grateful to all the people without whom this work would not have been possible:

To my advisors Dr. Pavel Levkin and Prof. Dr. Michael Grunze. I am appreciative of having had the opportunity to come to Germany and to join the Institute of Applied Physical Chemistry, for the support and the enlightening scientific discussions that always left me with more to think about, and finally for the review of this thesis. Many thanks also to Prof. Dr. Hans-Robert Volpp, for agreeing to be the second referee of this work and for the strong consideration.

To Dr. Pavel Levkin, for being a good PI whose door was always open and to whom I was always excited to come with new data and ideas, for supporting and keeping track of my work as well as for introducing me to the field of material science, polymer chemistry and physical methods of polymer characterization. For his patience and willing to provide an eye-opening view, a clever solution, or a much-needed reality check.

To my lab members: Victoria Nedashkivska, Erica Boles, Girish Shankara, Linxian Li, Junsheng Li, Xin Du and Wenqian Feng for permanent help and collaborative spirit. I am particularly grateful to Victoria, Erica and Girish for discussions of scientific problems.

To Dr. Alexander Welle at the Institute of Functional Interfaces at KIT, for being an excellent collaborator in ToF-SIMS measurements as well as a patient technical advising committee member and colleague always ready to talk and to help.

To Dr. Steffen Scholpp and his PhD student Dipl.-Biol. Eliana Stanganello at the Institute of Toxicology and Genetics at KIT, for helping with the cell experiments for visualization of Wnt protein propagation as well as for interesting conversations.

And finally to my mother Valentina, my father Nikolai and grandmother Evgenija for their unconditional love and emotions, all phone and skype calls, care packages and support as well as for providing a happy home to come back to.

# Summary

Surface patterning is important in a wide spectrum of applications ranging from microelectronics, sensors design and material science to high throughput screening, tissue engineering and cell biology. A number of methods for specific patterning applications, such as photolithography, soft lithography, or electron beam and dip-pen nanolithography, have been developed. However, there is still a clear need for the development of novel methods permitting patterning of different cell types, nano- and microparticles as well as hydrogels incorporating cells. These novel patterning methods are vital for the advancement of such research fields as tissue engineering, biomaterials and for fundamental investigation of cell-cell communication, tissue and organ development.

The aims of this PhD thesis were: a) develop a technique for creating droplets of liquid with defined geometries that can be used for patterning water soluble components; b) optimize the conditions for the fabrication of porous polymer surfaces for the liquid patterning; c) characterize the produced patterned polymer surfaces; d) further develop the technique for maskless generation of liquid patterns with arbitrary geometry; e) optimize the method for the patterning of different materials (chemicals, hydrogels, microparticles); f) show an application of the method for patterning of living cells and characterize their behavior on the composite surface during cultivation; g) show an application of the technology to mimic natural cell-cell communication *in vitro* via signaling protein propagation between patterned cell populations in co-culture.

The first part of the work was devoted to the development of porous polymer layers with precise micropatterns of hydrophilic and hydrophobic areas. In order to fabricate these patterns, UV-initiated photografting of 2,2,3,3,3-pentafluoropropyl methacrylate (PFPPMA) on porous poly(2-hydroxyethyl methacrylate-*co*-ethylene dimethacrylate) (HEMA-EDMA) was optimized. Before and after photografting, both polymer substrates were thoroughly characterized using water contact angle measurement, UV-Vis spectroscopy, scanning electron microscopy (SEM) and time of flight secondary ion mass spectrometry (ToF-SIMS). Porous properties were characterized by UV-Vis spectroscopy, SEM and dynamic light scattering techniques (DLS). Due to the high difference in wettability of the hydrophilic HEMA-EDMA polymer film and hydrophobic regions coated with PFPPMA polymer brushes, aqueous solutions can be trapped in the hydrophilic areas, taking the shape of these areas. The transparency of the HEMA-EDMA monolith originated from porous properties of the polymer makes it suitable for microscopic monitoring of liquid patterns during experiments.

The method was for the first time applied for the simultaneous micropatterning of multiple cell types. More than ten different cell populations separated by hydrophobic borders could be cultured in microreservoirs. After adhesion, the cells could be placed in the mutual culture medium, allowing cell-cell communication among populations. During 3 days co-culture in the mutual medium, cross-contamination was shown to be less than 1,5%, although the cells were pre-patterned in the hydrophilic areas separated by hydrophobic borders of only two to three cell diameters. The capability of cell patterning and long term cultivation opens the way for many interesting bio-applications, such as *in*

*vitro* mimicking important biological processes that involve and depend on the organization of multiple cell types into complex micropatterns *in vivo*. As a case study, I together with Dr. Steffen Scholpp and Dipl. Eliana Stanganello (ITG, KIT) used the developed technique to visualize spreading of signaling molecules (Wnt protein) from one micropatterned population of fibroblast cells to another fibroblast population by activation of the reporter system. Thus, we were able to simulate paracrine signaling system *in vitro*.

In addition, I further developed our technique into a new type of mask-less liquid patterning or *digital liquid patterning* (DLP) method. The idea of this method is similar to the working principle of a digital score board. A digital score board consists of many small bulbs, which generate light symbols on it. In the case of DLP, instead of the bulbs, small liquid droplets (digits) form a more complex liquid pattern on a substrate. The substrate for DLP is a composite surface, consisting of a grid of hydrophilic HEMA-EDMA spots divided by hydrophobic PFPMA barriers. The method allows on-demand fabrication of liquid patterns without the need to change the substrate and use an additional photomask. Patterns with customized geometries can be prepared manually by simply pipetting liquid inside the spots and successively coalescing the generated droplets to form a liquid micropattern. The DLP does not require clean room or high-precision microfabrication and allows the manual positioning of microdroplets in the range of micrometer scale. It was also shown that using superhydrophilic/superhydrophobic patterned surfaces leads to spontaneous dewetting of the coalesced microdroplets on the interface of the superhydrophobic border and the superhydrophilic spot. Hence, the usage of hydrophilic/hydrophobic patterned surface ensures the stability of liquid patterns during manipulations. Furthermore, the developed technique enables patterning of not only solutions, e.g. different chemicals, but also suspensions of living cells and microparticles, hydrogels, or formation of liquid multi-component gradients with complex geometries. Thus, this method will be especially useful for biological studies, which require the generation of complex patterns of different or the same cell types, or bioactive materials and cellular gradients without the need for sophisticated microfluidic and printing equipment, or for designing additional masks.

# Zusammenfassung

Oberflächenstrukturierung finden Anwendung in einem breiten Spektrum von Technologien: Mikroelektronik, Sensoren, Design- und Materialforschung bis hin zu Hochdurchsatz-Screening, Gewebe-Engineering und Zellbiologie. Trotz einer großen Vielfalt von Methoden für spezielle Strukturierungsanwendungen, wie zum Beispiel Photolithographie, Soft Lithography oder Elektronenstrahl- oder Dip-Pen-Nanolithographie, besteht immer noch ein großes Interesse an der Entwicklung neuer Verfahren, die die Strukturierung von verschiedenen Zelltypen, von Nano- und Mikropartikeln sowie von Hydrogelen- in die Zellen eingebunden werden können- erlauben. Diese neuen Strukturierungsverfahren sind entscheidend für die Weiterentwicklung der Forschungsfelder Tissue Engineering, Biomaterialforschung und Grundlagenforschung an Zell-Zell-Kommunikation, Gewebe- und Organentwicklung.

Die Ziele dieser Dissertation waren: a) Entwicklung einer Technik zum Erzeugen von flüssigen Oberflächen mit definierten Geometrien, die für die Strukturierung wasserlöslicher Komponenten verwendet werden können, b) Optimierung der Bedingungen für die Herstellung von porösen Polymeroberflächen für Strukturierung von Flüssigkeiten, c) Charakterisierung der hergestellten strukturierten Polymeroberflächen, d) Weiterentwicklung der Technik für die maskenlose Herstellung von flüssigen Mustern mit beliebiger Geometrie, e) Optimierung der Methode für die Strukturierung von unterschiedlichen Materialien, f) Entwicklung dieser Methode Immobilisierung von lebenden Zellen und Charakterisierung ihres Verhaltens auf der strukturierten Oberfläche während der Kultivierung, g) Anwendung der Technologie zur Modellierung der natürlichen Zell-Zell-Kommunikation *in vitro* durch Ausbreitung eines Signalproteins zwischen strukturierten Zellpopulationen in der entsprechenden Co-Kultur.

Der erste Teil der Arbeit ist die Entwicklung von porösen Polymerschichten mit präzisen Mikrostrukturen, die aus hydrophilen und hydrophoben Bereichen zusammengesetzt sind. Für die Herstellung dieser Strukturen wurde UV-initiiertes Photografting von 2,2,3,3,3-Pentafluorpropylmethacrylat (PFPPMA) auf porösem Poly(2-hydroxyethylmethacrylat-co-ethylen-dimethacrylat) (HEMA-EDMA) optimiert. Vor und nach dem Photografting wurden beide Polymersubstrate durch Kontaktwinkelmessung, UV-Vis-Spektroskopie, Rasterelektronenmikroskopie (REM) und Flugzeit-Sekundärionenmassenspektrometrie (ToF-SIMS) umfassend charakterisiert. Poröse Eigenschaften wurden durch UV-Vis-Spektroskopie, REM und dynamische Lichtstreuung (DLS) charakterisiert. Aufgrund der sehr unterschiedlichen Benetzbarkeit zwischen dem hydrophilen HEMA-EDMA Polymerfilm und den mit polymeren Bürsten aus PFPPMA bedeckten hydrophoben Bereichen können wässrige Lösungen in den hydrophilen Bereichen eingeschlossen werden. Die auf den porösen Eigenschaften des Polymers basierende Transparenz des HEMA-EDMA Monoliths ermöglicht die mikroskopische Beobachtung der flüssigen Strukturen während der Experimente.

Die Methode wurde zum ersten Mal für die gleichzeitige Aufbringung von mehreren Zelltypen nebeneinander mittels Verwendung von Mikrostrukturen eingesetzt. Mehr als zehn, durch hydrophobe Grenzen getrennte, verschiedene Zellpopulationen

konnten in Mikroreservoiren kultiviert werden. Nach Adhäsion wurden die Zellen im gemeinsamen Kulturmedium aufbewahrt, um die Zell-Zell-Kommunikation zwischen den Populationen zu gewährleisten. Während der dreitägigen Co-Kultur im gemeinsamen Medium wurde gezeigt, dass die gegenseitige Kreuzkontamination weniger als 1,5 % betrug, obwohl die Zellen in den hydrophilen Bereichen durch hydrophobe Grenzen von nur zwei bis drei Zelldurchmessern durch vorherige Mikrostrukturierung voneinander getrennt worden sind. Die Fähigkeit der Zell-Strukturierung und Langzeitkultivierung eröffnet den Weg für viele interessante biologische Anwendungen, wie zum Beispiel die *in vitro*-Modellierung wichtiger biologischer Prozesse, die auf der Organisation von mehreren Zelltypen *in vivo* auf komplexen Mikrostrukturen basieren. Als Fallstudie haben ich zusammen mit Dr. Steffen Scholpp and Dipl. Eliana Stangannello (ITG, KIT) die entwickelte Technik zum Visualisieren der Ausbreitung von Signalmolekülen (Wnt-Protein) von einer mikrostrukturierten Population von Fibroblasten zu einer anderen Fibroblasten-Population durch die Aktivierung des Reportersystems eingesetzt. So konnten wir ein parakrines Signalsystem *in vitro* simulieren.

Darüber hinaus habe ich die Technik zu einer neuen Art der maskenfreien flüssigen Strukturierung oder zur digitalen flüssigen Strukturierungsmethode (Digital Liquid Patterning, DLP) weiter entwickelt. Die Idee dieser Methode ähnelt dem Funktionsprinzip einer digitalen Anzeigetafel. Eine digitale Anzeigetafel besteht aus vielen kleinen Glühbirnen, worauf Licht-Symbole generiert werden. Im Fall von DLP bilden anstelle der Glühbirnen kleine flüssige Tropfen (Ziffern) ein komplexes flüssiges Muster auf einem Substrat. Das Substrat für DLP ist eine zusammengesetzte Oberfläche, bestehend aus einem Netz von hydrophilen HEMA-EDMA Spots, die durch hydrophobe PFPMA Barrieren voneinander getrennt sind. Das Verfahren ermöglicht eine Maßherstellung von flüssigen Mustern, ohne dass Änderung des Substrats oder eine zusätzliche Fotomaske notwendig sind. Muster mit individuellen Geometrien können durch einfaches Pipettieren von Flüssigkeit in die Spots und späteres Verbinden der erzeugten Tropfen, um eine flüssige Mikrostruktur zu bilden, manuell erzeugt werden. Die DLP erfordert weder einen Reinraum noch hochpräzise Mikroherstellung. Die manuelle Positionierung von Mikrotröpfchen liegt im Bereich der Mikrometerskala.

Es wurde auch gezeigt, dass die Verwendung von superhydrophil/superhydrophob strukturierten Oberflächen zur spontanen Entnetzung der verbundenen Mikrotröpfchen auf der Grenzfläche zwischen der superhydrophoben Barriere und des superhydrophilen Spots geführt hat. Daher sichert die Verwendung von hydrophil/hydrophob strukturierten Oberflächen die Stabilität der flüssigen Strukturen während der Anwendungen. Weiterhin ermöglicht das entwickelte Verfahren nicht nur die Strukturierung von Lösungen, z.B. von verschiedenen Chemikalien, sondern auch von Suspensionen lebender Zellen und Mikropartikel, Hydrogelen, oder zur Bildung von flüssigen Mehrkomponenten-Gradienten mit komplexen Geometrien. Somit ist dieses Verfahren besonders nützlich für biologische Untersuchungen, die die Erzeugung von komplexen Mustern von verschiedenen oder gleichen Zelltypen oder bioaktiven Materialien und Zell-Gradienten, ohne dass anspruchsvolle Mikrofluidik- und Druckausstattung oder zusätzliche Masken benötigt werden.

# Table of Contents

Acknowledgements .....	i
Summary.....	ii
Zusammenfassung .....	iv
Table of Contents .....	vi
List of Figures.....	viii
List of Tables.....	xi
List of Abbreviations.....	xii
List of Symbols.....	xiii
Chapter 1 .....	1
Introduction: surface patterning technologies .....	1
1.1 Microscale surface patterning technologies .....	1
1.1.1 Photolithography .....	1
1.1.2 Soft lithography .....	2
1.1.2.1 Microcontact printing .....	3
1.1.2.2 Microfluidics .....	4
1.1.2.3 Stencil-assisted surface patterning .....	5
1.2 Nanoscale surface patterning technologies.....	9
1.2.1 Electron beam lithography.....	9
1.2.2 Electron beam chemical lithography .....	9
1.2.3. Scanning probe lithography.....	10
1.2.4 Dip-pen nanolithography .....	11
1.3 Aim and objectives of this work.....	15

Chapter 2 .....	17
Materials and Methods .....	17
2.1 Materials .....	17
2.2 Fabrication of hydrophobic/hydrophilic patterned surfaces.....	17
2.3 Scanning electron microscopy.....	21
2.4 Measuring water contact angle and water dispensing/withdrawing experiments .....	21
2.5 Measuring time and rate of droplet evaporation.....	22
2.6 Time-of-flight secondary ion mass spectrometry.....	22
2.8 UV-NIR transmittance spectroscopy.....	23
2.10 Cell cultures.....	24
2.11 Cell patterning .....	24
2.12 Cell proliferation assay.....	25
2.13 Cross-contamination assay .....	25
Chapter 3 .....	27
Fabrication and characterization of a hydrophilic-hydrophobic micropatterned surface for generation of liquid patterns .....	27
3.1 Summary.....	27
3.2 Introduction .....	28
3.3 Fabrication of hydrophilic/hydrophobic patterned surfaces.....	31
3.4 Generation of liquid patterns .....	33
3.5 Microscale morphology of hydrophilic/hydrophobic patterned surfaces.....	36
3.6 Chemical composition of hydrophilic/hydrophobic patterned surfaces.....	38
3.7 Influence of porogen content on the porous structure of HEMA-EDMA monoliths	41
3.8 Influence of porous structure on transparency of HEMA-EDMA polymer films.....	46
3.9 Influence of porous structure on the wetting properties of HEMA-EDMA polymer films.....	53
3.10 Optimization of the photografting procedure .....	54
Chapter 4 .....	59

Micropatterned structures for the simultaneous culture of Multiple Cell Types and the Study of Cell-Cell Communication .....	59
4.1 Summary.....	59
4.2 Introduction .....	59
4.3 Cell patterning procedure .....	61
4.4 Cross-contamination of cell patterns during co-culturing .....	63
4.5 Mimicking Wnt-signaling system <i>in vitro</i> .....	65
4.6 Conclusions .....	67
Chapter 5 .....	68
Digital Liquid Patterning: A Versatile Method for Maskless Generation of Liquid Patterns and Gradients.....	68
5.1 Summary.....	68
5.2 Introduction .....	68
5.3 Experimental Details .....	69
5.4 Results and Discussion.....	83
5.5 Conclusions .....	87
Chapter 6 .....	89
Conclusion and outlook.....	89
Bibliography.....	91

# List of Figures

1.1	Microscale surface patterning techniques.....	7
1.2	Nanoscale surface patterning techniques.....	13
2.1	Chemical structures of reactants.....	18
2.2	Schematics of reactions in fabrication of patterned surfaces.....	19
2.3	Fabrication of HEMA-EDMA polymer layer.....	20
3.1	Liquid patterning approach based on using hydrophilic/hydrophobic patterned surfaces.....	28
3.2	Liquid patterning based on using superhydrophilic/superhydrophobic patterned surfaces.....	30
3.3	Liquid patterning based on micropatterned structures with undercut edges.....	30
3.4	Schematic description of a pattern fabrication procedure.....	32
3.5	Schematic description of the generation of liquid patterns. Static and dynamic water contact angles of patterned surface.....	34
3.6	Influence of the width of hydrophobic borders on the stability of adjacent liquid patterns .....	35
3.7	Patterned surfaces and corresponding SEM micrographs.....	37
3.8	Photograph of a hydrophilic/hydrophobic micropatterned substrate and corresponding $C_3H_2F_5O^-$ -ion ToF-SIMS images.....	39
3.9	Mass spectra $C_3H_2F_5O^-$ signals obtained from hydrophilic and hydrophobic regions of patterned surface.....	39
3.10	ToF-SIMS cross-sectional images of 100 $\mu\text{m}$ -wide PFPMA hydrophobic border after 1 min and 15 min photografting.....	41
3.11	SEM micrographs of HEMA-EDMA polymer monoliths with different content of porogens in the polymerization mixture.....	44
3.12	Size distribution of the scattering particles in HEMA-EDMA monoliths with different content of porogens in the polymerization mixture.....	45

3.13 Gaussian curves approximating size distributions of polymer particles in the bulk monoliths obtained from the polymerization mixtures 1–6.....	46
3.14 Coordinate geometry for Rayleigh and Mie scattering.....	47
3.15 UV-NIR transmission spectra of HEMA-EDMA polymer films in air.....	50
3.16 UV-NIR transmission spectra of HEMA-EDMA polymer films in water.....	51
3.17 Photographs showing relative transparency of HEMA-EDMA layers obtained from mixtures 1-6 on glass supports.....	52
3.19 Photographs of water droplets on HEMA-EDMA layers obtained from the polymerization mixtures 1-6.....	53
3.20 Photographs of water droplets on HEMA-EDMA substrate after photografting for different time intervals.....	55
3.21 Mass spectra $\text{CHO}_2^-$ and $\text{C}_3\text{H}_2\text{F}_5\text{O}^-$ peaks and corresponding peak areas from the samples impregnated with the photografting mixture.....	56
3.22 Mass spectra $\text{CHO}_2^-$ peaks and corresponding peak areas from the samples with $\text{H}_2\text{O}$ -tBu (1 <sub>v</sub> :1 <sub>v</sub> ) mixture.....	57
4.1 Cell patterning procedure.....	60
4.2 Cell viability on HEMA-EDMA polymer.....	62
4.3 Trajectories of HeLa-EGFP cells on HEMA-EDMA and polystyrene surfaces for 24 h.....	63
4.4 Cross-contamination of cell patterns during co-culturing.....	65
4.5 Simulation of paracrine signaling system <i>in vitro</i> .....	66
5.1 Digital liquid patterning.....	70
5.2 Withdrawing of water droplet from two hydrophilic spots divided by superhydrophobic or hydrophobic barriers.....	70
5.3 Dispensing of water to hydrophilic spot next to another one divided by hydrophobic barriers of different width.....	72
5.4 Dispensing of water to hydrophilic spot surrounded by hydrophobic barriers of different width.....	73
5.5 Schematics illustration of sessile droplet and its geometrical parameters.....	74
5.6 Models of conformational changes of evaporating droplet.....	77
5.7 Shape of evaporating droplets placed on hydrophilic spots with different geometries as a function of time.....	78
5.8 Time-dependences of normalized contact angle and volume. Dependence of contact angle function on contact angle of the evaporation water droplet.....	80

5.9 Digital liquid patterning: examples of applications.....	84
5.10 Generation of single and multiple concentration gradients inside surface tension-confined liquid channels formed by the digital liquid patterning method.....	85

# List of Tables

1.1 Comparison of the commonly used microscale surface patterning techniques.....	8
1.2 Comparison of the commonly used nanoscale surface patterning techniques.....	14
2.1 Dependence of the time and rate of the droplet evaporation on the geometry and area of hydrophilic spots.....	22
3.1 Content of polymerization mixtures used for preparation of HEMA-EDMA monoliths.....	42
3.2 Porous properties of HEMA-EDMA monoliths.....	43
3.3 Comparison of the light transmission by polymer particles obtained experimentally and estimated by using the theoretical approximation. Samples are in air.....	50
3.4 Comparison of the light transmission by polymer particles obtained experimentally and estimated by using the theoretical approximation. Samples are in water.....	51
3.5 Static WCAs of HEMA-EDMA polymer layers prepared with different content of porogens in the polymerization mixture.....	55
4.1 Parameters of HeLa-EDFP cell motility on HEMA-EDMA and polystyrene substrates.....	63
5.1 Comparison of the experimental time of droplet evaporation with the results estimated by using theoretical approximations of the contact angle function.....	82
5.2 Comparison of the rate of droplet evaporation obtained experimentally with results estimated by using theoretical approximations of the contact angle function.....	82

# List of Abbreviations

AFM – atomic force microscope

BIBB – 2-bromoisobutyryl bromide

DNA – deoxyribonucleic acid

DPN – dip-pen nanolithography

EBCL – electron beam chemical lithography

e-beam – electron beam

EBL – electron beam lithography

HEMA-EDMA – poly(2-hydroxyethyl methacrylate-*co*-ethylene dimethacrylate)

MilliQ water – deionized water (resistivity 18.2 M $\Omega$ ·cm at 25 °C)

NBT – 4-nitro-1,1-biphenyl-4-thiol

NIR – near-infrared

OTS – octa(decyltrichloro)silane

PDMS – poly(dimethylsiloxane)

PFPPMA – 2,2,3,3,3-pentafluoropropyl methacrylate

PNIPAM – poly(*N*-isopropyl acrylamide)

SAM – self-assembled monolayer

SEM – scanning electron microscopy

SPL – scanning probe lithography

STM – tunneling microscope

ToF SIMS – time-of-flight secondary ion mass spectrometry

UV – ultraviolet

Vis – visible

WCA – water contact angle

$\mu$ CP – microcontact printing

# List of Symbols

- $a_k, b_k$  – coefficients of Mie scattering parameters
- $i_1$  – vertically paralyzed Mie scattering parameter
- $i_2$  – horizontally paralyzed Mie scattering parameter
- $\Psi_k, \xi_k$  – Ricatt-Bessel functions
- $C$  – vapor concentration
- $\bar{C}$  – capacitance of equiconvex lens
- $C_a$  – ambient vapor concentration
- $C_s$  – saturated vapor concentration
- $d$  – diameter of particle
- $D$  – molecular diffusion coefficient
- $f(\theta)$  – contact angle function
- $h$  – height of an open liquid channel
- $H$  – droplet height
- $I$  – intensity of transmitted light
- $I_0$  – intensity of incident light
- $L$  – distance to a scattering particle
- $l$  – length of an open liquid channel
- $m$  – mass
- $M_s$  – molecular mass of solvent
- $n$  – relative refractive index
- $n_m$  – refractive index of the medium
- $n_p$  – refractive index of scattering particle
- $\theta_{adv}$  – advancing water contact angle
- $\theta_{rec}$  – receding water contact angle
- $\theta_{st}$  – static water contact angle
- $Q$  – net diffusive flux
- $\bar{R}$  – ideal gas constant

$R_d$  – radius of droplet  
 $R_s$  – spherical radius  
 $S_d$  – surface area of droplet  
 $T$  – temperature  
 $t$  – time  
 $V$  – droplet volume  
 $\tilde{V}$  – molar volume  
 $w$  – width of an open liquid channel  
 $\alpha$  – dimensionless size parameter of scattering particle  
 $\eta_s$  – solvent viscosity  
 $\Phi$  – scattering angle  
 $\theta_0$  – the contact angle of the smooth surface  
 $\theta_{app}$  – apparent water contact angle  
 $\pi_k, \tau_k$  – angular functions of Mie scattering parameters  
 $\rho$  – liquid density  
 $\psi$  – the angle of the undercut edge  
 $\varphi_s$  – association factor of solvent with solute  
 $\lambda$  – light wavelength  
 $J_{k+1/2}$  – half-integer-order Bessel function  
 $H_{k+1/2}$  – half-integer-order Henkel function

# Chapter 1

## Introduction: surface patterning technologies

### Summary

Recent advantages in the development of new surface patterning technologies have created unique opportunities for the fabrication of a variety of micro- to nanometer surface structures. The ability to create surface structures with dimensions from nano to micrometers makes a wide spectrum of chemical, biological and topographical patterns possible. Microelectronics, sensors, mechanical and optical devices, can benefit from the availability these techniques. This chapter briefly introduces the principles of the major and widely used micro- and nanopatterning technologies currently used to fabricate surface patterns of various materials with well-defined geometry in the range from several hundred micrometers to few nanometers. The advantages, limitations and applications for each surface patterning technology are discussed. The low cost, availability, outstanding performance and compatibility with delicate materials make the presented technologies desirable and widespread in industry and science.

## 1.1 Microscale surface patterning technologies

### 1.1.1 Photolithography

Photolithography is the most commonly utilized microfabrication technique and has been actively used in the microelectronics industry [1, 2]. Nonetheless, photolithographic is also considered as a microfabrication tool in routine research laboratories (Table 1.1). In the photolithography process, patterns are generated when features on a mask are transmitted to a substrate by exposure to light (Fig. 1.1 A). The substrate is first coated

with a material that is sensitive to radiation (polymers [1, 3], metal oxides [4], quartz [1], glass [1, 5], hydrogels [6]), known as a photoresist. Then, the photoresist is selectively irradiated through the photomask, which consists of transparent and non-transparent areas. Typical photomasks are made of optically transparent materials at the wavelength used for patterning and can be produced using computer-aided-design software. Depending on the properties of the photoresist, the polymer chains can either break or become cross-linked in the irradiated areas, making them soluble or insoluble, respectively, to particular solvents (so-called development solutions). The first kind of resist is known as positive resist, the second as negative resist. After the substrate is immersed in the resist development solution, the pattern on the surface is either an identical replica of the mask template (positive resist) or its complimentary geometrical image (negative resist). The photoresist can also be removed from the substrate by using suitable solvents or plasma treatment if required [7, 8].

Conventional photolithographic processing occurs in a clean room and requires expensive equipment. Therefore the process can be cost prohibitive, if such facilities are not readily accessible. In addition, photolithography is also well suited for surface patterning of substrates that have been functionalized with delicate ligands. Photolithography enables feature sizes on the order of 100 nm and can be used to create various patterns over large surface areas [9-11]. To overcome some shortcomings, such as requirements for clean room and the resolution limit of conventional photolithography, new photolithographical techniques have emerged, such as transparency-based photolithography [6], projection photolithography [12, 13], extreme ultraviolet lithography [14-17] and interference lithography [18-21]. For instance, transparency-based photolithography does not require the use of a clean room and is less expensive as transparencies are created using standard ink jet printers. Interference lithography relies on the use of light interference pattern projected onto a photoresist and allows creating nanoscale resolution (down to 11 nm) [18-20].

### **1.1.2 Soft lithography**

“Soft lithography” is a group of surface patterning techniques based on non-lithographic strategies utilizing elastomeric (“soft”) materials [22, 23]. The main members of the soft lithography family are microcontact printing, microfluidics and stencil-assisted techniques. All these techniques take advantages of either printing or molding with elastomeric stamps [23]. The elastomeric pattern (stamp, mold or stencil) is fabricated in

bas-relief from a replica mold, the so-called master created prior via microfabrication. The transfer of the shape and form to the elastomer is ensured by the rigidity of the master, which allows for its separation from the produced pattern. Hence, the elastomeric pattern, typically poly(dimethylsiloxane) (PDMS), represents an inverted replica of the master structure, which can have a wide range of geometries [8].

The primary advantage of soft lithography is that elastomers can generate a conformal contact at the molecular level over large areas of diverse substrates. Tight mechanical contact is even possible with curved surfaces [22]. In addition, the sealing between the material of interest and the elastomeric pattern is mediated by van der Waals forces and therefore reversible. This ensures that the procedure could be repeated several times using the same mold, stamp, or stencil [7]. Moreover, soft lithography is a low-cost and high-throughput technique that does not require clean rooms to produce high-quality patterned micro- and nanostructures. It overcomes the resolution limits imposed upon photolithography by optical diffraction. Furthermore, widely used PDMS elastomer is suitable for biological applications, as it is stable at temperatures ranging from 37 to 95°C, chemically inert and biocompatible [24], as well as optically transparent, minimally autofluorescent and gas-permeable [25]. The following sections represent the most commonly used members of soft lithography family such as microcontact printing, microfluidics and stencils-assisted patterning.

### **1.1.2.1 Microcontact printing**

Microcontact printing ( $\mu$ CP) is the most widely used soft lithography technique.  $\mu$ CP was invented in the early 1990s by Kumar and Whitesides, who used elastomeric stamps made of PDMS with micrometer sized relief structures for the patterned transfer of alkanethiols on gold-coated silicon surfaces [26]. Originally developed for creating patterns for microelectronics applications [1],  $\mu$ CP soon found extremely widespread applications in physics, chemistry and biology [23, 27, 28] (Table 1.1).  $\mu$ CP technology is suitable for the direct surface patterning of small, surface-active molecules, polymers, or biomaterials onto spatially and geometrically well-defined areas of a substrate by mechanical contact (Fig. 1.1 B).

This technique requires an inking step to transfer the molecules of interest to an elastomeric stamp. The excess solution is then dried and the remaining layer at the surface of the stamp is placed in conformal contact with the surface of the target material. The conformal contact can last from a few seconds to minutes. Afterwards, the stamp is peeled

off, leaving a surface pattern of the molecules of interest on the substrate. The bonds that connect the transferred molecules and the surface of the target material can be either non-covalent or covalent, depending on the molecules and surface functionality involved. The surrounding unmodified areas can be subsequently backfilled with other molecules of interest.

For example, an elastomeric stamp is immersed in a thiol solution for inking and then carefully placed on a gold-coated substrate. Since thiols form strong metal-sulfur bonds with gold, printing results in self-assembled monolayers (SAMs) of alkanethiols on the metal only in the areas of conformal contact [29]. Being an additive process, the material losses incurred in contact printing are minimal in comparison with techniques such as subtractive printing.  $\mu$ CP methods additionally take advantage of the reusability of the photomask and flexibility of the stamp to serve as a versatile, low cost, high-throughput patterning technique that allows working with a wide spectrum of patterning materials (Table 1.1) as well as using different substrates varying from metals [26, 30], glass slides [31, 32], silicon oxide [33] to polymers [34] and hydrogels [35, 36].

PDMS is the commonly used elastomer for the fabrication of  $\mu$ CP stamps. The Young's modulus of fully cross-linked PDMS is usually in the low MPa range that is suitable to achieve conformal contact but may reduce the pattern resolution. In order to obtain high-resolution patterns in the submicrometer range, without any distortions, new types of elastomers were successfully developed, including hard-PDMS [37], polyolefin plastomers [38], perfluoropolyethers [39], poly(methyl methacrylate) stamps [40] and poly(ethylene)/poly(methyl methacrylate) composite stamps [41].

### **1.1.2.2 Microfluidics**

Microfluidic channels can be also used for patterning. This method is based on the formation of microchannels on the surface of the target material. Elastomeric molds are often used to fabricate such microchannels with desired geometries. The mold is then pressed and fixed on the substrate of interest, followed by filling the formed microchannels with a solution of the desired molecules to be patterned (Fig. 1.1 C) [42, 43], [44]. The bond between the mold and target material can be either reversible or irreversible. Microfluidic patterning can be particularly useful as an alternative to  $\mu$ CP if a drying step can damage sensitive molecules, or when close control over the molecular density of the immobilized component in the material surface is a key requirement.

Microfluidic patterning combines the advantages of being a parallel and additive technique. In addition, spatially separated, elastomeric microchannels allow different solutions to flow over different regions of the same sample to generate multi-component patterns [8, 44, 45] (Table 1.1). Another interesting attribute is the laminar flow inside the microchannels. Moreover, several laminar streams flowing parallel to each other can be combined into one microscale size stream without intermixing. As it was mentioned the elastomeric molds are easily fabricated and widely available, making microfluidics a cost effective technology for surface patterning [46]. One of the drawbacks of this technique is the difficulty to create multiple-interconnected channels, limiting the diversity of possible surface patterns. Another difficulty is that spontaneous filling of microchannels *via* capillary forces is a relatively slow process limited to small microfluidic structures. However, the wide use of external pumping devices with controlled flow rates, down to nanoliters per minute, has successfully addressed the latter problem.

### 1.1.2.3 Stencil-assisted surface patterning

An elastomeric microstencil is a membrane that is structured with through-holes of the desired size and geometry. Microstencils are usually made of PDMS. The softness and elasticity of PDMS microstencils result in them to spontaneously seal to any smooth surface. When a microstencil is brought in conformal contact with a surface, the molecules of interest can be adsorbed onto the unprotected areas [47, 48], or plasma treatment can be used to selectively modify the exposed surface [49]. However, the areas outside the holes remain intact (Fig. 1.1 D). After the surface modification process is finished, the microstencil is manually lifted off. One of the main drawbacks of the PDMS microstencils is that they cannot be reused, since they are stretched and deformed during the peel-off process. New materials have been proposed as alternatives to PDMS, such as parylene-C stencils [50] or hybrid elastomer metal stencils [51], which can be reused. Parylene-C microstencils are free-standing and rigid, which allow for creating well defined and regular surface patterns. However, parylene-C microstencils do not enable the formation of a conformal contact. Therefore, a liquid confinement is dependent on the hydrophobic properties of both the substrate surface and the microstencils. This limits their application to hydrophobic surfaces, preventing, for example, the use of clean glass as a substrate. To overcome this limit, hybrid microstencils made of steel with elastomeric O-gaskets around the microstencil apertures have been created as a more versatile alternative, allowing for fabrication of patterns on both hydrophobic and hydrophilic surfaces. Additionally, rigid

nanostencils made of silicon have been widely used to create surface nanopatterns of different materials, ranging from metals and semiconductors to proteins [52-57]. Although the stencils-assisted surface patterning requires some technical skills to align the flexible stencil on the surface (with respect to electrodes or underlying chemical patterns) and ensure an adequate sealing, the replication technique is relatively simple, large scale and cost-effective. The stencil-assisted surface patterning has two significant advantages. First, it is compatible with virtually any substrate material (metals, semiconductors, polymers) as well as curved surfaces. Second, the absence of organic solvents makes it an attractive approach for the immobilization of delicate molecules [1].

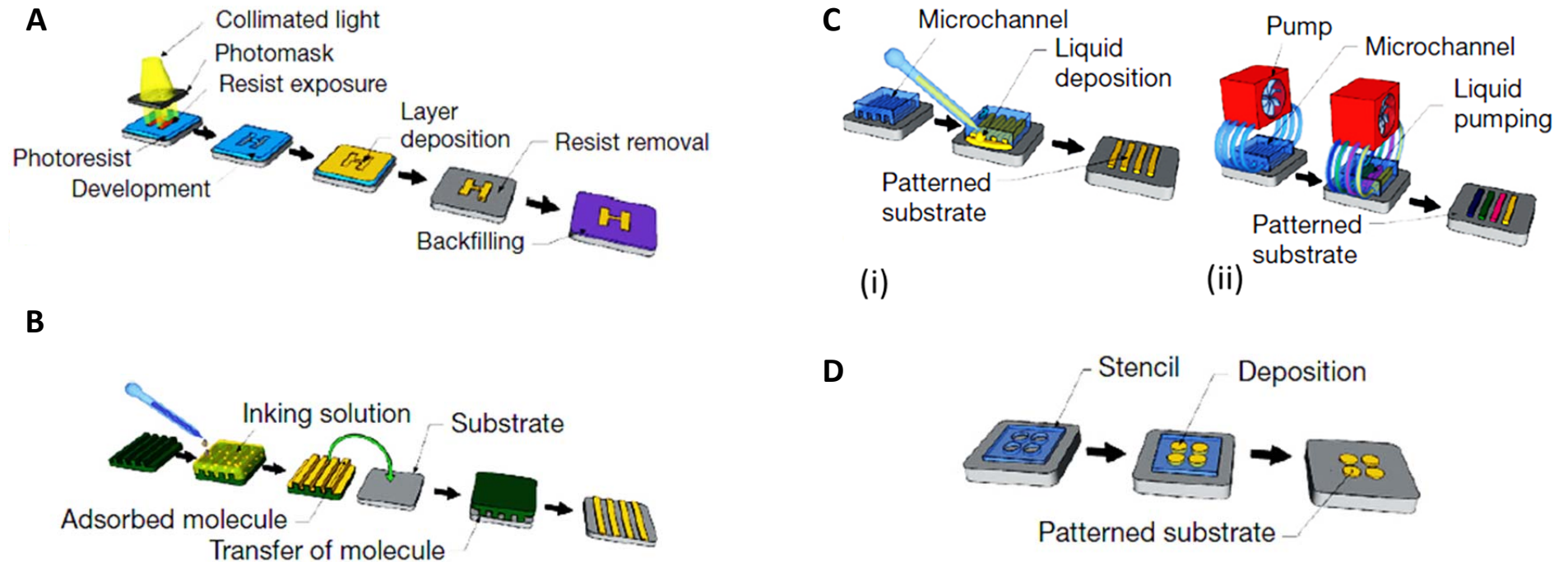


**Fig. 1.1.** Microscale surface patterning techniques. (A) Photolithography: a beam of light irradiates through a photomask onto the photoresist, selectively modifying it. Subsequent immersion in a development solution removes the modified areas. After that deposition and backfilling another molecule of interest can be applied to create the desired surface pattern. (B) Microcontact printing: a flexible stamp is immersed in the solution of interest and pressed onto the surface to produce surface pattern. (C) Microfluidic patterning: (i) surface patterns are generated by passively filling the microchannels with the solution of interest powered by capillary forces; (ii) surface patterns are generated by the use of pumps and tubing to deliver distinct solutions in each channel. (D) Stenciling: deposition of materials or ablation of the substrate through the holes of the micro- or nanostencils leads to the generation of desired surface patterns. [7]

**Table 1.1.** Comparison of the commonly used microscale surface patterning techniques.

Technique	Description	Advantages	Limitations	Applications
Photolithography	Photo irradiation of a photosensitive substrate through a photomask	Patterning over large area. Compatible with many substrates.	Requires photosensitive substrates or chemicals. Requires photomasks.	Metals [58] Metal oxides [59] Small organic molecules [4, 60-62] Polymers [63, 64] Proteins [63, 65, 66] Cells [59, 64] Cell co-cultures [67-70]
Microcontact printing	Printing using inked elastomeric stamps	Simple implementation. Relatively cheap. Patterning over large areas.	Inability to print multiple “inks” simultaneously. Possible “ink” diffusion.	Metals [34, 71] SAMs [26, 30, 72-76] Nanoparticles [77, 78] Dendrimers [79, 80] DNA [81, 82] Lipids [83] Proteins [30, 32, 35, 74, 84-87] Cells [30, 35, 72, 74, 85, 88, 89] Cell co-cultures [90, 91]
Microfluidics	Sealing an elastomeric mold against a substrate to form a network of microchannels.	Relatively cheap. Rapid and dynamic system. Manipulation with liquids, solutions or suspensions.	Channel geometry limits pattern diversity. Limited to interconnected pattern.	SAMs [92-94] DNA [24] Peptides [93] Proteins [43, 95] Antibodies [31] Immunoglobulins [96] Cells [42, 93, 97, 98] Cell co-cultures [94, 99, 100]
Stenciling	Deposition of material through apertures of a mask.	Relatively cheap. Patterning over curved surfaces. Rapid implementation.	Simple geometry. Mechanically weak. Clogging of apertures.	Metals [52, 54, 55, 101] DNA [51] Proteins [47, 50, 51, 57] Cells [47, 49, 51] Cell co-cultures [47, 48, 50, 102, 103]

## 1.2 Nanoscale surface patterning technologies

### 1.2.1 Electron beam lithography

Electron beam lithography (EBL) is a direct writing patterning technique [104]. Originally developed for the semiconductor industry, it has been applied to pattern a wide spectrum of materials, ranging from SAMs to DNA (Table 1.2). EBL is based on focusing an electron beam (e-beam) onto a substrate covered with an electron beam photoresist under high vacuum [8] (Fig. 1.2 A). If the resist is positive, the areas exposed to the e-beam become more soluble in the development solution that removes the exposed substrate, thereby finalizing the surface pattern. If the resist is negative, the irradiated areas become insoluble in the developer solution. The resolution of this technique is determined by the size of the molecules in the resist and the scattering range of the electrons [105]. To avoid the backscattering of electrons, low electron beam energies lead to smaller feature sizes and patterns in the tens nanometer range have been fabricated [106]. Although small feature sizes can be created, the adoption of this patterning technique is limited by high costs, as compared to other lithographic approaches. In addition, the patterning speed of this technique is considerably slower than in photolithography.

### 1.2.2 Electron beam chemical lithography

An electron beam can be focused onto very small spots (<1 nm). However, in standard resist materials, the achievable resolution is not only limited by the beam size, but also by the size of the molecules in the resist and by primary and secondary electron scattering processes, namely forward scattering, backscattering, and proximity effects. Thus, novel resists should not only show a specific sensitivity to electrons, but also be thin and composed of small subunits permitting high resolution patterning. These criteria are fulfilled by SAMs with a typical thickness of 1-2 nm and an intermolecular spacing of ~0,5 nm [107]. Apart from the use of SAM as standard resist material, Grunze and colleagues [108, 109] demonstrated that terminal nitro groups can be selectively reduced to amine moieties by irradiation of 4-nitro-1,1-biphenyl-4-thiol (NBT) monolayers on gold substrates with low and high energy electrons, while the aromatic biphenyl layer is dehydrogenated and cross-linked (Fig. 1.2 B). The technique was termed Electron Beam Chemical Lithography (EBCL) because the electron irradiation resulted in a selective and quantitative chemical transformation of the nitro to amino groups [110]. It has been

assumed that the source of hydrogen atoms required for reduction of the nitro groups are generated by the electron-induced dissociation of the C-H bonds in the biphenyl moieties [108]. Chemical patterns were generated by irradiation through a mask featuring lines with a width down to 70 nm. Direct write e-beam lithography achieved 11 nm resolution lines [111]. Subsequently, these amine-terminated organic nanostructures were used as templates for surface-initiated polymerization using a surface-bound bromoisobutyryl bromide (BIBB) initiator to yield densely grafted poly(N-isopropyl acrylamide) (PNIPAM) brush surface nanopatterns [112]. Using a similar synthesis approach, sub-50 nm polystyrene brush nanopatterns were fabricated, but in this case, the NBT SAM was first patterned by EBCL followed by diazotization and coupling with methylmalonodinitrile. This resulted in surface patterns with well-defined areas of cross-linked initiator sites for polystyrene surface-induced polymerization [110].

Despite the advantages and stability of aromatic SAMs, they are not commercially available. Furthermore, the efficient nitro-to-amine transformation requires large irradiation doses of 30-40 mC/cm<sup>2</sup> making this surface patterning method a relatively time-consuming process, which is a constraint for industrial implementation of this technique. In an effort to overcome these limitations, the concept of EBCL was extended to aliphatic SAMs [113, 114]. The exposure of the aliphatic SAM to a low dose e-beam (0,5-2,0 mC/cm<sup>2</sup>) led to the fragmentation of the aliphatic thiol molecules and disorder of the SAM. These pre-patterned regions, consisting of fragmented and disordered SAM molecules, were displaced by 11-aminoundecanethiol. This exchange reaction resulted in amino-terminated 11-aminoundecanethiol patterns surrounded by a methyl-terminated (dodecanethiol) background with the resolution up to ~50 nm. A surface initiator (BIBB) was then attached to the patterned regions for surface-initiated atom-transfer radical polymerization of PNIPAM brushes.

EBCL is not restricted to any length scale, since the use of electron-flood guns in combination with adequate stencil masks allows an efficient patterning of large areas. For high-resolution patterning, electron beam can be focused to nanometer-sized spots, and the resolution is only limited by secondary electrons that are generated during irradiation.

### 1.2.3. Scanning probe lithography

The invention of scanning probe microscopes, such as the tunneling microscope (STM) [115] and the atomic force microscope (AFM) [116], allowed observing surface structures at atomic resolutions. STM has been also applied to move atoms or molecules to

form surface patterns [117]. A set of techniques, so-called scanning probe lithography (SPL), has been developed to generate nanoscale surface patterns based on STM and AFM. SPL can be further divided into two major modes by the type of mechanical impact to surface: destructive and constructive [2]. In case of the constructive SPL mode, the probe tip is used to generate patterns by transferring molecules of interest onto a surface of a target material. The most common constructive SPL is dip-pen nanolithography, which is described in section 1.2.4. The generation of surface patterns in the destructive SPL mode is done by mechanical damaging or chemical modification of the surface by the probe tip (Fig. 1.2 C). For example, a large current can be applied between the STM tip and SAMs to induce electrochemical oxidation and then removal of SAMs to produce patterned structures. Crooks *et al.* reported the fabrication of well-defined patterns by repeated scanning of the STM tip on C<sub>35</sub>S SAMs on Au(111) after application of a large bias (+8 V) [118]. The obtained patterns were in the range from 60 nm to 5 μm. Alternatively, Liu *et al.* have generated surface patterns *via* physical removal of SAMs when the tip was in close contact with the substrate by applying large mechanical force [119, 120]. The latter approach is usually called “nanografting” or “nanoshaving”, because the displacement of SAMs results in formation of nanopatterns.

The combination of high spatial resolution, alignment accuracy, throughput, and reproducibility makes scanning-probe lithography a promising technology to produce a wide range of patterns at the nanoscale [121]. Destructive SPL is a very flexible and high resolution technique that can be easily adapted to different study conditions, including ambient air, liquids, gases, humidity, and temperature differences, making it suitable for patterning delicate materials such as biomolecules [122]. Resolution of the destructive SPL depends on the tip shape, cantilever strength, scan domain, and the number of measurements per scan and, under the appropriate conditions, enables the manipulation of surfaces at the single-atom level [123]. However, the SLP technique is serial process in that it is time-consuming, which makes it hardly applicable in industrial field.

### 1.2.4 Dip-pen nanolithography

Dip-pen nanolithography (DPN) is based on the idea of transforming a common AFM into a virtue of a new technology. When an AFM experiment is conducted in air, capillary forces condense water vapor from the air in the small gap between the AFM tip and the surface sample. Mirkin *et al.* [124] showed that when the water flows from the tip to the sample surface, multiple nanometer patterns can be formed (Fig. 1.2 D). This

phenomenon, similar to EBL, allows for direct writing on the surface of the samples. DPN, therefore, relies on the spontaneous formation of a meniscus, which acts either as a conduit for ink transport onto a surface or as a reaction vessel. In the latter case, material precursors on the tip can be directly synthesized on the target substrate when in contact with the meniscus during the transfer process [125]. The transferred molecules act as ink, patterning molecules on the surface either *via* chemisorption or physisorption. The inked AFM probe is scanned in a serial process across the surface either in contact or tapping mode [126, 127]. When the velocity of the tip across the surface is increased, the transport of molecules is interrupted and the AFM probe acts as an imaging tool, which provides feedback on the pattern characteristics. The printing quality is influenced by probe tip geometry, writing speed, contact time between the tip and substrate, and the properties of the ink and substrate [128]. Furthermore, controlling environmental factors such as temperature and humidity is important and environmental control chambers and glove boxes are often employed to maintain control of these parameters. DPN is advantageous over traditional direct writing techniques such as  $\mu$ CP in that it allows direct writing of different molecules within a nanostructure, thereby, generating complex surface patterns architectures. In addition, a broad range of inks, from small organic molecules to biomolecules can be printed using this technique [8, 129, 130].

In summary, DPN is a serial technique that allows both hard and soft material to be patterned with minimal material losses, and there is no need for exposing the substrate to harsh conditions such as radiation or solvents. In contrast to the destructive SPL approach, DPN directly delivers the material to be patterned on the surface of a target material without the help of a resist, a stamp, substrate irradiation, or solvents, thereby avoiding surface damage or cross-contamination. As the movement of the tip is computer-controlled, the pattern can be easily changed at any point. As is true for all scanning probe techniques, DPN has the drawback of being a serial process, which implies low throughput and, therefore, increased cost [129]. This shortcoming has been partially overcome by parallel DPN [130, 131]. However, the technique still remains slow through-put speed to be implemented for industrial needs.

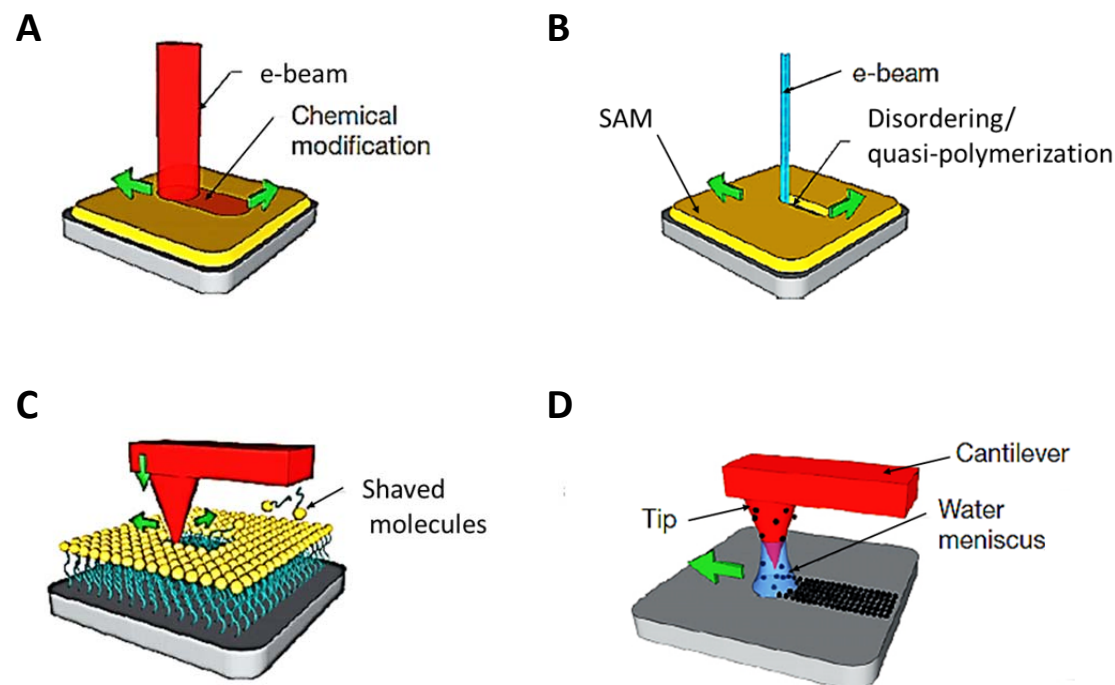


**Fig. 1.2.** Nanoscale surface patterning techniques. (A) Electron beam nanolithography: beam of electrons locally polymerizes or removes a resist-coated surface, resulting in the nanoscale pattern. (B) Electron beam chemical lithography: beam of electrons results in fragmentation and disordering of aliphatic SAMs or induces quasi-polymerization and reduction of nitro-to-amino groups in aromatic NBT SAMs. (C) Scanning probe lithography: spatially controlled shaving of molecules from the substrate with the AFM tip results in the surface pattern. (D) Dip-pen lithography: the nanopattern is created by an AFM tip previously dipped in the solution of interest. The meniscus formed by condensation of environmental water between the material surface and the AFM tip allows the transport of the molecules from the tip to the surface. [7]

**Table 1.2.** Comparison of the commonly used nanoscale surface patterning techniques.

Technique	Description	Advantages	Limitations	Applications
Electron beam lithography	Direct writing of structures with a focused electron beam on a photoresist.	High resolution. Compatible with standard microfabrication techniques.	Relatively expensive. Secondary electron scattering processes influence pattern resolution. Slow patterning speed.	SAMs [106, 132, 133] Polymers [134, 135] Hydrogels [136] Nanoparticles [133] DNA [137] Proteins [132, 134, 138-140] Cells [141, 142]
Electron beam chemical lithography	Direct writing of structures with a focused electron beam via triggering a chemical transformation of the surface.	High resolution. Low energy electron beam. Control over surface modification. Compatible with standard microfabrication techniques.	Relatively expensive. Slow patterning speed. Stability of SAMs.	Small organic molecules [107-109, 143] Polymer brushes [110, 112-114, 144, 145] Lipids [146] Cells [144]
Scanning probe lithography	Physical or chemical modification of a surface by STM or AFM tip.	High resolution. Can be used in ambient conditions.	Surface scratching. Cross-contamination of patterns.	SAMs [118, 119] Graphenes Langmuir-Bloodgett films [147] DNA [148, 149] Proteins [120, 148, 150] Lipids [151]
Dip pen nanolithography	Direct writing by an inked AFM tip on a substrate.	High resolution. Compatible with standard microfabrication techniques. Compatible with broad range of inks. Can be used for high-throughput applications (parallel DPN).	Relatively expensive. Low throughput. Printing quality dependent on myriad of environmental and system parameters.	Small organic molecules [124, 152, 153] DNA [154] Lipids [155] Proteins [126, 156, 157] Cells [153, 155]

## 1.3 Aim and objectives of this work

The overarching goal of this work was to develop a new bench-top method based on porous polymers for the generation of microliter-patterns of aqueous solutions or suspensions, to implement this method for patterning of different materials as well as for co-culturing multiple cell types, and studying cell-to-cell communication. This goal was achieved by manufacturing hydrophilic/hydrophobic micropatterned polymer surfaces followed by applying these patterns for the formation of liquid droplets with complex geometries controlled by the geometry of the hydrophilic pattern. The following secondary goals were also achieved:

[i] Optimization of the fabrication and characterization of hydrophilic/hydrophobic-patterned surfaces.

[ii] Demonstration of capabilities of the method to pattern and co-culture multiple mammalian cell populations in conjoint culture medium.

[iii] Implementation of the method in a study of the Wnt propagation phenomenon involved in the paracrine signaling.

[iv] Further improvement of the method to a maskless approach (digital liquid patterning), which does not require manufacturing of new masks or changing substrates in order to generate open liquid channels of arbitrary geometry.

These goals were accomplished by first testing different compositions of the polymerization mixture for the fabrication of highly hydrophilic porous poly(2-hydroxyethyl methacrylate-co-ethylene dimethacrylate) (HEMA-EDMA) layers. The morphology of obtained HEMA-EDMA layers was characterized by scanning electron microscopy (SEM) and dynamic light scattering (DLS) measurements. The transparency and wetting properties of samples were characterized by UV-NIR and water contact angle (WCA) measurements. Secondly, to generate hydrophobic patterns on the hydrophilic substrate, HEMA-EDMA polymer layers were photografted with 2,2,3,3,3-pentafluoropropyl methacrylate (PFMA) using a quartz photomask. To ensure the

stability of liquid droplets immobilized onto a micropatterned surface, the photografting procedure was optimized to reach the high contrast between hydrophilic and hydrophobic domains. The cross-section and surface morphology, and chemical composition of micropatterned surfaces were characterized by SEM, time-of-flight secondary ion mass spectrometry (ToF-SIMS) and WCA measurements. Different sizes of hydrophobic PFPMA domains were tested in order to find the limit of its dimensional magnitude, which can prevent fusion of closely situated droplets into the adjacent hydrophobic compartments (Chapter 3). The method was applied for the patterning of multiple cell types within separated microdroplets followed by co-culturing of cells in conjoint cell culture medium. The cross-contamination rate between the neighboring cell patterns during 3 day of co-culture was tested. The developed procedure for cell patterning was implemented for the mimicking of intercellular communication by a signaling protein (Wnt-morphogen) propagation from one patterned cell population to another (Chapter 4). In order to improve the method for generation of liquid micropatterns into a maskless liquid patterning approach, an array of hydrophilic HEMA-EDMA spots divided by hydrophobic PFPMA borders was fabricated. This approach, termed *digital liquid patterning*, is based on generation of droplets inside individual hydrophilic spots followed by manual fusion of adjacent droplets over hydrophobic border into an open liquid channel with arbitrary geometry. The influence of wetting properties of hydrophilic and hydrophobic domains, width of hydrophobic borders, and volume of droplets on the fusion of droplets was examined. Finally, the *digital liquid patterning* approach was used to show its applicability to generate liquid patterns of other biomaterials and living cells, as well as to create multi-component gradients of complex geometry (Chapter 5).

# Chapter 2

## Materials and Methods

### 2.1 Materials

2-Hydroxyethyl methacrylate, ethylene dimethacrylate, 2,2,3,3,3-pentafluoropropyl methacrylate (PFPPMA), trichloro(1H, 1H, 2H, 2H-perfluorooctyl)silane, 2,2-dimethoxy-2-phenylacetophenon, benzophenon, cyclohexanol, 1-decanol, fluorescein isothiocyanate isomer I, rhodamine B, low gelling temperature agarose, 40-75  $\mu\text{m}$  silica gel were purchased from Sigma-Aldrich (Germany) at purity >97%. Food colorants were purchased from August Thomsen Corp. (USA). 1-Butanol was purchased from Carl Roth (Germany) at purity of 99,5%. All other chemicals were purchased from Sigma-Aldrich and used as supplied.

Quartz photomask was developed with Autodesk Inventor 2011 software and manufactured by Rose Fotomasken (Germany). Borosilicate glass plates Nexterion B from Schott (Germany). Teflon films employed in this study were from American Durafilm (USA).

Dulbacco's modified Eagle's medium (DMEM), fetal bovine serum (FBS), phosphate buffered saline (PBS), penicillin / streptomycin mixture, trypsin were purchased from Invitrogen (USA).

### 2.2 Fabrication of hydrophobic/hydrophilic patterned surfaces

In the first step, glass slides were activated by sodium hydroxide followed by the modification with 3-(trimethoxysilyl)propyl methacrylate to introduce anchoring groups for a subsequent immobilization of the polymer film. To this end, glass slides were cleaned by MilliQ water and dried in air. Afterwards, the cleaned glass sides were immersed in a 1 M NaOH solution for 30 min, washed with water, and immersed in 0,2 M HCl for 1 h, followed by washing with water and drying with an air gun (Fig. 2.2 (i-ii)). In order to

achieve covalent attachment of the polymer layer to the glass support, the surface was functionalized with anchoring groups. For this purpose, the surface of an activated glass slide was modified with a 20% (v/v) solution of 3-(trimethoxysilyl)propyl methacrylate (Fig. 2.1 A) in ethanol adjusted to pH=5 with acetic acid (Fig. 2.2 (iv)). 100  $\mu$ l of the solution is dropped on the glass slide. The glass slide was then covered with another activated glass slide, avoiding the trapping of air bubbles in between. After 30 min, the new portion of solution was applied for another 0,5 h. Finally, the silylated glass slides were washed with ethanol followed by MilliQ water and dried under air flow.

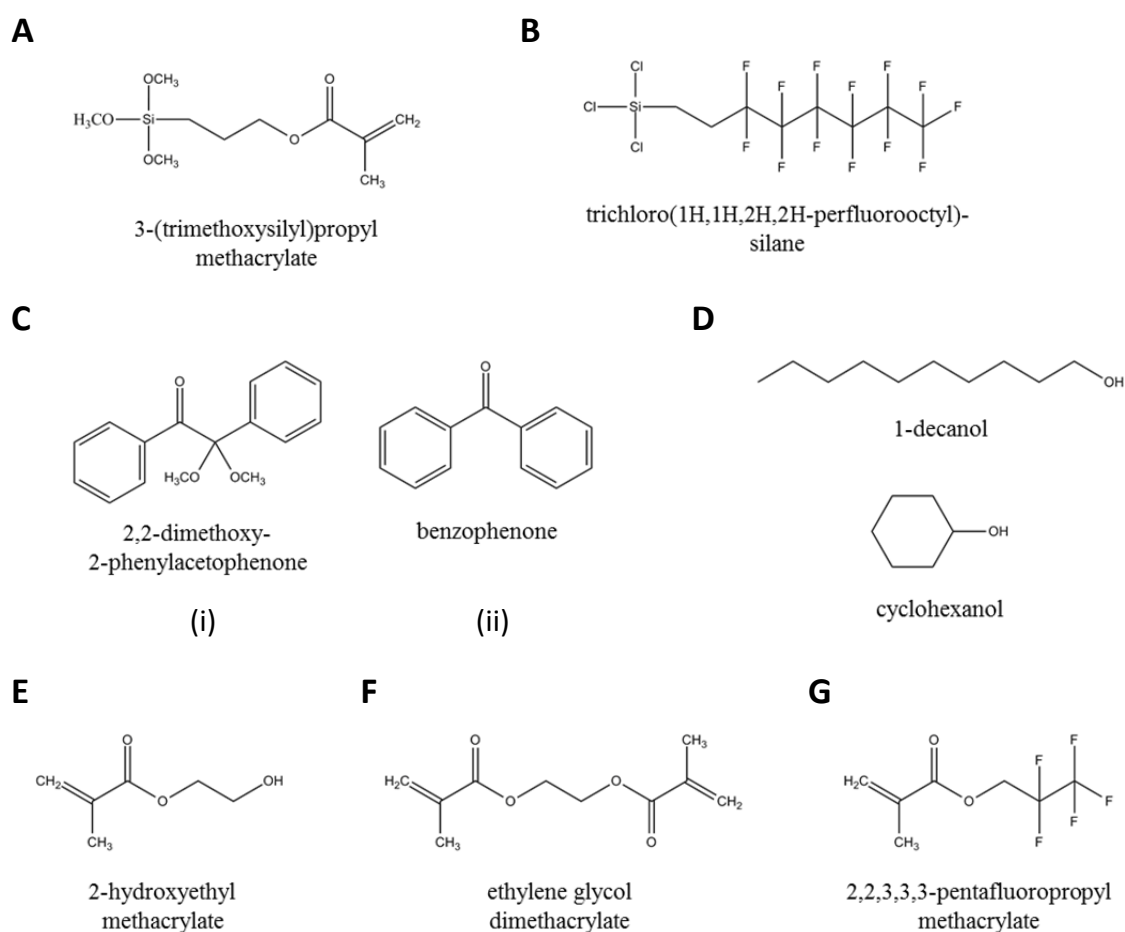


**Fig. 2.1.** Chemical structures of reactants. (A) Anchoring agent. (B) Fluorination agent. (C) Initiators for the polymerization (i) and the photografting process (ii). (D) Porogenic solvents. (E) Monomer of polymerization mixture film. (F) Cross-linker. (G) Monomer used for the photografting.

Fluorinated glass slides were used as cover slides to prevent an attachment of the polymer during the polymerization. The fluorination of glass slides were fabricated by placing an open vial of trichloro(1H, 1H, 2H, 2H-perfluorooctyl)silane (Fig. 2.1 B)

together with an activated glass slide into a vacuumated desiccator overnight (Fig. 2.2 (iii)). Afterwards, the glass slides were washed with ethanol, dried with an air gun and stored at room temperature.

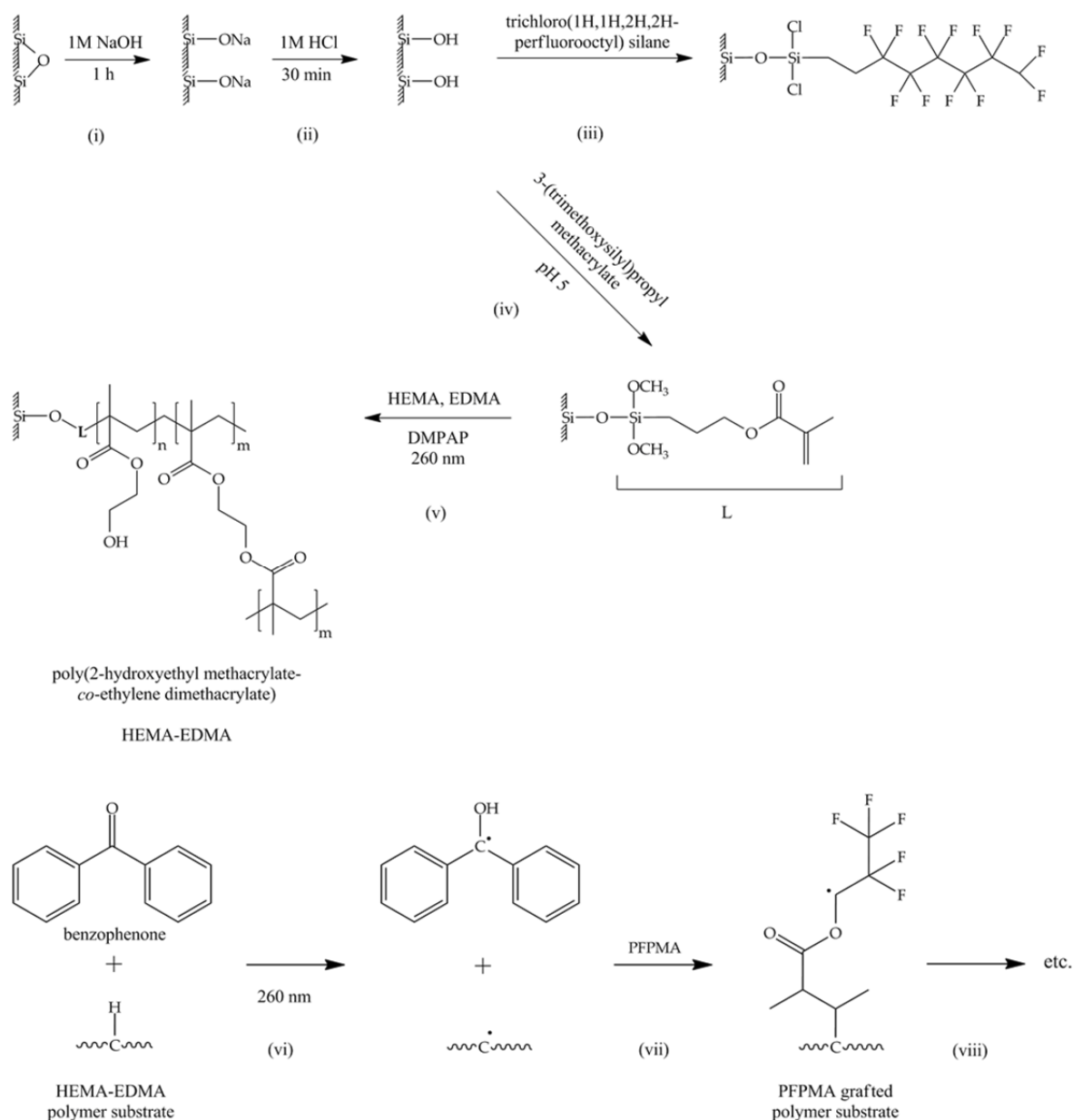


**Fig. 2.2.** Scheme of reactions for the fabrication of patterned surfaces: (i,ii) activation of a glass surface by immersing in alkaline solution, followed by acid solution; (iii) functionalization of an activated glass surface by trichloro(1H,1H,2H,2H-perfluorooctyl)silane; (iv) introduction of anchoring groups by modification of an activated glass surface with 3-(trimethoxysilyl)propyl methacrylate; (v) fabrication of a hydrophilic HEMA-EDMA layer on the modified glass support by free-radical co-polymerization of 2-hydroxyethyl methacrylate monomer and ethylene dimethacrylate cross-linker catalyzed by

2,2-dimethoxy-2-phenylacetophenone; (vi-viii) photografting functionalization of HEMA-EDMA substrate via photografting through a quartz photomask with 2,2,3,3,3-pentafluoropropyl methacrylate catalyzed by benzophenone.

In the second step, a thin hydrophilic polymer layer was fabricated on the silylated glass slide (Fig. 2.2 (v)) by UV-initiated free radical polymerization [158-160]. The poly(2-hydroxyethyl methacrylate-*co*-ethylene dimethacrylate) (HEMA-EDMA) layer was produced by the polymerization of a mixture of 24% wt. 2-hydroxyethyl methacrylate as a monomer (Fig. 2.1 E), 16% wt. ethylene dimethacrylate as a cross-linker (Fig. 2.1 F), 12% wt. 1-decanol and 48% wt. cyclohexanol as porogenic solvents (Fig. 2.1 D), and 1% wt. (with respect to monomers) 2,2-dimethoxy-2-phenylacetophenone as an initiator (Fig. 2.1 C(i)). The polymerization mixture was loaded into a slot between the activated and fluorinated glass slides. The glass slides were set apart by 12,5  $\mu\text{m}$  Teflon film spacers and fixed with binder clips (Fig. 2.3). The reaction was accomplished by exposure to UV-light ( $\lambda = 260 \text{ nm}$ ,  $10 \text{ mW/cm}^2$ ) for 15 min. Afterwards, the glass slides were separated by a scalpel. The polymer layer was washed with ethanol and then immersed into methanol for 12 h. Finally, the glass slides were washed with ethanol, dried in air flow and stored at room temperature.

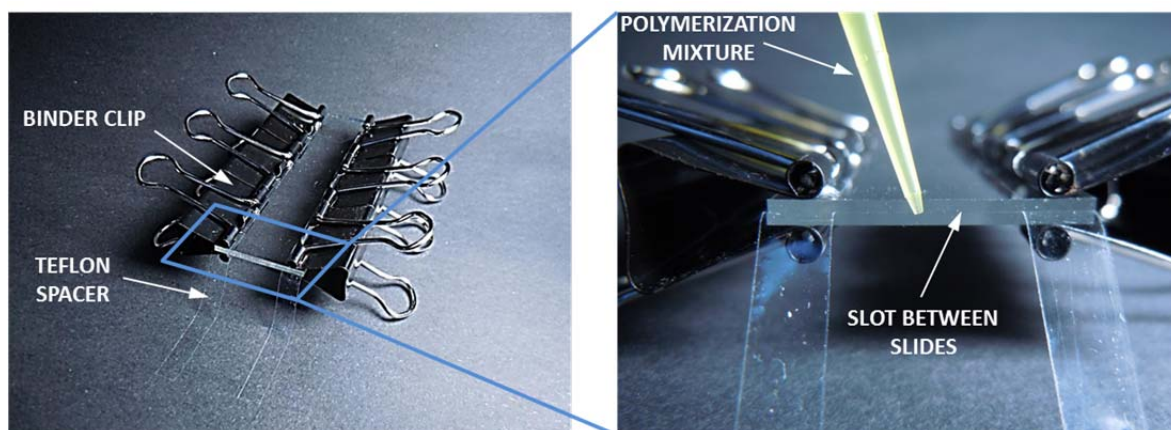


**Fig. 2.3.** Fabrication of HEMA-EDMA polymer layer. The methacrylated and fluorinated glass slides are separated by 12,5  $\mu\text{m}$  thin Teflon spacers and fixed with binder clips; polymerization mixture is injected in the slot between the glass slides.

In the final step, the hydrophobic 2,2,3,3,3-pentafluoropropyl methacrylate (PFPPMA) patterns were generated on the hydrophilic HEMA-EDMA substrate by photografting [160-168]. 100  $\mu\text{l}$  of the photografting mixture (25% wt. PFPPMA as a monomer (Fig. 2.1 G), 1,7% wt. ethylene dimethacrylate as a cross-linker, 0,4% wt.

benzophenon as a photoinitiator (Fig. 2.1 C(ii)) in 1/3 (v.) water/1-butanol mixture as solvents) was dropped and distributed on the top of HEMA-EDMA polymer layer. The wetted polymer layer was covered with a 50  $\mu\text{m}$  Teflon film, avoiding trapped air bubbles in between. Afterwards, a quartz photomask with geometry of interest was placed on the top of the Teflon film cover. The construct was irradiated with UV-light (260 nm, 8-12  $\text{mW}/\text{cm}^2$ ) for 15 min. The benzophenone molecule is excited by UV-light and abstracts a proton from a carbon atom of the polymer chain. The carbon radical hits the methacrylate group of a monomer molecule that leads to the formation a covalent bond between the polymer chain and the monomer. Thus, irradiation with UV light triggers free radical polymerization that leads to the growth of polymer brushes made of PFPMA monomers on the polymer substrate [169, 170] (Fig 2.2 (vi-viii)). The reaction can be continued to form a polymer brush. The obtained hydrophilic/hydrophobic chemical patterns were washed with ethanol and stored at room temperature.

### **2.3 Scanning electron microscopy**

The surface and cross-section morphologies of polymer films were analyzed using the ZEISS Leo 1530 (Carl Zeiss NTS GmbH, Germany; INT, KIT) scanning electron microscope after gold sputtering (15 nm) using the Balzers Union MED 10 (INT, KIT). The analysis chamber was held at  $\sim 9 \cdot 10^{-6}$  mbar during experiment. The accelerating voltage was held at 2 kV.

### **2.4 Measuring water contact angle and water dispensing/withdrawing experiments**

Water contact angles (WCA) were evaluated with UK1117 camera (EHD imaging GmbH, Germany), 5  $\mu\text{L}$  syringe (Hamilton, Switzerland) by a sessile drop measuring method. The static WCAs were determined by placing 3  $\mu\text{L}$  of MilliQ water to a substrate. The advancing and receding WCAs were determined by the consecutive addition and subtraction of MilliQ water to the droplet with maximum volume of 5  $\mu\text{L}$ . The measurements of WCAs were repeated at least four times. The calculation of WCA was performed using ImageJ Drop Analyzer plug-in. Dispensing and withdrawing water experiments (Fig. 5.2-5.4) was performed at flow speed 15  $\mu\text{L}/\text{min}$ . The images of droplets were captured at the speed 300 ms per frame.

## 2.5 Measuring time and rate of droplet evaporation

The measurements of the time and evaporation rate of water droplets from hydrophilic spots with different geometries were performed at 22-23 °C and 13-16 % relative humidity of air in a clean room. Deionized water was pipetted in a hydrophilic spot surrounded by a 100 µm hydrophobic border. The hydrophilic/hydrophobic micropatterned substrates were cleaned before the experiment with ethanol and extensively dried by using an air gun. The initial ratio of droplet volume to a surface area was the same for spots with different geometry 0,5 µl/mm<sup>2</sup>. The hydrophilic spots had circular, square, and hexagonal geometries (Table 2.1). Images of the evaporating droplet were recorded every 5 sec by a CCD-camera (UK1117, EHD imaging GmbH, Germany). The contact angle and height of the evaporating droplet were measured using the produced images with the help of ImageJ software. The droplet contact area (i.e. the area of hydrophilic spots), remained equal to the initial droplet contact area during the experiments for all geometries of the hydrophilic spots (Fig. 5.6). To obtain statistically representative data, the evaporation experiment for each spot geometry was repeated at least six times.

**Table 2.1.** Dependence of the time and rate of droplet evaporation on the geometry and area of hydrophilic spots.

Geometry of hydrophilic spot	Area of spot, mm <sup>2</sup>	Mass of droplet, mg	Time of evaporation, sec	Rate of evaporation, 10 <sup>3</sup> ·mg/sec
Circle (3 mm diameter)	7,07	3,53	875±20	4,03
Square (3 mm side length)	9,00	4,50	960±25	4,69
Hexagon (2 mm side length)	10,39	5,20	1105±20	4,71

## 2.6 Time-of-flight secondary ion mass spectrometry

Time-of-flight secondary ion mass spectrometry (ToF-SIMS) images were obtained by ToF-SIMS 5 machine (ION TOF Inc., Munster, Germany). The analysis chamber was held at  $\sim 8 \cdot 10^{-9}$  mbar during experiment. The primary ion beam was generated by using a liquid metal ion gun fitted with a pure bismuth ion. Bi<sup>1+</sup> primary ion source with a kinetic energy of 25 keV was used for all image and spectral data acquisition. All data were collected in high mass resolution bunched mode unless otherwise indicated. The data were analyzed by ION TOF software (ION TOF Inc., Munster, Germany). Spectra and images

were acquired and care was taken to use a new sample area for each analysis. All images contained 256×256 pixels. The field of view is given in figure legends.

## **2.7 Dynamic light scattering**

Dynamic light scattering (DLS) measurements were performed using a Zetasizer Nano ZS (Malvern Instruments, UK) equipped with 10 mW He-NE laser at a wavelength of 633 nm. Bulk samples of HEMA-EDMA polymers obtained from the polymerization mixtures (Table 3.1) were prepared by gently removing polymer layers from the glass support (Schott Nexterion B, Germany) using a spatula. The resulted samples were collected into individual Eppendorf tubes followed by suspending in 1 ml of ethanol. Afterwards, the tubes were sonicated in an ultrasonic bath (Elmasonic S 30 H, Germany) for 5 min at room temperature. The samples were introduced into polystyrene cuvettes and stabilized for 2 min at a room temperature. The autocorrelation functions were used to obtain the size distribution of the polymer globules (Zetasizer Software v. 6.34, Malvern Instruments, UK). All values of the globule size for each polymerization mixture were averaged over 18 individual measurements.

## **2.8 UV-NIR transmittance spectroscopy**

The transmittance of the HEMA-EDMA porous polymer layers in the UV to NIR spectral range was measured using a commercial high-resolution spectrophotometer (HR2000+, Ocean Optics, Germany). Each HEMA-EDMA film was prepared on a glass support (Schott Nexterion B, Germany) using polymerization mixtures 1-6 (Table 3.1). The polymer layers was circa 12,5  $\mu\text{m}$  in thickness. Input and output UV/Vis/NIR light beams were provided by a balanced deuterium tungsten-halogen light source (DH-2000-BAL, Ocean Optics) and transmitted through two steel-jacketed optical fibers (QP400- 2-SR-BX, Ocean Optics; 400  $\mu\text{m}$  core diameter) optimized for transmission in the spectral range 200–1100 nm. The transmitted light beam was dispersed into its various wavelengths by a monochromator and sent to a CCD detector. All spectra were recorded and processed using the SpectraSuite software (Ocean Optics). The absorption spectra were taken as the negative logarithmic ratio of background-corrected signals. As reference the clean glass slide (Schott Nexterion B, Germany) was recorded. Assuming a spherical shape of the polymer particles and Mie-scattering regime, the spectra of light transmittance were simulated by MiaPlot 4.3.05 software [171-175]. To show the relative transparency of

HEMA-EDMA polymer layers the samples were placed over a printed template and photographs were captured with Nikon Coolpix S8000 digital camera (China).

## **2.9 Generation of liquid gradients**

Open liquid channels of different geometry were generated on an array of hydrophilic HEMA-EDMA spots, each 3×3 mm. The spots were surrounded by hydrophobic PFPMA borders. To generate gradient inside the channel a drop of 1 mg/ml a food colorant or 1 mM fluorescein solution was secreted and suspended from a pipette tip approximately 1 mm above the liquid pattern at one end of the channel. With one gentle motion the drop was dislodged into the open channel from the tip. After the drop coalesced with the fluid, the chemical starts quickly extending aside and along the middle line of the channel (Fig. 5.6). The spreading of the chemical initially forms a stripe with a sharp parabolic-shape end. The chemical distribution within the stripe becomes homogeneous after a few minutes due to diffusion. Finally, the chemicals formed linear gradients along the middle line of the channel independently of the geometry of liquid channels. The resulting gradients were observed for 1 h after the drop coalesced with the liquid channel.

## **2.10 Cell cultures**

Green and red fluorescent rat mammary carcinoma MLIy-CMV-EGFP-neo and MLIy-CMV-mCherry-neo, human embryonic kidney HEK 293, human cervical tumor HeLa, mouse embryonic fibroblasts NIH-3T3 cell lines were kindly donated by Prof. Jonathan P. Sleeman and Dr. Olivier Kassel (Institute of Toxicology and Genetics, KIT, Germany). Human Cervical tumor cell line HeLa expressing GFP was purchased from BioCat (Heidelberg, Germany). All cell lines were cultured using DMEM, supplemented with 10% FBS, 100 u/ml penicillin and 0,1 mg/ml streptomycin. Cells were cultured at 37°C in a humidified atmosphere of CO<sub>2</sub> and 95% air. The initial cell seeding numbers were 5–10×10<sup>3</sup> cells/cm<sup>2</sup>. The cultured cells were observed with inverted light microscope (CKX 31 Olympus, Japan) and counted using a blood cell counting chamber (Neugebauer, Germany).

## **2.11 Cell patterning**

Patterning of cells on the hydrophilic/hydrophobic microstructured surfaces was performed by simple pipetting a cell suspension onto the hydrophilic domains (Fig. 4.1 (i-

iii)). To this end, an appropriate volume of cell suspension was pipetted onto each hydrophilic region surrounded by a hydrophobic border. In that, the formed liquid patterns, i.e. microliter droplets of cell suspensions were immobilized onto the patterned surface by surface-tension forces between the hydrophilic and hydrophobic domains. The initial cell seeding density was  $50 \times 10^3$  cells/cm<sup>2</sup>. Cells were cultivated inside of separated reservoirs at 37 °C and 5% of CO<sub>2</sub> for 18 h. Glass plate was then washed with PBS in order to remove non-adherent cells, and replaced in fresh cell culture medium. The adhered cells were further cultivated conjointly. The fluorescence images were obtained either with a Leica MZ10F fluorescence microscope (Germany), Leica DFC360 FX (Germany) and Keyence BZ-9000 (Japan) microscopes.

## **2.12 Cell proliferation assay**

HEK 293 cells were seeded on HEMA-EDMA substrate at concentration of  $25 \times 10^3$  cells/cm<sup>2</sup>. Cell proliferation of cells was assessed by an increase of the number of adhered cells. The number of only adhered cells was counted at 24 h, 48 h and 72 h after seeding. The experiment for each time point was repeated at least three times to obtain representative values.

## **2.13 Cross-contamination assay**

MLTy-mCherry red fluorescent cells and HeLa-EGFP green fluorescent cells were seeded at concentration  $50 \times 10^3$  cells/cm<sup>2</sup> into neighboring hydrophilic HEMA-EDMA domains of rectangular geometry, each  $3 \times 10$  mm. The hydrophilic domains were surrounded by a hydrophobic PFPMA background and separated with a thin hydrophobic gap in between. In all experiments the width of the hydrophobic gap was 100 μm. The cells in the isolated hydrophilic compartments (i.e. separated microliter-volume droplets) were cultured for 18 h to get cells adhered to the surface of their own compartment. Afterwards, the adjacent compartments of the red and green fluorescent adhered cells were connected, washed several times with PBS and immersed into the same medium in a Petri dish. Further, the patterned cells were co-cultured for 24 h, 48 h and 72 h and fixed with 4% formaldehyde. The fluorescent and bright field images of the patterned cells were taken using a fluorescent microscope (Keyence BZ-9000, Japan). The images were processed by using with BZ-II Analyzer software (Keyence, Japan). The cross-contamination rate between the adjacent cell patterns was calculated based on the fluorescent intensity by

using ImageJ software. Experiments for each time point of cultivation were repeated at least 3 times to obtain representative values.

# Chapter 3

## **Fabrication and characterization of a hydrophilic-hydrophobic micropatterned surface for generation of liquid patterns**

### **3.1 Summary**

In this chapter, a new and facile method for the generation of liquid patterns with on-demand geometry is presented. The method is based on the surface-tension confinement of aqueous solutions on a patterned surface. The patterned surface consists of highly hydrophilic and hydrophobic regions. Liquid patterns are generated by simple pipetting of the solution onto the hydrophilic domains. The patterned surfaces were prepared on a glass support by *in situ* UV-initiated free radical polymerization of poly(2-hydroxyethyl methacrylate-*co*-ethylene dimethacrylate) (HEMA-EDMA), followed by the generation of the hydrophobic domains by photoinitiated grafting with 2,2,3,3,3-pentafluoropropyl methacrylate (PFPPMA). The wettability, transparency, porous properties and chemical composition of the HEMA-EDMA substrate and PFPPMA-domains were thoroughly characterized by static and dynamic water contact angle (WCA) measurements, UV-Vis spectroscopy, scanning electron microscopy (SEM), dynamic light scattering (DLS) measurements and time-of-flight secondary ion mass spectrometry (ToF-SIMS). The transparency of the thin HEMA-EDMA polymer layer is well-suited for a microscopic observation of samples. The high difference in wettability of the highly hydrophilic and hydrophobic domains allows the strong immobilization of droplets inside the hydrophilic area and durability during user manipulations. The developed technique enables the achievement of micrometer-precise liquid patterns without special skills, sophisticated dispensing equipment or a clean room and would be suitable for a variety of studies associated with liquid patterning.

### 3.2 Introduction

The control over the spreading of fluids and precise confinement of their shape on a surface has a plethora of engineering applications such as generation of surface gradients [176, 177], microparticles and cell patterning [178], droplet-driven material transfer and microfluidics in open liquid channels [179, 180], devices for liquid-liquid extraction [181] and droplet manipulation [182, 183]. However, among the existing surface patterning techniques there are only a few that allow the fabrication of liquid patterns, i.e. the generation of droplets of liquid on the substrate with geometry on-demand.

Notably, the well-known surface-wetting theory was applied to develop a new strategy for the confinement of fluids on a surface. Lipowsky and co-authors describe theoretical aspects of wetting and dewetting of heterogeneously patterned surface [184-189]. Whitesides and co-authors as well used the theoretical frameworks and finite element methods to predict the shape of droplets on hydrophilic/hydrophobic patterned surfaces [190-193]. This wetting/dewetting approach for liquid patterning is based on the fact that the shape of a droplet resting on a surface depends on its volume, the surface tension of a liquid, the contact angle, and the shape of the contact line [194]. In turn, the shape of the contact line can be controlled by patterning a substrate with hydrophilic and hydrophobic regions. The hydrophobic regions act as virtual walls, while the hydrophilic regions play a role of virtual reservoirs for liquid. In that, the geometry of the droplet is defined by the geometry of the contour of hydrophobic regions.

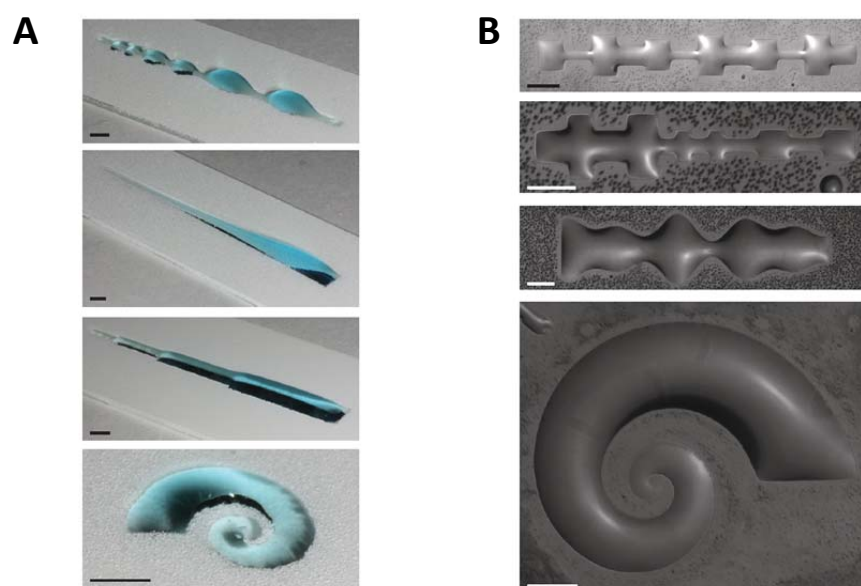


**Fig. 3.1.** Liquid patterning approach based on using hydrophilic/hydrophobic patterned surfaces. (A) Microliter volume patterns fabricated by a mask method. Scale bars 3 mm.

(B) Nanoliter volume patterns fabricated by microcontact printing. Scale bars 300  $\mu\text{m}$ . [178]

Liquid patterning based on the surface-tension confinement between hydrophilic and hydrophobic domains has been extensively elaborated by Hancock et al. [176-178]. The fabrication of the hydrophilic/hydrophobic structured surface was performed by masking or microcontact printing for macro- and microscale surface patterns, respectively. In the case of the mask method, first, a vinyl stencil or cutout was precision-cut with a cutting plotter. Afterwards, they were coated with a hydrophobic spray (WX2100, Cytonix Corp., USA) and finally applied to a hydrophilic glass support. For microscale patterning, a PDMS-stamp was fabricated by soft lithography and spin-coated with octadecyltrichlorosilane (OTS) solution. The PDMS-stamp was pressed onto a glass slide, leaving the hydrophobic OTS fingerprint on it. The generation of liquid patterns at the macroscale was performed by simple pipetting of liquid onto the hydrophilic regions, resulting in the spreading of liquid inside the hydrophilic domains until the hydrophobic borders (Fig. 3.1 A). However, the features of hydrophilic/hydrophobic patterned surfaces fabricated by the microcontact printing technique were too small for direct pipetting or dispensing liquid. Thereby, nanoliter-volume liquid patterns at the microscale were generated in the humidified chamber by rolling microliter-volume droplets over the patterned area (Fig. 3.1 B). Hancock and co-authors used a hydrophilic channel surrounded by a hydrophobic boundary to produce centimeter-scale long gradients of biomolecules, microparticles and cells by means of passive capillary flow. The integration of microwell arrays into the open liquid channel enables high-throughput screening studies [177]. They further utilized the approach to generate linear gradients of bio-hydrogels for the investigation of cell motility [176]. In addition, by using finite element simulations to predict the 3D shape of nano- and microliter droplets, the geometry of hydrophilic/hydrophobic surface patterns could be predefined in order to control the surface concentration of cells or microparticles [178].

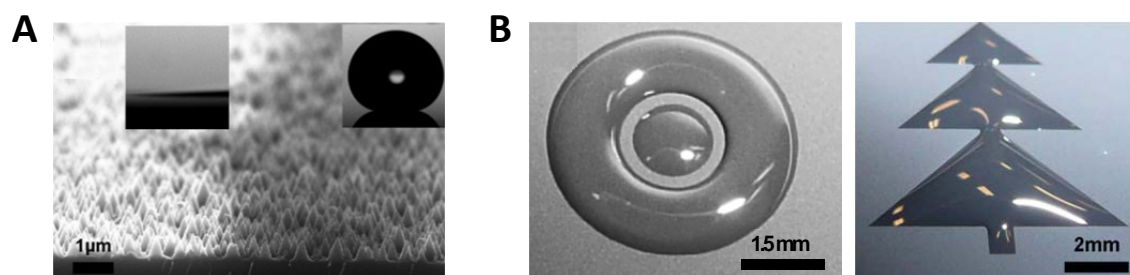


**Fig. 3.2.** Liquid patterning approach based on using superhydrophilic/superhydrophobic patterned surfaces. (A) SEM micrograph of non-coated (bright, left side) and fluoropolymer (dark, right side) coated silicon nano-grass with corresponding photographs of sessile water droplets. (B) Examples of liquid patterns. [182]

The stability of liquid patterns significantly depends on the difference in wettability of the hydrophobic and hydrophilic domains. Jokinen et al. used superhydrophilic/superhydrophobic patterned surface for the generation of droplets with a geometry of interest [182]. The superhydrophilic substrate was manufactured from silicon wafer by deep reactive ion etching, resulting in a highly rough silicon surface (also known as black silicone or nanograss). The superhydrophobic domains were fabricated by fluoropolymer coating using photolithography (Fig. 3.2 A). Droplets of various geometries were generated on the microstructured surface by pipetting water or oil inside the superhydrophilic regions (Fig. 3.2 B). Jokinen and co-authors used superhydrophilic/superhydrophobic patterned surfaces to advance the control over passive droplet transfer and droplet splitting suitable for microfluidic applications [182, 183]. By using a special design of surface patterns to create the oil-water droplets, they performed multiphase liquid-liquid (aqueous-organic-aqueous) extraction for immiscible liquids [181]. This approach can be further developed for the investigation of liquid partition or mimicking of drug-permeation processes.

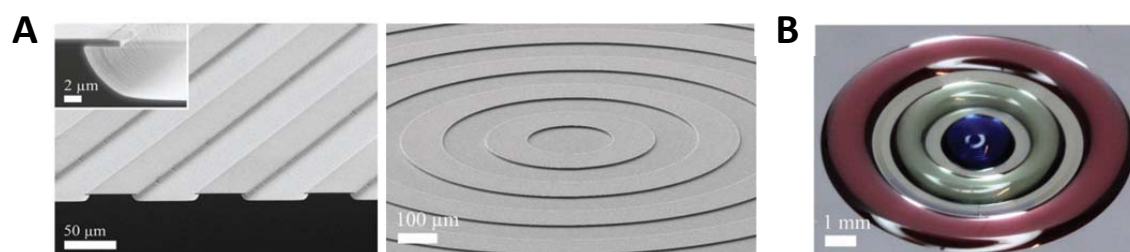


**Fig. 3.3.** Liquid patterning approach based on micropatterned structures with undercut edges. (A) SEM micrographs of circular micropatterns with undercut edges. (B) Liquid pattern.

droplets with the shape of concentric circles (water dyed blue, ethylene glycol dyed yellow, hexadecane dyed red). [195]

An interesting approach for liquid patterning has been developed by Liimatainen et al. [195]. The method is based on the pinning of a liquid by undercut edges. This effect is described by Gibbs inequality:

$$\theta_0 \leq \theta_{app} \leq (180^\circ - \psi) + \theta_0 \quad (1)$$

where  $\theta_0$  is the static contact angle of a smooth surface,  $\theta_{app}$  is the apparent contact angle, and  $\psi$  – the angle of an undercut edge. Thereby, a spreading liquid meeting an undercut sharp edge ( $\psi \approx 0$ ) may have ultra-high values of apparent contact angle, which significantly exceed the contact angle of the smooth surface. The surface micropatterns with undercut edges were fabricated on silicon or silicon oxide wafers by standard photolithography followed by dry etching for the undercut structure (Fig. 3.3 A). By using the effect of undercut topography to obtain ultrahydrophobicity ( $\theta_{app}=180^\circ$ ), liquid patterns could be generated by simple pipetting of fluid onto the etched areas, resulting in the fast spreading of the liquid along the undercut contours (Fig. 3.3 B).

### 3.3 Fabrication of hydrophilic/hydrophobic patterned surfaces

The fabrication of hydrophilic/hydrophobic patterned surfaces includes two main steps. First, a glass slide is coated with hydrophilic porous poly(2-hydroxyethyl methacrylate-*co*-ethylene dimethacrylate) (HEMA-EDMA) film. Then, hydrophobic patterns are fabricated on the hydrophilic polymer film by photoinitiated grafting with 2,2,3,3,3-pentafluoropropyl methacrylate (PFPPMA) (Fig. 2.1, 2.2).

A ca. 12,5  $\mu\text{m}$ -thin highly hydrophilic nanoporous HEMA-EDMA film is synthesized on a glass substrate by the free-radical UV-initiated polymerization of a mixture of monomer 2-hydroxyethyl methacrylate (24 wt. %) and cross-linker ethylene dimethacrylate (16 wt. %) in the presence of 1-decanol (12 wt. %) and cyclohexanol (48 wt. %) serving as porogenic solvents, and initiator 2,2-dimethoxy-2-phenylacetophenone [158, 160]. The polymerization mixture is dispensed into a slit between silylated and fluorinated glass slides and placed under UV light for 15 min (Fig. 3.4 (i)). Afterwards, the glass slides are separated by a scalpel. During the UV-irradiation the HEMA-EDMA

polymer becomes covalently bound to the silylated glass slide, whereas the fluorinated glass slide remains intact [158, 196]. The obtained polymer film is extensively washed with and immersed in ethanol for 24 h, followed by drying with an air gun, and storing at room temperature.

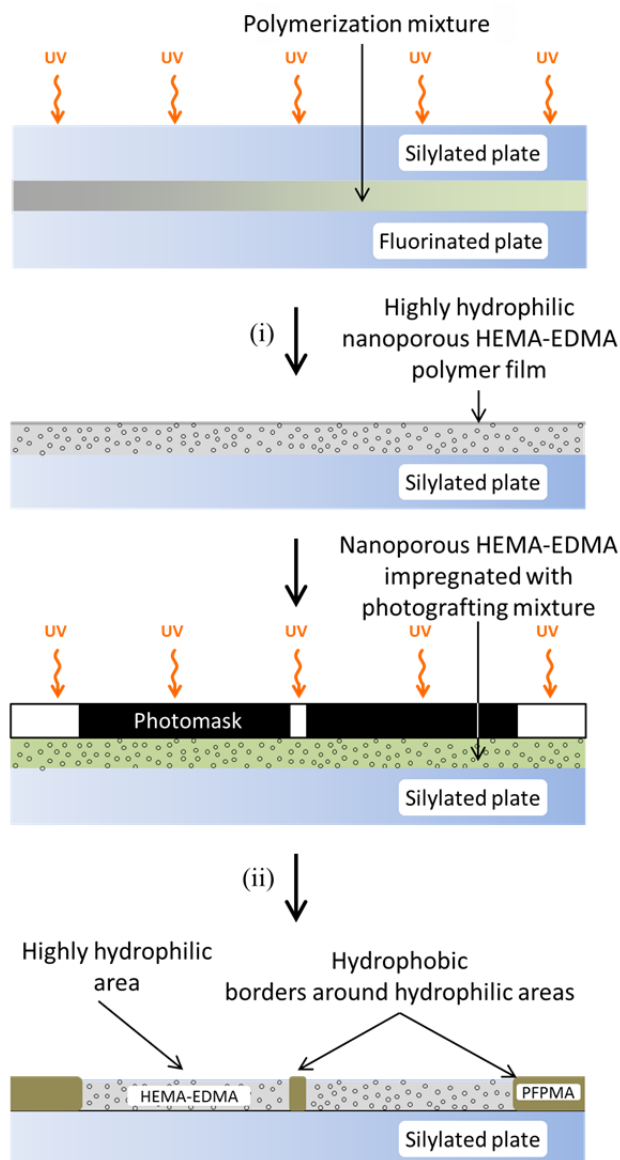


**Fig. 3.4.** Schematic description of the pattern fabrication procedure: (i) preparation of a hydrophilic nanoporous polymer film on a glass substrate by photoinitiated polymerization of 2-hydroxyethyl methacrylate and ethylene dimethacrylate in the presence of porogens; (ii) formation of hydrophobic barriers and hydrophobic background areas by photoinitiated surface grafting with poly(2,2,3,3,3-pentafluoropropyl methacrylate) brushes through a quartz photomask.

The second step in the preparation of hydrophilic/hydrophobic patterned surfaces is the fabrication of hydrophobic barriers on the hydrophilic HEMA-EDMA substrate. To this end, the surface of HEMA-EDMA is modified with polymer brushes of hydrophobic 2,2,3,3,3-pentafluoropropyl methacrylate (PFPPMA) by photoinitiated grafting [160, 162-168]. The porous polymer film is impregnated with a photografting mixture composed of 2,2,3,3,3-pentafluoropropyl methacrylate (25 % wt.) as a photografting agent, cross-linker EDMA (1,7% wt.) and initiator benzophenone (0,4% wt.) in water/*tert*-butanol (1/3 v.) mixture. The impregnated polymer film is then covered with 50  $\mu\text{m}$ -thin Teflon foil. After that, a quartz photomask with the desired pattern geometry is placed over the Teflon foil (Fig. 3.4 B (ii)). The whole construct is irradiated with UV-light for 15 min. The area exposed to UV-light becomes hydrophobic, while the area protected by non-transparent regions of the photomask remains hydrophilic. The obtained hydrophilic/hydrophobic patterned surface is washed with ethanol and stored at room temperature.

### 3.4 Generation of liquid patterns

Liquid patterns on the hydrophilic/hydrophobic microstructured surfaces are generated by pipetting an aqueous solution onto the hydrophilic regions (Fig. 3.5 A). Once injected onto the hydrophilic areas, the aqueous solution spreads until the water repellent barrier. The geometry of the liquid pattern is defined by the contour of the hydrophobic border. The high difference in wettability between HEMA-EDMA and PFPPMA areas ensures the confinement of the liquid within the hydrophilic region [178, 182].

In order to assess the wettability of the hydrophobic and hydrophilic areas we measured the water contact angles (WCA) of both substrates. The results showed that HEMA-EDMA polymer film is highly hydrophilic with static, advancing and receding WCAs being  $\theta_{st}=17,4\pm0,5^\circ$ ,  $\theta_{adv}=24,1\pm0,2^\circ$  and  $\theta_{rec}=3,8\pm0,1^\circ$ , respectively. The UV-initiated grafting of the HEMA-EDMA substrate with PFPPMA polymer brushes [197] switches the wetting properties to hydrophobic. Therefore, the PFPPMA-modified area possessed the following WCA values:  $\theta_{st}=81,2\pm0,9^\circ$ ,  $\theta_{adv}=96,4\pm1,1^\circ$  and  $\theta_{rec}=10,6\pm0,4^\circ$  (Fig. 3.5 B).

The design of the photomask defines the geometry of the hydrophobic microstructures fabricated onto the hydrophilic substrate. Variety of PFPPMA micropatterns can be generated by the UV-initiated grafting (Fig. 3.5 C). In addition, liquid patterns can be formed in close proximity to each other.

In order to find the minimal hydrophobic gap that ensures separation of dispensed microdroplets, different widths of hydrophobic barriers between hydrophilic areas were tested. In this experiment, hydrophilic/hydrophobic micropatterns were prepared where each hydrophilic area had the rectangular geometry ( $2 \times 10$  mm). The width of hydrophobic gaps between hydrophilic rectangles was  $25 \mu\text{m}$ ,  $50 \mu\text{m}$  or  $100 \mu\text{m}$ . Then,  $10 \mu\text{l}$  of milliQ water ( $50 \mu\text{l}/\text{cm}^2$ ) was injected onto each hydrophilic region in order to test the ability of the hydrophobic gaps to separate liquid into adjacent hydrophilic compartments. All hydrophobic gaps prevented the connection of water droplets (Fig. 3.6 A).

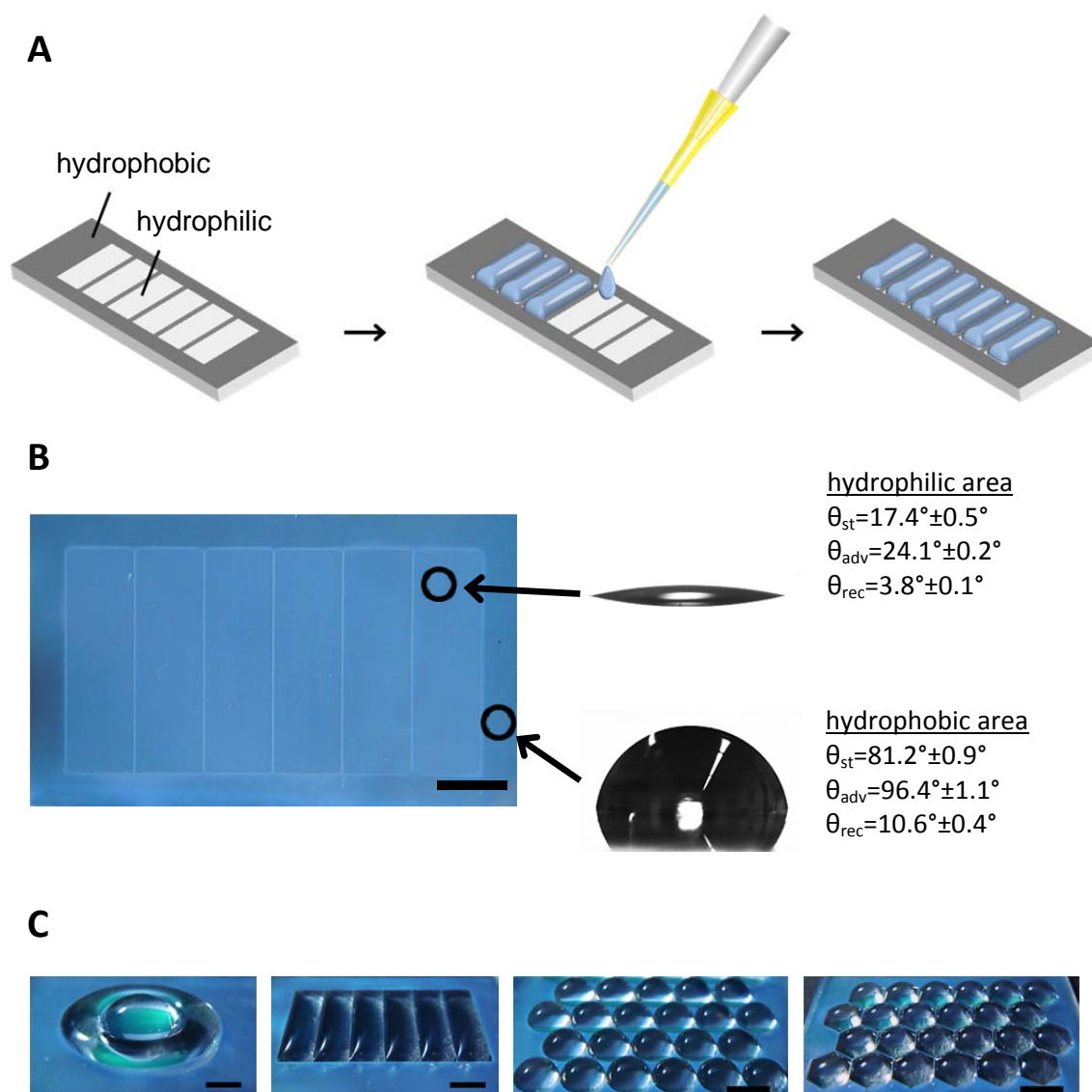


**Fig. 3.5.** (A) Schematic description of the generation of liquid patterns: the pipetting of an aqueous solution into hydrophilic regions surrounded by hydrophobic borders generates a liquid reservoir (i.e. liquid pattern) confined by the contour of the hydrophobic border. (B) Photographs of the microstructured surface and milliQ water microdroplets on the hydrophilic and hydrophobic areas with corresponding values of WCAs. The width of

hydrophobic border is 100  $\mu\text{m}$ . (C) Examples of liquid patterns with different geometry. The width of hydrophobic borders is 100  $\mu\text{m}$ . All scale bars are 3 mm.

Although the 25  $\mu\text{m}$  hydrophobic border was able to prevent the overflow of water and keep the droplets in the adjacent compartment, it was found that water could leak beneath the surface of the barrier. Fig. 3.6 B shows micropatterns filled with water 20 s after addition of water. In the case of 25  $\mu\text{m}$  border, the water spreading occurred only underneath the surface of the barrier, whereas the droplet by itself was still immobilized in the hydrophilic area. However, the leaking did not happen in the case of 50  $\mu\text{m}$  and 100  $\mu\text{m}$ .

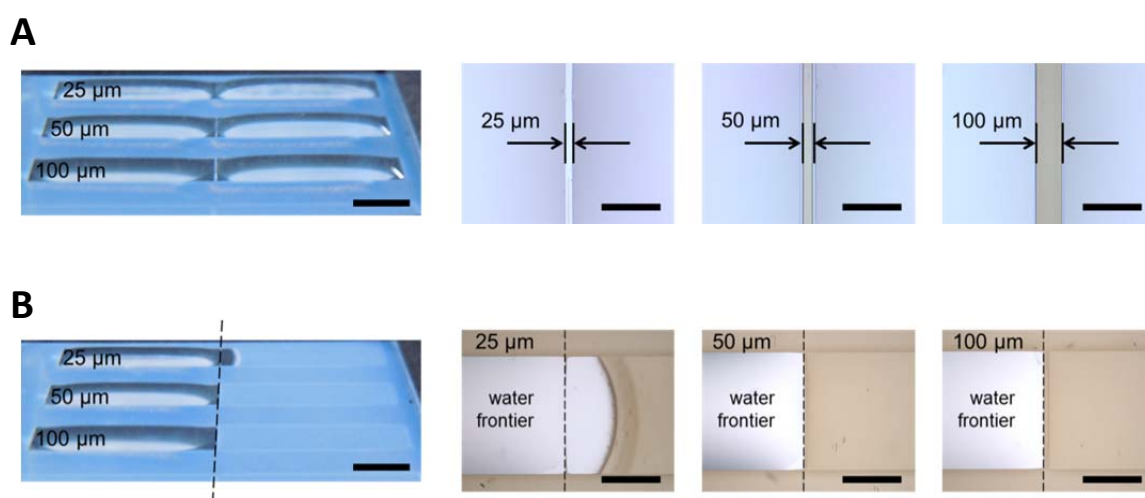


**Fig. 3.6.** (A) Set of  $2 \times 10$  mm adjacent hydrophilic patterns filled with miliQ water and corresponding microscopic images of 25  $\mu\text{m}$ , 50  $\mu\text{m}$  and 100  $\mu\text{m}$  hydrophobic borders between two separated water compartments. Scale bars are 3 mm (images of water patterns) and 200  $\mu\text{m}$  (microscopic images of the hydrophobic borders). (B) Set of  $2 \times 10$  mm adjacent hydrophilic patterns. Only one pattern in each set is filled with water. The dash line corresponds to water frontier. Microscopic images show enlarged area between two hydrophilic patterns of each set. Scale bars are 3 mm (water pattern image) and 1000  $\mu\text{m}$  (enlarged images of hydrophobic gaps).

### **3.5 Microscale morphology of hydrophilic/hydrophobic patterned surfaces**

Surface morphology was analyzed by conventional scanning electron microscopy (SEM). Fig. 3.7 shows the hydrophilic/hydrophobic microstructured surface and SEM micrographs corresponding to the highlighted regions. The shown surface possesses six parallel hydrophilic rectangles separated by thin hydrophobic borders and surrounded by hydrophobic background. Each HEMA-EDMA hydrophilic compartment is 3 mm in width and 10 mm in length. The PFPMA hydrophobic borders between the hydrophilic compartments are 100  $\mu\text{m}$  in width.

According to the top and cross-section SEM micrographs, the obtained HEMA-EDMA monolith has a highly porous structure. The thickness of the polymer substrate before photografting was  $9,7\pm 1,5 \mu\text{m}$ , while the thickness of the used Teflon spacers was  $12,5 \mu\text{m}$  (Fig. 3.7 A). The decrease in the thickness of the polymer film may be explained by the shrinkage of polymer during drying. In addition, the sizes of pores and globules were quantified using SEM images and an ImageJ plug-in. The average pore size was  $158\pm 35 \text{ nm}$ . The microglobules consist of spherical polymer nanoparticles, which are fused with each other. The average size of a single nanoparticle is  $36\pm 6 \text{ nm}$ .

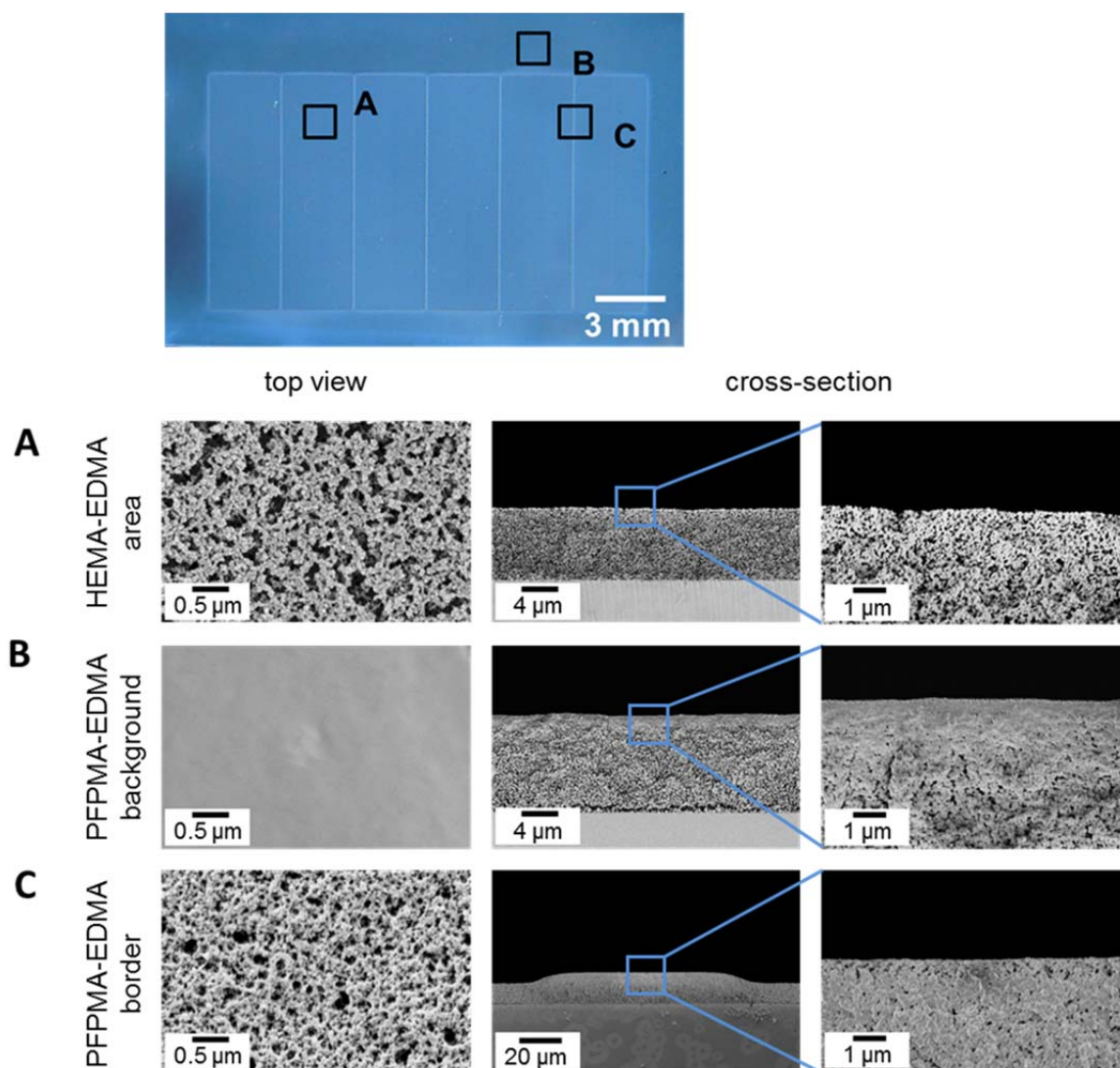


**Fig. 3.7.** Patterned surface and corresponding SEM micrographs. (A) Hydrophilic HEMA-EDMA polymer film. (B) Hydrophobic PFPPMA-grafted background. (C) 100  $\mu\text{m}$  thin hydrophobic PFPPMA-modified strip.

The PFPPMA-modified background region has a completely smooth and non-porous superficial polymer layer, while remaining highly porous and globular in structure in the bulk (Fig. 3.7 B). Noteworthy, the thickness of the polymer layer was increased in comparison with the non-grafted HEMA-EDMA substrate. By using SEM cross-sectional images obtained from four samples, the average thickness of the polymer film after photografting was quantified to be  $11,2 \pm 1,0 \mu\text{m}$ . In contrast, the superficial layer of 100  $\mu\text{m}$  thin PFPPMA-borders remained porous with structure similar to the non-grafted substrate. The SEM micrograph of the cross-section showed a highly porous structure of the grafted polymer in bulk (Fig. 3.7 C). The average size of pores and globules in the superficial layer was  $88 \pm 29 \text{ nm}$  and  $62 \pm 9 \text{ nm}$ , respectively. The thickness of the modified

polymer layer was increased by  $11,6 \pm 1,2 \mu\text{m}$  as well, forming a step-like structure. We assume that the increase in the thickness of the polymer layer (in comparison with the non-grafted monolith) may occur due to the alteration of the polymer layer stiffness caused by clumping of the pores and growth of the monolith volume after the photografting procedure.

### **3.6 Chemical composition of hydrophilic/hydrophobic patterned surfaces**

Time of flight secondary ions mass spectrometry (ToF-SIMS) was employed in order to confirm the modification of HEMA-EDMA polymer with PFPMA agent during the photografting process. Fig. 3.8 shows negative  $\text{C}_3\text{H}_2\text{F}_5\text{O}^-$ -ion ToF-SIMS images corresponding to the marked regions on the patterned surface. The patterned surface consists of six hydrophilic HEMA-EDMA regions with rectangular geometry,  $3 \times 10 \text{ mm}$  each. The rectangles are separated by  $50 \mu\text{m}$  hydrophobic PFPMA borders and surrounded by PFPMA background.

The  $\text{C}_3\text{H}_2\text{F}_5\text{O}^-$ -ion signals were detected only on the UV-light exposed area. The absence of such signals on the photomask-protected regions confirms the selectivity of the photografting process (Fig. 3.8 A,B). Noteworthy, the average  $\text{C}_3\text{H}_2\text{F}_5\text{O}^-$ -ion signal from the PFPMA-modified area is 700 fold higher as compared to the non-modified area (Fig. 3.9). The ToF-SIMS image of the cross-scan over the PFPMA-modified and HEMA-EDMA non-modified surface also confirms the selective modification of the background area, while keeping intact the area protected with the photomask. The distribution of  $\text{C}_3\text{H}_2\text{F}_5\text{O}^-$ -signal intensity has a clear step-like shape at the boundary between the hydrophobic background and hydrophilic domain (Fig. 3.8 C). According to the intensity plot, the width of the step is  $80 \mu\text{m}$ . Since ToF-SIMS is a surface chemistry sensitive method, the increase in intensity of  $\text{C}_3\text{H}_2\text{F}_5\text{O}^-$  signals corresponds to the increased density of PFPMA residues. The increased modification ratio may be explained by the excess of photografting mixture that comes from the UV protected area due to diffusion and temperature convection.

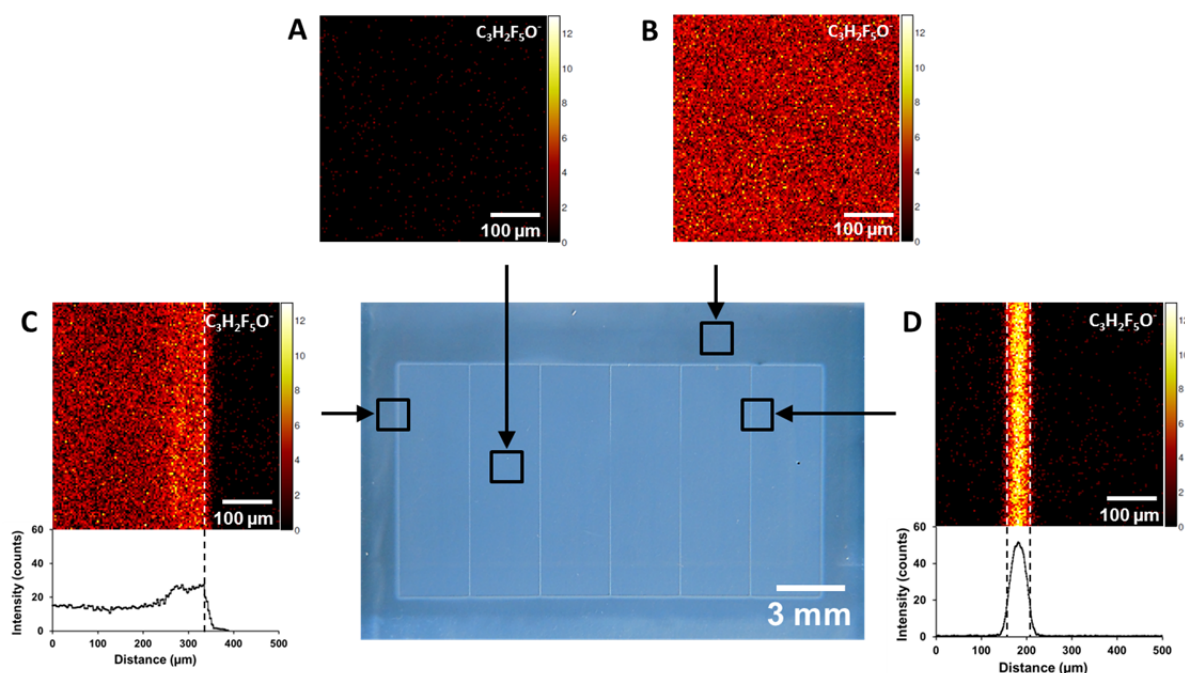


**Fig. 3.8.** Photograph of a hydrophilic/hydrophobic micropatterned surface and corresponding negative  $\text{C}_3\text{H}_2\text{F}_5\text{O}^-$ -ion ToF-SIMS images with intensity plots. (A) HEMA-EDMA polymer film. (B) PFPMA-modified hydrophobic background area. (C) Region between PFPMA-modified area and intact HEMA-EDMA polymer. (D) 50  $\mu\text{m}$  PFPMA hydrophobic border. Each ToF-SIMS image has a resolution of  $256 \times 256$  pixels.

The intensity of  $\text{C}_3\text{H}_2\text{F}_5\text{O}^-$  signals across as well as along the border is entirely homogeneous (Fig 3.8 D). The border has straight and sharp edges. The measured border width is 50  $\mu\text{m}$ , which matches the dimensions of the used photomask, demonstrating the accuracy of the photografting process.

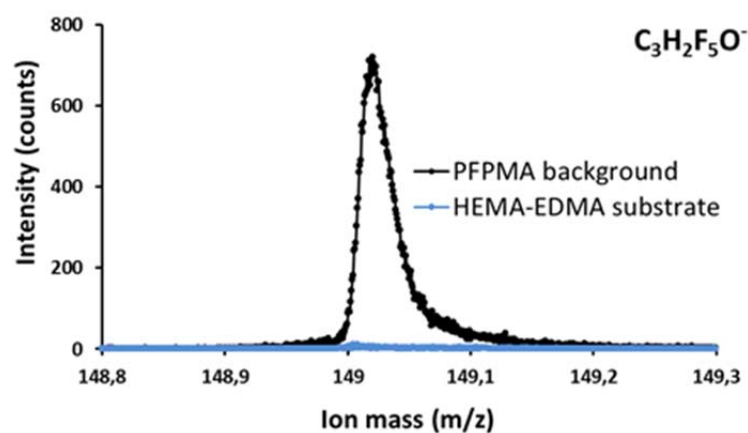


**Fig. 3.9.** Mass spectra  $\text{C}_3\text{H}_2\text{F}_5\text{O}^-$  signals of hydrophilic HEMA-EDMA (blue) and hydrophobic (black) PFPMA regions of the patterned surface.

Although ToF-SIMS surface analysis allows one to obtain information about the chemical composition of a superficial surface layer, the depth of chemical analysis does not exceed a few micrometers. To confirm that the photografting of HEMA-EDMA monolith with PFPMA occurs in bulk, we performed a ToF-SIMS measurement of a cross-section for a 100  $\mu\text{m}$ -wide PFPMA border. Since the polymer film is  $\sim 10$   $\mu\text{m}$  thick, the ToF-SIMS analysis was performed in high lateral resolution mode. This mode allows resolving objects down to  $\sim 500$  nm lateral resolution, but is accompanied by the loss of high mass resolution. Therefore, it was not possible to obtain the signal for  $\text{C}_3\text{H}_2\text{F}_5\text{O}^-$  ions, as well as for  $\text{CF}_3^-$  and  $\text{C}_2\text{F}_5^-$  ions. However, we were able to detect strong  $\text{F}^-$  signals, confirming the presence of PFPMA and its derivatives. Fig. 3.10 shows ToF-SIMS images of a HEMA-EDMA polymer film cross-section with the 100  $\mu\text{m}$ -wide PFPMA border obtained after 1 min and 15 min photografting. Each image is composed of  $\text{O}^-$ ,  $\text{C}^-$  and  $\text{F}^-$  signals. According to the obtained data, ions of fluorine were homogeneously distributed in the bulk of the impregnated film after 1 min of UV-light irradiation. There was an increase in  $\text{F}^-$  signal intensity in the region close to the glass support after 15 min of UV-irradiation. This might be associated with the binding of PFPMA molecules to unreacted methacrylate groups, which remain intact on the surface of the glass slide after the UV-irradiation of the polymerization mixture.

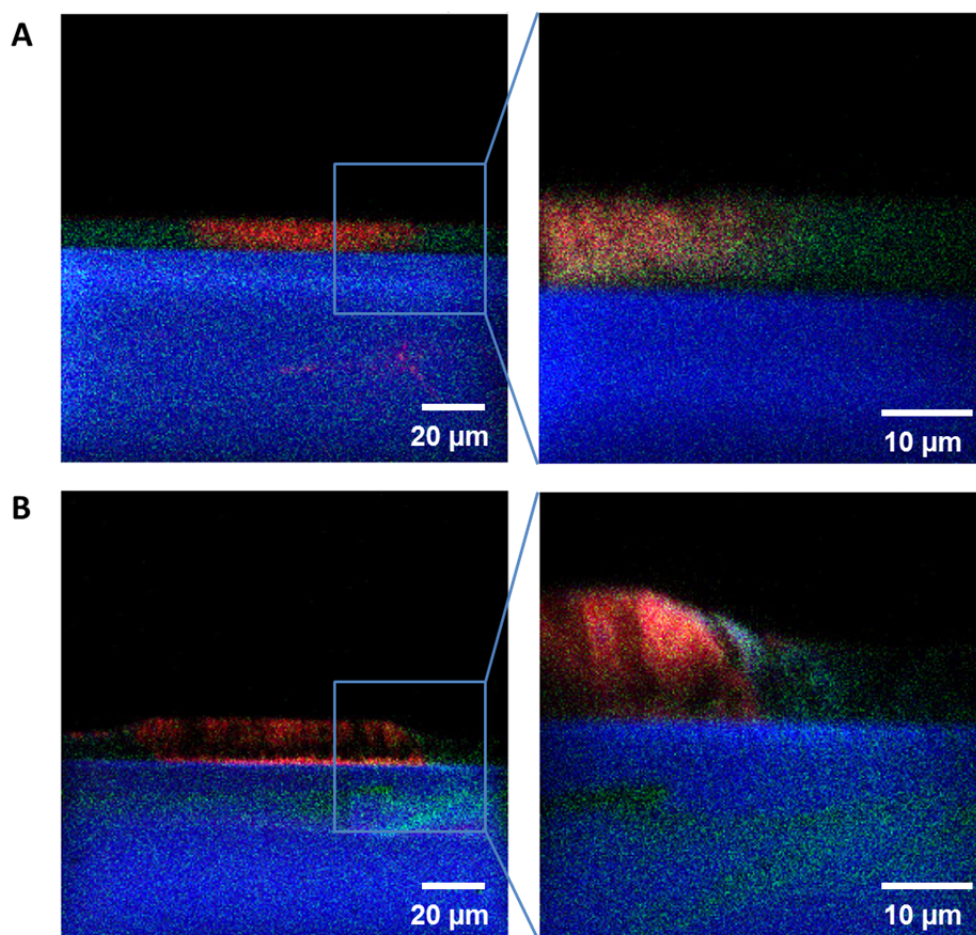


**Fig. 3.10.** ToF-SIMS cross-sectional images of a 100  $\mu\text{m}$ -wide PFPMA hydrophobic border after (A) 1 min and (B) 15 min photografting. Each ToF-SIMS image is composed of  $\text{O}^-$  (blue),  $\text{C}^-$  (green) and  $\text{F}^-$  (red) negative secondary ions' signals. Resolution of each image is  $256 \times 256$  pixels.

### 3.7 Influence of porogen content on the porous structure of HEMA-EDMA monoliths

The porous structure of a polymer is strongly dependent on the porogenic solvent. In this work, HEMA-EDMA monoliths with different size of polymer particles were prepared by varying the content of porogenic solvents in pre-polymer mixtures. During polymerization, polymer particles are formed by phase separation due to limited solubility of a polymer in porogenic solvent [160, 198]. Therefore, the porous properties can be tuned by using various porogens with different solubility parameters between the polymer and the solvent [199, 200]. Being a poor solvent for HEMA-EDMA, cyclohexanol leads to the formation of small polymer particles, while 1-decanol is a good solvent for HEMA-EDMA in that it tends to the formation of larger polymer particles [159, 160, 201]. In order

to tune the porous properties of HEMA-EDMA, different ratios of cyclohexanol and 1-decanol were used as pore-forming solvents in the polymerization mixture. The ratio of porogens to monomer (HEMA) and cross-linker (EDMA), i.e. porosity of monolith, was kept constant, 60 wt. % for all pre-polymer mixtures.

Six polymerization mixtures with varying proportions of cyclohexanol and 1-decanol were prepared. All mixtures contained 24% (wt.) monomer 2-hydroxyethyl methacrylate, 16% (wt.) cross-linker ethylene dimethacrylate, 1% (w/w, with respect to the monomer and cross-linker) initiator 2,2-dimethoxy-2-phenylacetophenone and 60% (wt.) porogens cyclohexanol and 1-decanol (Table 3.1). The weight percentage of 1-decanol in the polymerization mixture was 0% in mixture 1 (pure cyclohexanol as the sole solvent), 10% in mixture 2, 12% in mixture 3, 15% in mixture 4, 20% in mixture 5, 30% in mixture 6. These polymerization mixtures were then used to prepare 12,5  $\mu\text{m}$  thick polymer layers on glass substrates by UV-initiated free-radical polymerization.

**Table 3.1.** Content of polymerization mixtures used for preparation of HEMA-EDMA monoliths.

Mixture	Initiator (DMPAP), %wt.*)	Monomer (HEMA), %wt.	Cross-linker (EDMA), %wt.	Porogens, %wt.	
				1-decanol	cyclohexanol
Mix 1	1	24	16	0	60
Mix 2	1	24	16	10	50
Mix 3	1	24	16	12	48
Mix 4	1	24	16	15	45
Mix 5	1	24	16	20	40
Mix 6	1	24	16	30	30

\*<sup>)</sup> the percentage (w/w) of the initiator is given with respect to the monomer and cross-linker.

The SEM micrographs of the porous polymer layers shown in Fig. 3.11 confirm the gradual increase in the size of microglobules and pores as the 1-decanol content of the polymerization mixture was increased. The average pore sizes for the porous polymers obtained from mixtures 1-6 are 136, 133, 158, 184, 362, and 1403 nm, respectively. The microglobules consist of smaller particles fused with each other. The average sizes of a

sole microparticle for mixtures 1-6 were 35, 34, 36, 40, 63, and 213 nm, respectively (Table 3.2).

**Table 3.2.** Porous properties of HEMA-EDMA monoliths.

Mixture	Content of porogens, % wt.		Pore size <sup>a</sup> , nm	Particle size <sup>a</sup> , nm	Globule size <sup>b</sup> , nm
	1-decanol	cyclohexanol			
Mix 1	0	60	136±35	35±6	357±28
Mix 2	10	50	133±51	34±5	411±27
Mix 3	12	48	158±35	36±6	447±33
Mix 4	15	45	184±37	40±5	462±25
Mix 5	20	40	362±80	63±10	466±15
Mix 6	30	30	1403±217	213±26	583±35

<sup>a</sup>measured by SEM

<sup>b</sup>measured by DLS

The porous structure of polymer surfaces was observed by using SEM. In order to examine porous properties in the bulk polymer, DLS measurement was employed. The monolith matrix is composed of polymer particles fused together. By using DLS the average size of the polymer microglobules was evaluated (Fig. 3.12, 3.13). To this end, the polymers were gently removed from the glass support into individual Eppendorf tubes followed by sonication in an ultrasonic bath at a room temperature. This procedure helped to disintegrate the monolithic structure of the polymer into individual polymer particles that could be characterized by DLS. Afterwards, the autocorrelation functions and corresponding sizes of particles were measured by a Zetasizer Nano (Malvern, UK). The mean values of the microglobules size for porous polymers obtained from mixtures 1-6 are 357, 411, 447, 462, 466, and 583 nm, respectively (Table 3.2). Thus, by decreasing the weight ratio of cyclohexanol to 1-decanol in the polymerization mixture and keeping the amounts of monomer and cross-linker unchanged, the significant increase of both the pore and the globule size of the polymer were achieved.

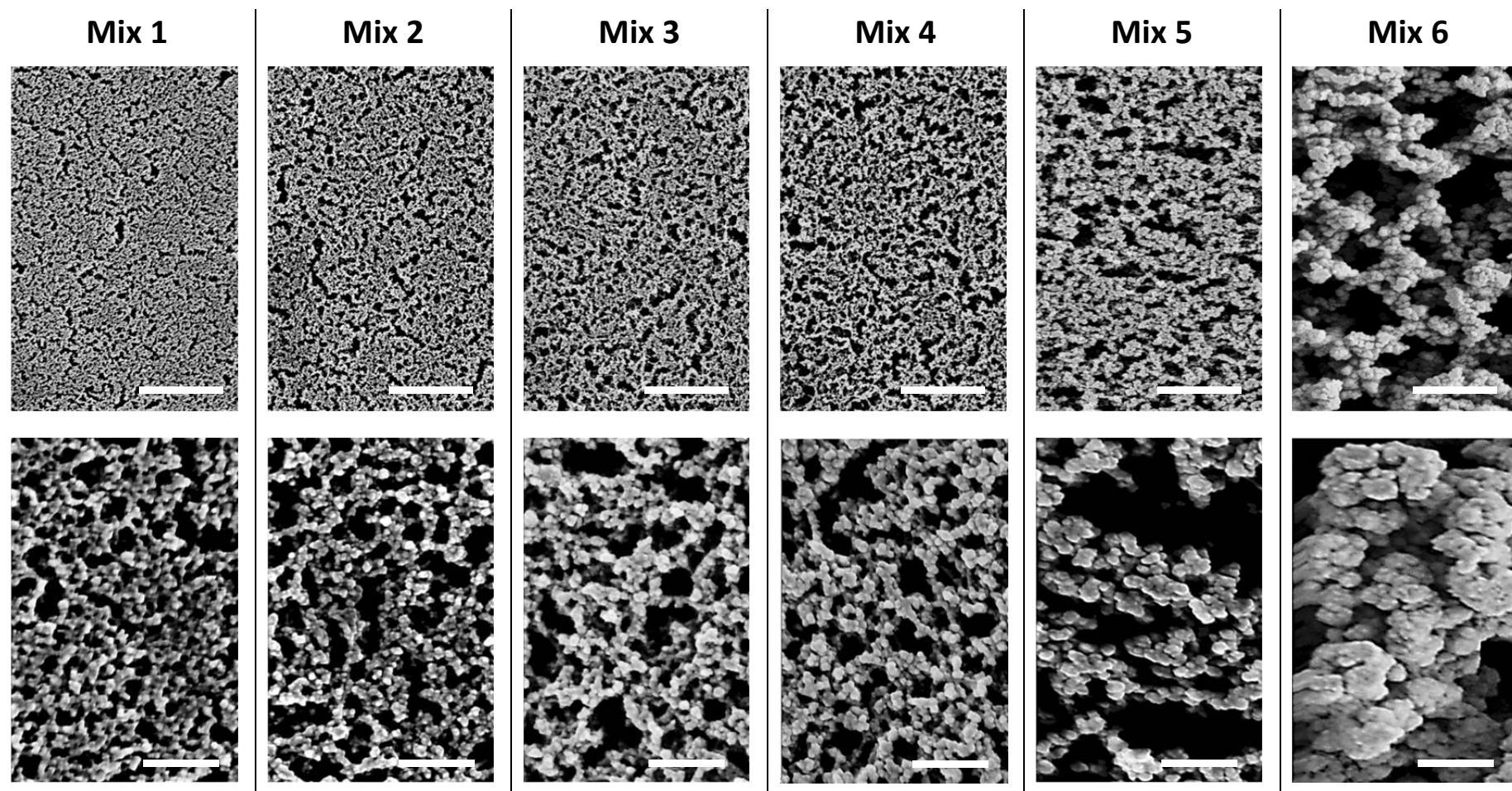


**Fig. 3.11.** SEM micrographs of HEMA-EDMA polymer monoliths with different content of porogens in the polymerization mixture. See Table 3.1 for the compositions and Table 3.2 for the quantification of the porous structure. Scale bars are 2  $\mu\text{m}$  (top) and 400 nm (bottom).

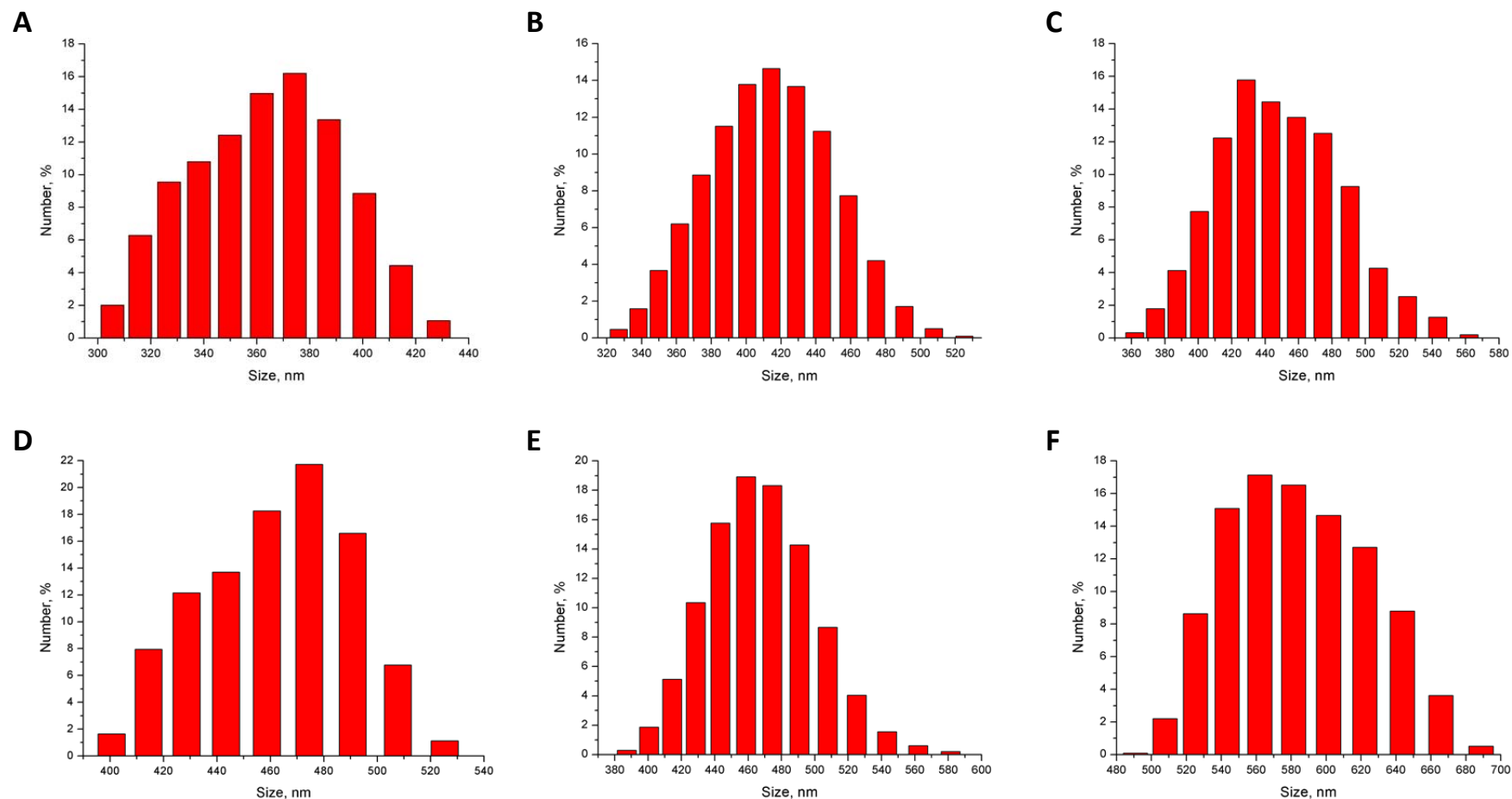


**Fig. 3.12.** Size distribution of the polymer particles produced by disintegration of the matrix of poly(2-hydroxyethyl methacrylate-*co*-ethylene dimethacrylates) with different porous structures. Polymers were produced by varying the content of porogens in the polymerization mixture. The microglobule size of the polymers is increased from A to F by changing the composition of the polymerization mixtures, with A to F corresponding to the mixtures 1 to 6, respectively. The globule size was determined by DLS.

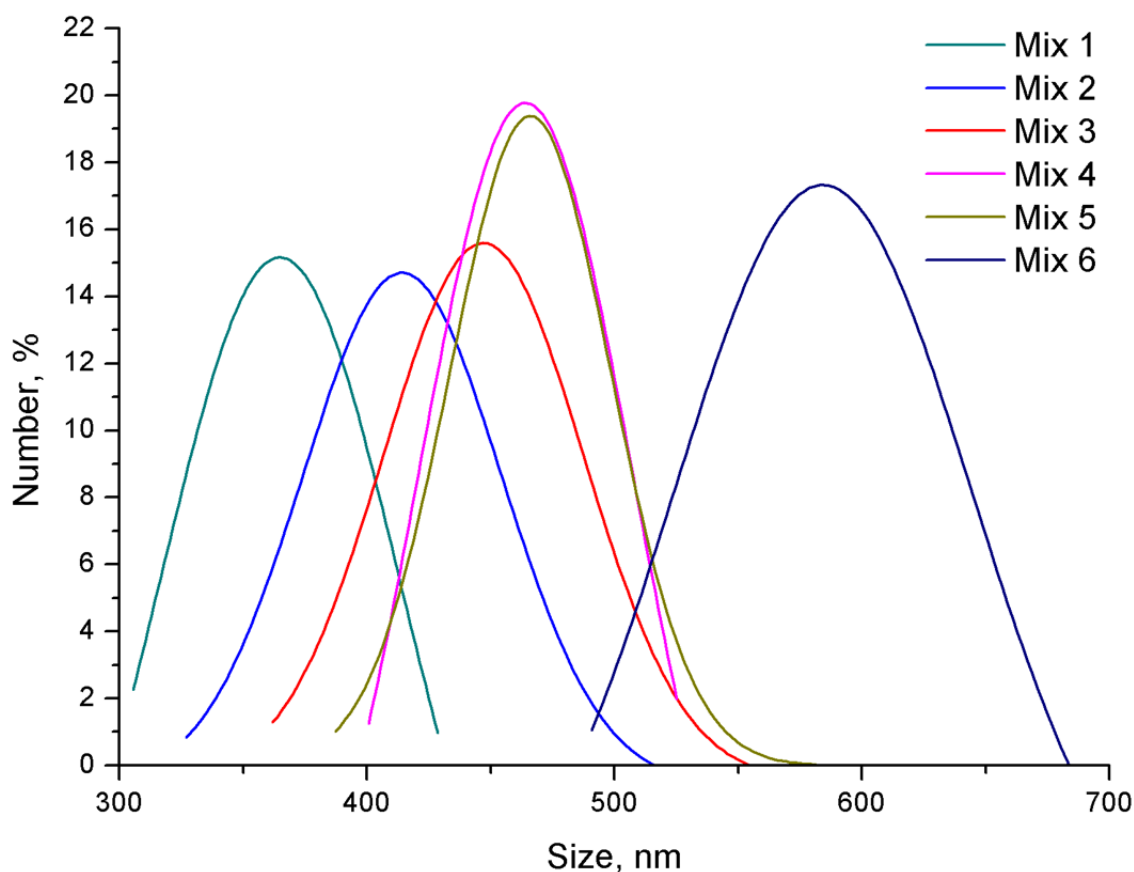


**Fig. 3.13.** Gaussian curves approximating size distribution of polymer particle in the bulk monoliths obtained from the polymerization mixtures 1–6 (Table 3.1). The full width at half maximum of Gaussian fits are 113  $\mu\text{m}$  (Mix 1), 94  $\mu\text{m}$  (Mix 2), 100 (Mix 3), 102 (Mix 4), 77  $\mu\text{m}$  (Mix 5) and 142 (Mix 6).

### 3.8 Influence of porous structure on transparency of HEMA-EDMA polymer films

The transparency of polymethacrylate monoliths depends significantly on their porous structure, in particular, on the size of polymer globules that scatter the incident light [200]. In turn, the size of globules can be varied by changing the content of porogens [159, 201].

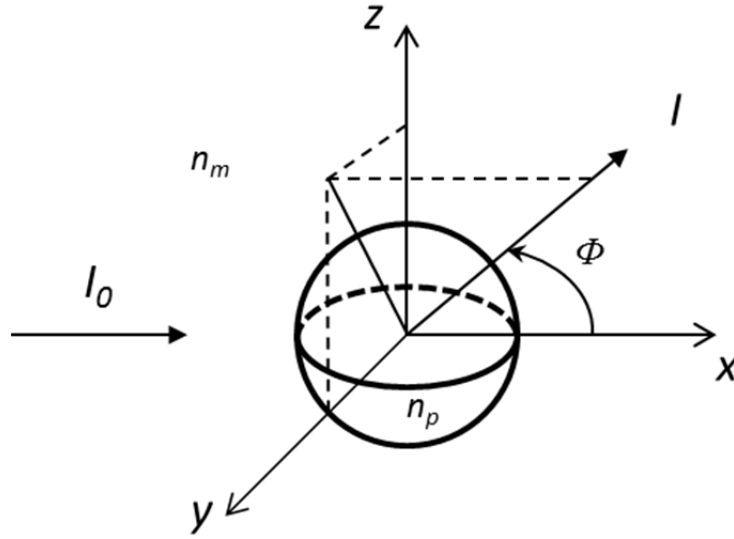


**Fig. 3.14.** Coordinate geometry for Rayleigh and Mie scattering.

The light scattering takes place when an incident light ray encounters an obstacle or non-homogeneity in medium (Fig. 3.14). The formal theoretical description may be categorized in terms of two frameworks: *Rayleigh* and *Mie scattering theory* [202-204]. The implementation of one or another theory relies on the size of scattering particles and wavelength of the incident light, which is defined as dimensionless parameter  $\alpha$ :

$$\alpha = \frac{\pi d}{\lambda} \quad (1)$$

where  $d$  is the diameter of the scattering particle,  $\lambda$  is wavelength of the incident light. The criterion for Rayleigh scattering is  $\alpha \ll 1$ . In this case, the size of scattering particles is sufficiently smaller than the wavelength of the incident electromagnetic irradiation. The scattered light intensity,  $I$ , can be described by the following equation:

$$I = I_0 \frac{1 + \cos^2 \Phi}{2L^2} \left( \frac{2\pi}{\lambda} \right)^4 \left( \frac{n^2 - 1}{n^2 + 2} \right)^2 \left( \frac{d}{2} \right)^6 \quad (2)$$

where  $I_0$  is the intensity of the incident light,  $\Phi$  is the scattering angle,  $L$  is the distance from the scattering particle to the observation point,  $n$  is the relative refractive index.

$$n = \frac{n_p}{n_m} \quad (3)$$

where  $n_p$  is refractive index of the scattering particle and  $n_m$  is refractive index of the medium. Generally, the Rayleigh theory is applied for calculation of the scattering intensity when  $d \sim 1 - 100$  nm.

If  $\alpha \geq 1$ , the size of the scattering particle is much larger than the wavelength of the incident electromagnetic irradiation. In this case, the scattering of light can be described by Mie theory, and the intensity of scattered light is given by the equation:

$$I = I_0 \frac{\lambda^2}{8\pi R^2} (i_1 + i_2) \quad (4)$$

where  $i_1$  and  $i_2$  are Mie scattering parameters, with are infinity series given by:

$$\begin{cases} i_1 = \left| \sum_{k=1}^{\infty} \frac{2k+1}{k(k-1)} (a_k \pi_k(\cos \Phi) + b_k \tau_k(\cos \Phi)) \right|^2 \\ i_2 = \left| \sum_{k=1}^{\infty} \frac{2k+1}{k(k-1)} (a_k \tau_k(\cos \Phi) + b_k \pi_k(\cos \Phi)) \right|^2 \end{cases} \quad (5)$$

$\pi_k, \tau_k$  are angular functions, which are the first order of Legendre function ( $P_k^1$ ):

$$\begin{cases} \pi_k = \frac{P_k^1(\cos \Phi)}{\sin \theta} \\ \tau_k = \frac{d(P_k^1(\cos \Phi))}{d\theta} \end{cases} \quad (6)$$

$a_k$  and  $b_k$  are Mie coefficients:

$$\begin{cases} a_k = \frac{\Psi_k(z)\Psi_k'(nz) - n\Psi_k(nz)\Psi_k'(z)}{\xi_k(z)\Psi_k'(nz) - n\Psi_k(nz)\xi_k'(z)} \\ b_k = \frac{n\Psi_k(z)\Psi_k'(nz) - \Psi_k(nz)\Psi_k'(z)}{n\xi_k(z)\Psi_k'(nz) - n\Psi_k(nz)\xi_k'(z)} \end{cases} \quad (7)$$

$\Psi_k$  and  $\xi_k$  are Ricatt-Bessel functions, which are defined in terms of the half-integer-order Bessel function of the first kind ( $J_{k+1/2}$ ):

$$\begin{cases} \Psi_k(z) = \sqrt{\frac{\pi z}{2}} J_{k+1/2}(z) \\ \xi_k(z) = \sqrt{\frac{\pi z}{2}} H_{k+1/2}(z) = \Psi_k(z) + iX_k(z) \end{cases} \quad (8)$$

$H_{k+1/2}$  is the half-integer-order Henkel function of the second kind, where  $X_k$  parameter is defined in terms of the half-integer-order Bessel function of the second kind ( $Y_{k+1/2}$ ):

$$X_k(z) = -\sqrt{\frac{\pi z}{2}} Y_{k+1/2}(z) \quad (9)$$

Finally, the intensity of scattering cross-section can be described as:

$$I = I_0 \frac{\lambda^2}{2\pi R^2} \sum_{k=0}^{\infty} (2k+1) (|a_k|^2 + |b_k|^2) \quad (10)$$

In order to obtain a transparent HEMA-EDMA polymer film, the scattering of the incident light should be minimized. The sizes of the polymer globules of the HEMA-EDMA monoliths, prepared by using polymerization mixture 1–6 (Table 3.1), vary in the range of 300–600 nm (Table 3.2). Therefore, the parameter  $\alpha > 1$  for all wavelengths in UV-Vis range and the scattering of the incident light can be estimated in terms of the *Mie scattering theory*. By using equations (7-10) assuming a spherical shape of the polymer particles and Mie-scattering regime, the spectra of light transmittance were simulated [171-175]. Fig. 3.15 and Fig. 3.16 show the transmittance spectra (dashed lines) of the particles in air and water mediums. The decrease of the polymer globules size leads to a gradual decrease the transmittance first in UV-Vis and then in NIR-range for both media. The calculated transmittance for distinct wavelengths corroborates with the obtained spectra (Table 3.3, 3.4).

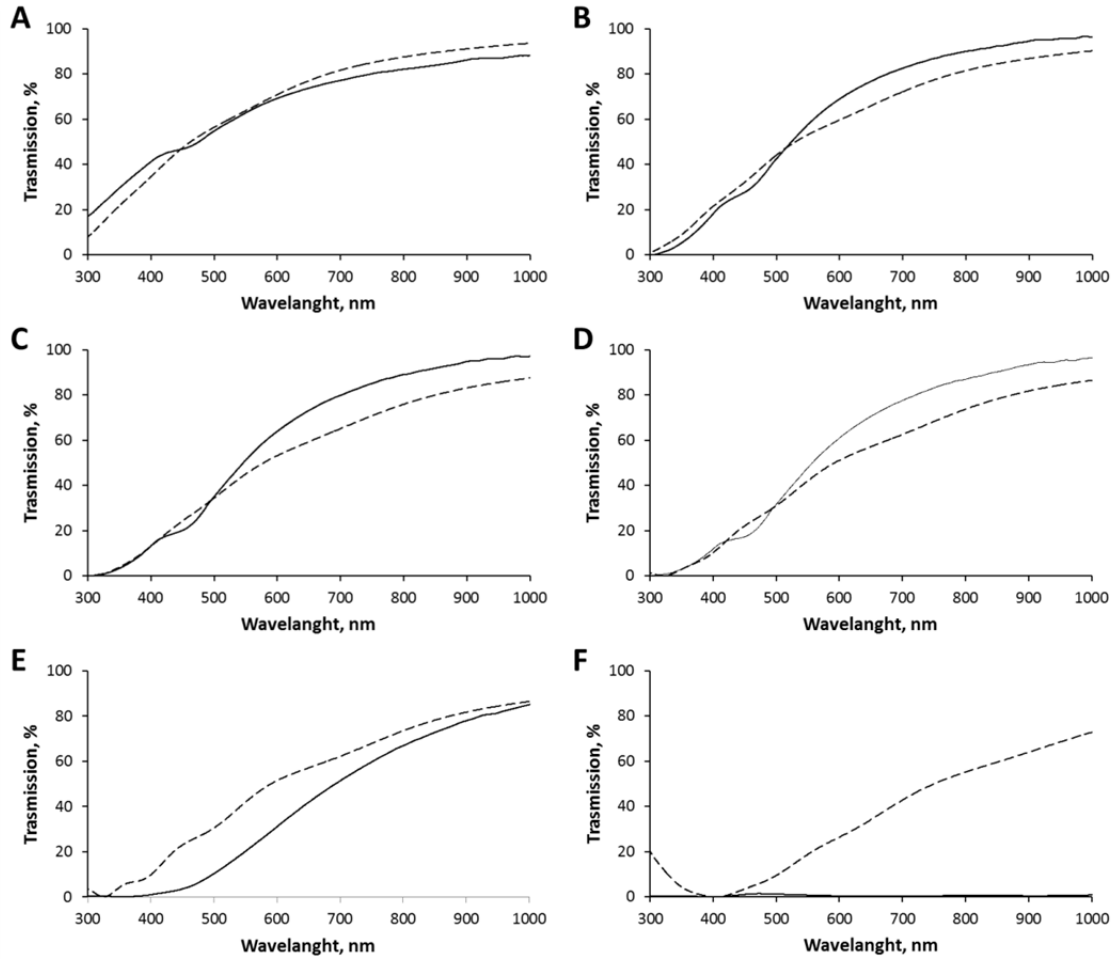


**Fig. 3.15.** UV-NIR transmission spectra of HEMA-EDMA polymer films in air. Globules and pore size of the monoliths are reduced by changing the composition of the polymerization mixture, with (A) to (E) corresponding to the mixture 1 to 6 (Table 3.1), respectively. Solid and dashed lines correspond to the experimental and simulated data, respectively. Thickness of the layers is 12,5  $\mu\text{m}$ . Porosity of the polymers is 60 %.

**Table 3.3.** Comparison of the light transmission by polymer particles obtained experimentally and estimated by using the theoretical approximation. Samples are in air.

	$\lambda=400\text{ nm}$			$\lambda=650\text{ nm}$			$\lambda=1000\text{ nm}$		
	$D_{exp}$ , %	$D_{sim}$ , %	dev., %	$D_{exp}$ , %	$D_{sim}$ , %	dev., %	$D_{exp}$ , %	$D_{sim}$ , %	dev., %
Mix 1	41,3	34,7	-16,0	73,8	77,1	+4,5	88,1	93,6	+6,2
Mix 2	18,2	21,6	+18,7	76,8	66,0	-14,1	96,2	90,2	-6,3
Mix 3	13,3	13,2	-0,8	73,2	59,3	-19,0	97,1	87,5	-9,9
Mix 4	11,9	10,3	-13,5	70,5	57,1	-19,0	96,3	86,5	-10,4
Mix 5	1,0	9,8	+89,8	41,9	57,1	+15,2	85,0	86,4	+1,7
Mix 6	0,1	0	—	0,4	34,3	+8475	0,9	72,8	+7988

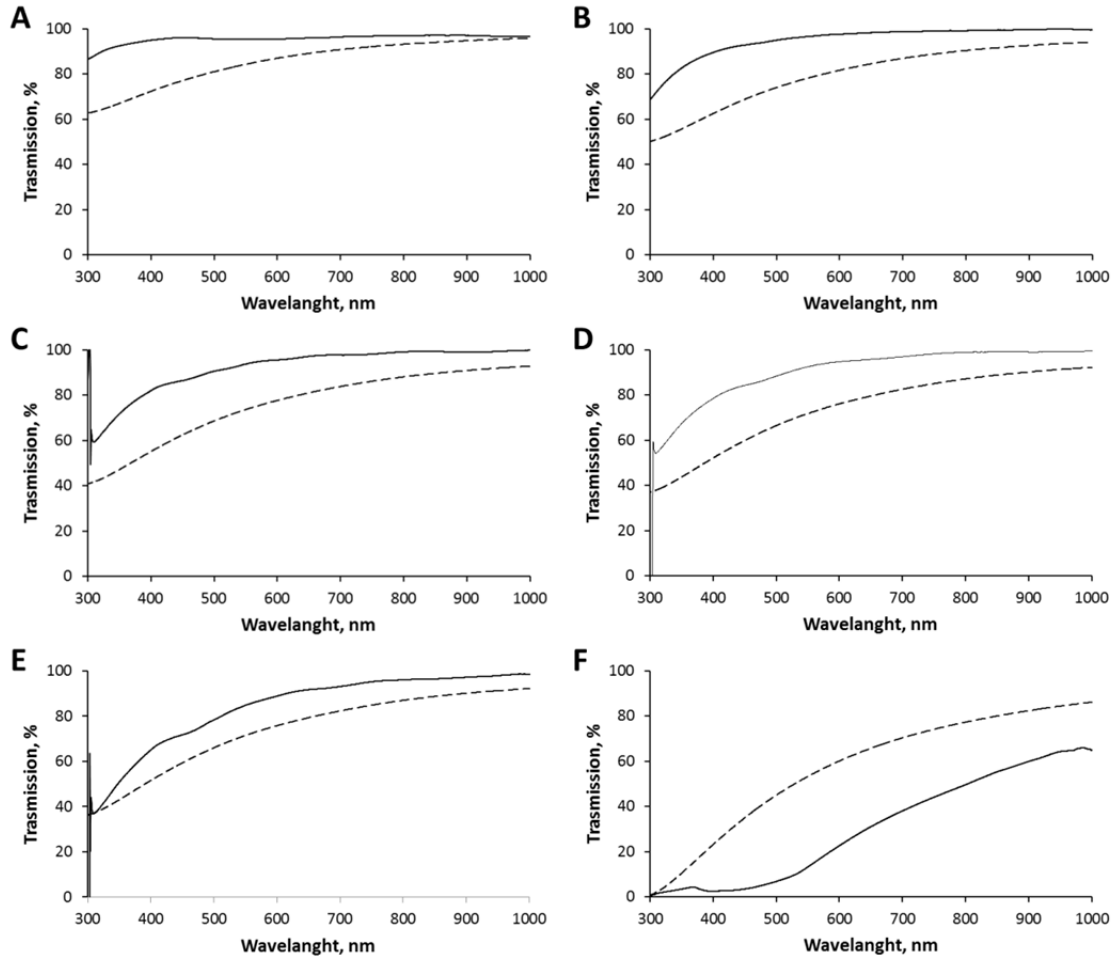


**Fig. 3.16.** UV-NIR transmission spectra of HEMA-EDMA polymer films in water. Globules and pore size of the monoliths are reduced by changing the composition of the polymerization mixture, with (A) to (E) corresponding to the mixture 1 to 6 (Table 3.1), respectively. Solid and dashed lines correspond to the experimental and simulated data, respectively. Thickness of the layers is 12,5  $\mu\text{m}$ . Porosity of the polymers is 60 %.

**Table 3.4.** Comparison of the light transmission by polymer particles obtained experimentally and estimated by using the theoretical approximation. Samples are in water.

	$\lambda=400\text{ nm}$			$\lambda=650\text{ nm}$			$\lambda=1000\text{ nm}$		
	$D_{exp}$ , %	$D_{sim}$ , %	dev., %	$D_{exp}$ , %	$D_{sim}$ , %	dev., %	$D_{exp}$ , %	$D_{sim}$ , %	dev., %
Mix 1	94,9	72,4	-23,7	95,9	89,1	-7,1	96,5	95,9	-0,6
Mix 2	89,6	62,6	-30,1	98,3	84,6	-13,9	99,5	94,1	-5,4
Mix 3	82,0	55,2	-32,7	97,1	81,0	-16,6	99,9	92,8	-7,1
Mix 4	78,5	52,2	-33,5	95,7	79,6	-16,8	99,5	92,2	-7,3
Mix 5	65,0	51,6	-20,6	91,6	79,3	-13,4	98,4	92,1	-6,4
Mix 6	2,5	23,2	+20,7	31,1	65,8	+111,6	65,1	86,1	+32,3

Fig. 3.17 shows the photographs of the polymer films prepared on a glass support both in the dry state and impregnated with water. The corresponding transmittance spectra of the dry and wet samples were measured by using a spectrophotometer. The resulted transmittance spectra (solid lines, Fig. 3.15, 3.16) represented the same regularities as the theoretically estimated spectra that are the rise of globule sizes results in decrease of the transmittance of light initially in UV-Vis and latter in NIR-range. The transmittance values for distinct wavelengths are represented in Table 3.3 and Table 3.4 for air and water mediums, respectively.

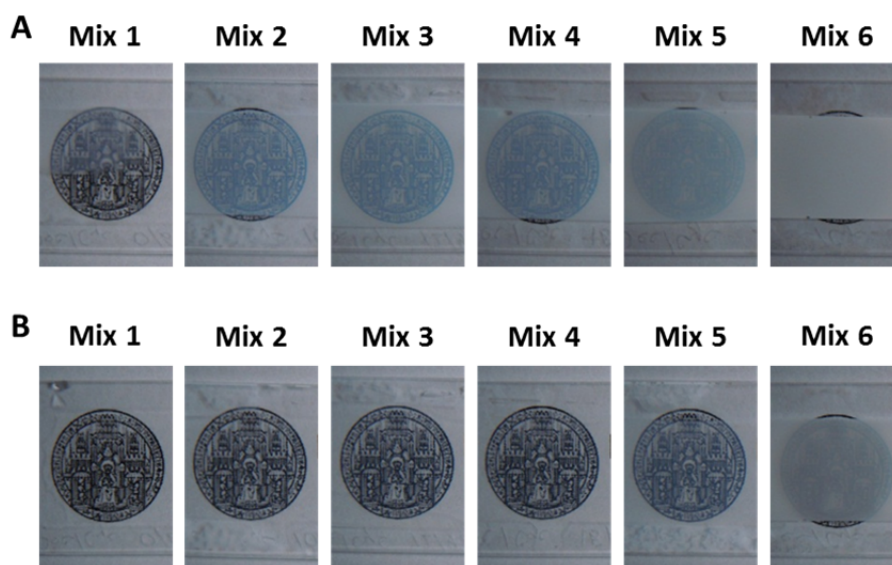


Fig. 3.17. Photographs showing relative transparency of HEMA-EDMA layers obtained from mixtures 1-6 on glass supports. (A) Polymer layers in dry state. (B) Polymer layers wetted by water.

Although the theoretically and experimentally obtained spectra of transmittance showed the same regularities, the discrepancy of theory and experimental data was found in the range of 1-25 % for the transmittance values in case of air medium, and 1-35 % for the transmittance values in case of water medium (Table 3.4, 3.5) for the polymers obtained for the polymerization mixtures 1-5. For the polymer obtained from the polymerization mixture 6 the simulation was inadequate to the experimental results. The mismatch between the simulations and experiments can be associated with the non-ideal spherical shape of the polymer globules (Fig. 3.11), which leads to a wrong estimation of scattering by the *Mie theory*, because the theory only applies to a spherical shape of scattering particles. Furthermore, the theory is based on the assumption that the small spherical particles are distributed in a medium, whereas the polymer globules are fused

with each other and still in the polymer matrix. Moreover, the simulations were performed regardless the thickness and bulk properties of the polymer films. Finally, the incident light is scattered by particles with a continuum of polymer particles sizes, while the simulations include only fifty discrete number of particle sizes within the calculated standard deviation values.

### 3.9 Influence of porous structure on the wetting properties of HEMA-EDMA polymer films

The combination of material chemistry and surface morphology influences on the surface wetting properties [205, 206]. Therefore, the change in the morphology of porous polymers should alter the hydrophilicity of polymer layers prepared on a glass support [160, 201]. Fig. 3.18 and Table 3.5 show static WCAs for the porous layers obtained from the six polymerization mixtures 1-6. The increase in the size of pores and microglobules is accompanied by a drop in  $\theta_{st}$  from 28,5° (Mix 1) to 11,5° (Mix 6). Since the polymerization mixtures consist of equal amounts of the monomer, cross-linker and initiator, the chemical nature of fabricated monoliths is the same and the observed decrease of  $\theta_{st}$  is the result of surface morphology. The increase in hydrophilicity can be explained by the growth of microscale roughness associated with significant increase in the size of the structural features of the polymer films (Table 3.2, Fig. 3.11).

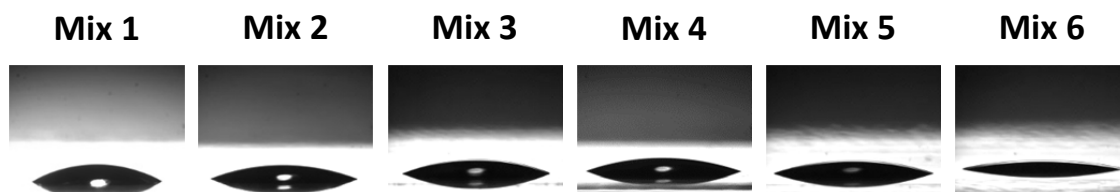


**Fig. 3.18.** Photographs of water droplets on HEMA-EDMA layers obtained from the polymerization mixtures 1-6. The size of globules and pores in the polymers is increased from mix 1 to mix 6.

**Table 3.5.** Static WCAs of HEMA-EDMA polymer layers prepared with different content of porogens in the polymerization mixture.

Mixture	Content of porogens, % wt.		$\theta_{st}$ , nm
	1-decanol	cyclohexanol	
Mix 1	0	60	$28,5^\circ \pm 0,5^\circ$
Mix 2	10	50	$20,1^\circ \pm 0,4^\circ$
Mix 3	12	48	$17,8^\circ \pm 0,3^\circ$
Mix 4	15	45	$17,5^\circ \pm 0,8^\circ$
Mix 5	20	40	$16,0^\circ \pm 0,6^\circ$
Mix 6	30	30	$11,5^\circ \pm 0,3^\circ$

### 3.10 Optimization of the photografting procedure

Our liquid patterning technique is based on filling the hydrophilic HEMA-EDMA area with aqueous solutions, which spread and follow the contour of the hydrophobic PFPMA-coated region. Therefore, the high water repellency of the hydrophobic area ensures the stability of microdroplets inside the hydrophilic areas, being vital for the durability of the liquid patterns during experiments. Since the UV-initiated photografting is a radical process, an increase in the UV-irradiation time should lead to an elevation in the density of PFPMA polymer brushes in the HEMA-EDMA film.

In order to find the optimal duration of the photografting step, we tested different times of UV-irradiation in the range of 1 min to 30 min. During the experiments the intensity and wave length of UV-light were kept constant and equal to  $9 \text{ mW/cm}^2$  and 260 nm, respectively. The HEMA-EDMA film was impregnated with the photografting mixture, followed by covering with 50  $\mu\text{m}$  thick Teflon film. The plate was irradiated with UV-light. After the photografting procedure, the samples were extensively washed with ethanol, dried under compressed air flow and stored at room temperature.

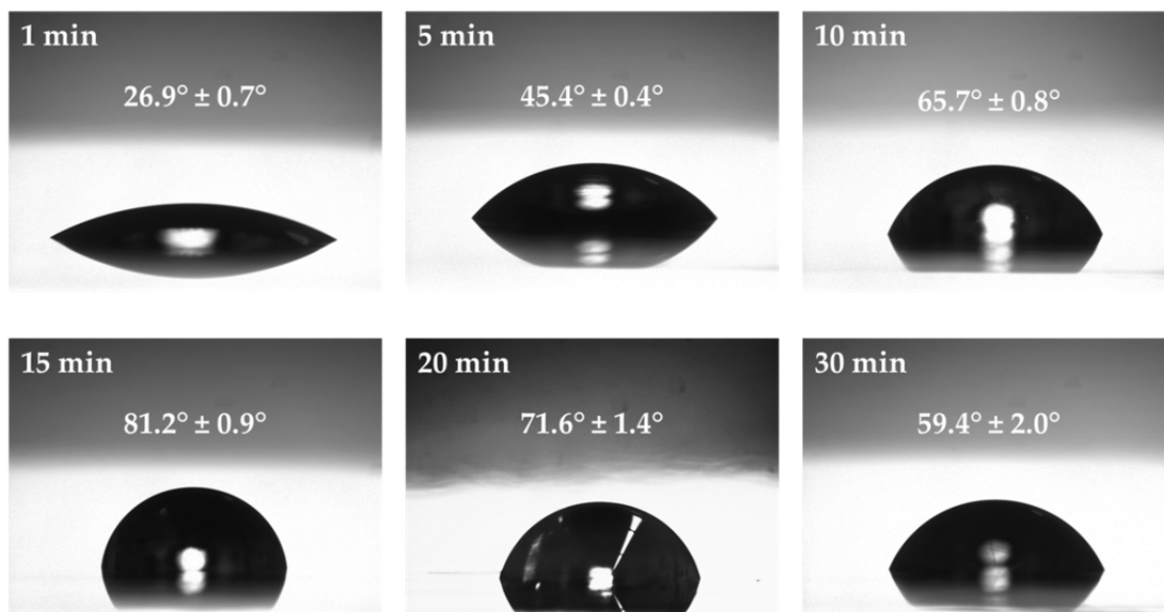


**Fig. 3.20.** Photographs of water droplets and corresponding values of static WCAs of HEMA-EDMA polymer substrate after photografting with PFPMA for different time intervals.

The results of the WCA measurements are shown in Fig. 3.20. The static WCA increased gradually from  $26.7^\circ$  to  $81.2^\circ$ , upon increasing the photografting time from 1 to 15 min. However, a further increase of photografting time led to a decrease of static WCAs to  $71.6^\circ$  and  $59.4^\circ$  after 20 and 30 min of UV-irradiation, respectively. One of the possible explanations for the observed decrease in the hydrophobicity after longer irradiation times is the oxidation of polymer triggered by UV-light. The oxidation should lead to the accumulation of carboxylic groups on the substrate, being the reason for the reduction of WCAs. On the other hand, UV-treatment can also lead to the degradation (depolymerization) of the PFPMA brushes, resulting in the loss of water-repellent properties.

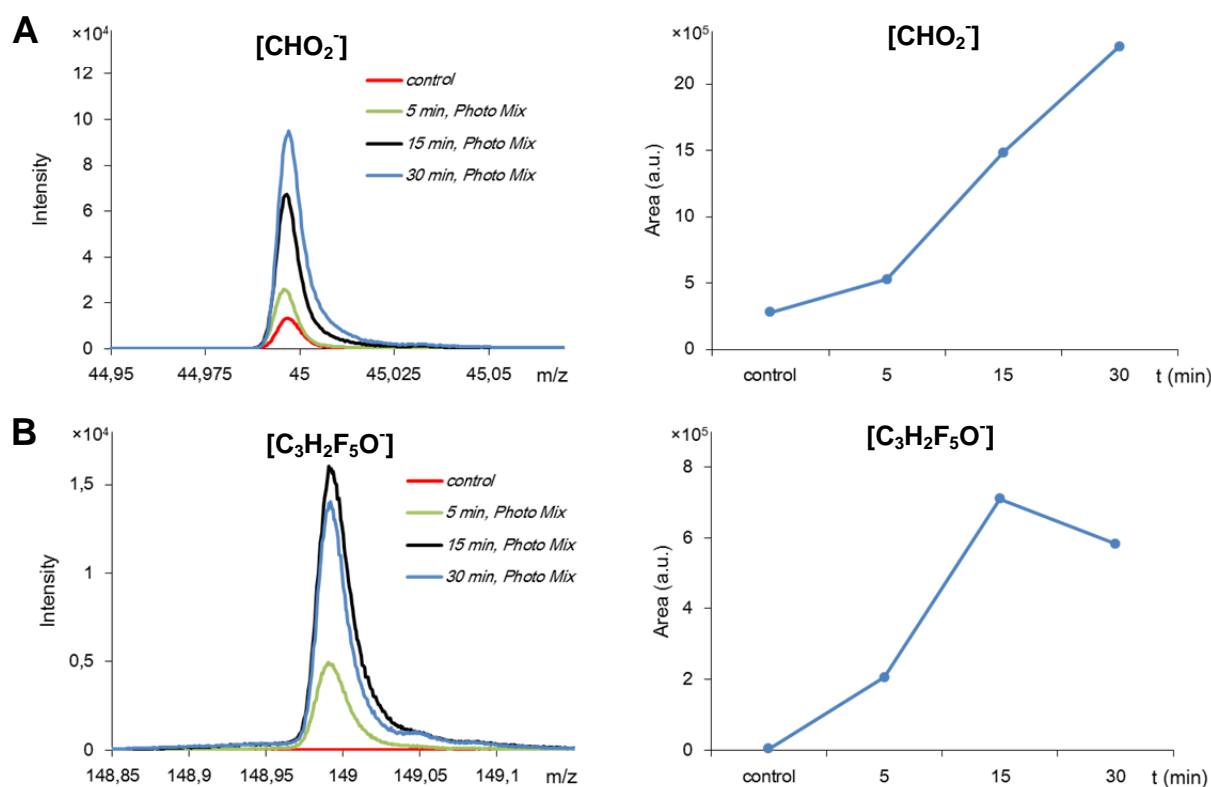


**Fig. 3.21.** Mass spectra  $\text{CHO}_2^-$  (A) and  $\text{C}_3\text{H}_2\text{F}_5\text{O}^-$  (B) peaks (left) and corresponding graphs of peak areas (right). Surfaces were impregnated with the photografting mixture and irradiated with UV light. Untreated HEMA-EDMA substrate was used as a control.

In order to test whether the substrate accumulates carboxylic groups or loses 2,2,3,3,3-pentafluoropropyl residues during the UV-irradiation, the samples photografted for 5, 15 and 30 min were analyzed by ToF-SIMS (Fig. 3.17). A non-treated HEMA-EDMA polymer film was used as a control sample. All samples were measured sequentially in one loading chamber and under the same settings:  $\text{Bi}^{1+}$  25 keV primary ion source, high mass resolution bunched mode, 20 runs of measurement for signal accumulation and  $500 \times 500 \mu\text{m}$  area of measurement. The collected mass spectra indeed showed an increase in  $\text{CHO}_2^-$  peak intensity and peak area with an increase in the photografting time (Fig. 3.21 A). To assess the relative oxidation rate, we calculated the ratio of the peak area of the photografted samples to the peak area of the control sample. The obtained ratios were equal to 1,9, 5,3 and 8,1 corresponding to 5, 15 and 30 min of UV-treatment, respectively. This result confirms the accumulation of carboxylic groups on the surface of the samples that leads to the observed increase of hydrophilicity, and to the drop of WCA values. On the other hand, the intensity of the  $\text{C}_3\text{H}_2\text{F}_5\text{O}^-$  peak, corresponding to the 2,2,3,3,3-pentafluoropropyl ion species, displayed an increase after 5 to 15 min photografting followed by a drop after 15 to 30 min photografting (Fig. 3.21 B). The ratio

of  $C_3H_2F_5O^-$  peak areas of the samples after 15 and 5 min of UV-treatment is equal to 3,5. However, the ratio of  $C_3H_2F_5O^-$  peak areas of the samples after 30 and 15 min of UV-treatment is equal to 0,8. These results indicate the reduction of the density of PFPFMA-residues on the surface after 30 min of UV-irradiation that also contributes to the drop of its hydrophobic properties.

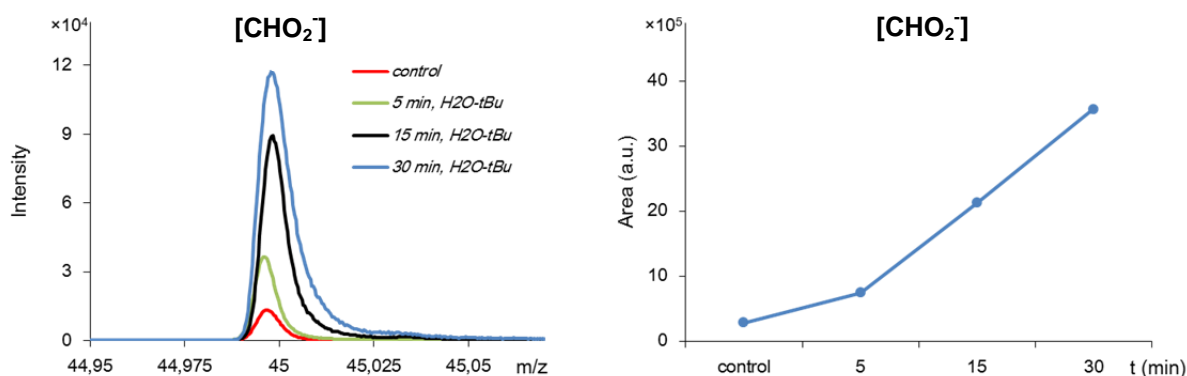


**Fig. 3.22.** Mass spectra  $CHO_2^-$  peaks and corresponding graph of peak areas of the samples that were impregnated with  $H_2O$ -tBu ( $1_v:1_v$ ) mixture. HEMA-EDMA substrate was used as a control.

In addition, to show whether the photografting agent, initiator and cross-linker affect the oxidation process, we substituted the photografting mixture with a  $H_2O$ -tBu mixture ( $1_v:1_v$ ). The UV-treatment and mass spectrometry were performed under the same conditions as described above. A HEMA-EDMA polymer substrate not treated with UV was used as a control sample. As previously, the mass spectra of the samples after UV-treatment showed an increase of  $CHO_2^-$  peak intensity and of the peak area. (Fig. 3.22). The ratios of peak areas of the UV-treated samples after 5, 15 and 30 min to the peak area of the control sample were equal to 2,7, 7,6 and 12,7 respectively. In the case of the impregnation of HEMA-EDMA film with the  $H_2O$ -tBu mixture the oxidation process was 1,4-1,5 times stronger as compared with the photografting mixture. We assumed that the increased oxidation rate is associated with the partial increase of solvents volume, i.e. the amount of dissolved oxygen.

### 3.10 Conclusions

We developed a facile method for rapid generation of liquid patterns with variable 2D geometry. The method is based on the fabrication of hydrophobic micropatterns on a highly hydrophilic surface by photoinitiated surface grafting. The liquid patterns are generated by simple pipetting onto the hydrophilic domains. Due to the extreme difference

in wettability between the highly hydrophilic and hydrophobic regions, the aqueous droplets are immobilized inside the hydrophilic area by surface tension forces. This technique does not require special skills or equipment and is accessible to virtually anyone.

This study also demonstrates the dual influence of the porous structure of HEMA-EDMA monoliths on the transparency and wetting properties of the polymer layers. Although increasing the size of structural monolith features reduces polymer transparency, meanwhile, the adhesion of water is strengthened. It was shown that a longer time of photografting first leads to an increase in hydrophobicity followed by its diminishment, which is associated with the decomposition and oxidation processes.

---

# Chapter 4

## **Micropatterned structures for the simultaneous culture of Multiple Cell Types and the Study of Cell-Cell Communication**

### **4.1 Summary**

The control over spatial arrangement and geometry of different cell types while keeping them separated and in close proximity for a long time is crucial to mimic and study variety of biological processes *in vitro*. Although the existing cell patterning technologies allow co-culturing of different cell types, they are usually limited to relatively simple geometry. The methods used for obtaining complex geometries are usually applicable for patterning only one or two cell types. Here a convenient method for creating patterns of multiple (up to twenty) different cell types on a one substrate is introduced. The method virtually allows any complexity of cell pattern geometry. Cell positioning on the substrate is realized by a parallel formation of multiple cell-containing microreservoirs confined to the geometry of highly-hydrophilic regions surrounded by superhydrophobic borders built-in a fine nanoporous polymer film. As a case study, I in a cooperation with PhD-student Eliana Stangaello and Dr. Steffen Scholpp (ITG, KIT), we showed the cross-talk between two cell populations via Wnt signaling molecules propagation during co-culture in a mutual culture medium.

### **4.2 Introduction**

The ability to culture multiple cell types in separated but adjacent compartments with predefined complex geometries and allowing the communication of these cell lines across the boundary is important to mimic and study variety of biological processes ranging from intercellular communication, cell signaling to tissue engineering and whole organism development [46, 207-209]. Although significant efforts have been made to

develop methods for cell patterning [46, 207], most of the existing techniques are still rather complicated and restricted in the geometry of the possible patterns. In addition, the number and type of cell lines that can be patterned are limited. Thus, the methods based on creating patterns of either cell repellent or cell adhesive regions [158, 210-213] usually allow patterning of either one or two cell types [158, 210-219]. Methods relying on the physical confinement of cells to certain regions using microfluidic devices [220, 221], micromechanical devices [222, 223] or using microwells [224, 225] make culturing of separated cell groups on the same substrate possible, however, are usually limited to simple geometries or laborious in usage.

Tissue development and cell differentiation during the early stages of the embryonic development are good examples of important biological processes that involve and depend on the organization of multiple cell types into complex micropatterns *in vivo*. Proper development requires further communication between these pre-patterned cell populations. In parallel, cells have to acquire positional information related to their location with respect to tissue boundaries. Indeed, the position of compartment boundaries coincides often with organizing cell groups. These organizers orchestrate patterning of cell populations across the border by the controlled release of signaling molecules. A well-characterized example for this process is the development of the thalamus orchestrated by the mid-diencephalic organizer [226]. Wnts proteins are one of the major signaling classes emitted from these organizing boundary zones [227, 228]. Interestingly, the spreading mechanism of the highly lipophilic Wnt molecules remains under debate. The suggested propagation mechanisms can be grouped into two categories: Wnt molecules are transported intercellularly which requires direct cell-cell contact or Wnt molecules are detached from cells and propagated independently in the extracellular space of a tissue [229]. The technical limitations of the existing methods, however, make it difficult or impossible to mimic such processes *in vitro*. To our knowledge, there are no methods allowing for a long term cultivation of more than three different cell types in separated but adjacent compartments with precise geometries without intermingling and simultaneously allowing the communication of these cell pools across the boundary. We used the developed method to visualize spreading of signaling molecules (Wnt) from one compartment and detect the response by activation of a reporter system in the cells pre-patterned in the adjacent compartment.

### 4.3 Cell patterning procedure

The produced patterns can be used to confine cell-containing solutions to the highly hydrophilic regions thereby creating multiple culture reservoirs with predefined geometries on the same substrate (Fig. 4.1). These reservoirs can be further then employed for a simultaneous cultivation of different cell types.

At first different cell suspensions are pipetted into separated hydrophilic compartments. Cells cultured inside separated reservoirs adhere to the hydrophilic polymer surface, forming a pattern of cell monolayers with geometries defined by the photomask (Fig. 4.1 A). Afterwards, the substrate is washed out of non-adherent cells and placed into conjoint culture medium for further co-cultivation of the cells pre-patterned in predefined geometrical regions without cell intermingling (*vide infra*). The distance between the microreservoirs, controlled by the width of the superhydrophobic barrier, can be as low as 50  $\mu\text{m}$ , i.e. comparable to the size of a single cell. Several examples of multiple cell types co-culturing is shown on Fig. 4.1 B. The developed methods cell patterning allows co-culturing up to tens of different cell lines in a close proximity. Creation of such kind of multi-cell type networks can lead to the formation of complex cellular chains for investigation of very complex biological processes, involving multiple cell-cell communications.

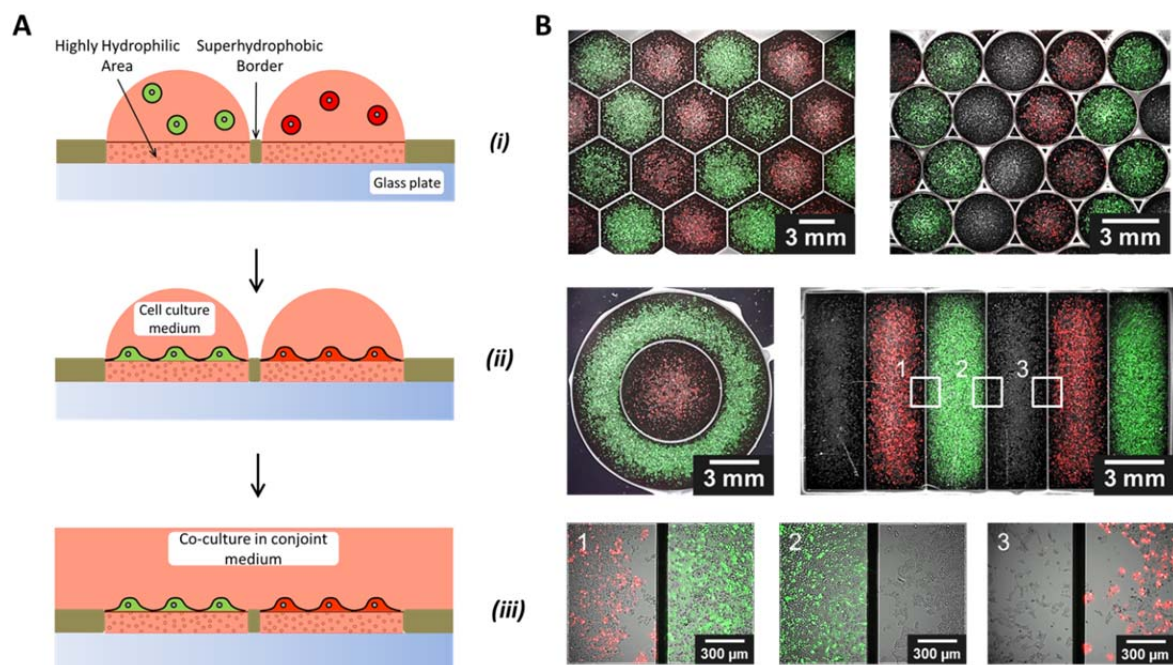


**Fig. 4.1.** (A) Schematics of cell patterning procedure. (i) Different cell suspensions are added into the highly hydrophilic areas, forming droplets with suspended cells. (ii) After seeding cells are settled down and adhere to the substrate. (iii) Adhered cells are placed in

conjoint medium. Cells compartments are connected and superhydrophobic borders serve as lineage restriction borders. (B) Combined bright-field and fluorescence micrographs of different cell lines patterned (red fluorescent MLTy-mCherry, green fluorescent HeLa-GFP and non-fluorescent HEK 293 cell lines) in various geometries. The superhydrophobic border is 100  $\mu\text{m}$ . Cells were co-cultured during 24 h.

The main limitation of the method is the maximum volume of cell-containing reservoirs, which is limited by possible overlapping of neighboring droplets. In this work the optimal ratio of cell suspension volume to pattern area was 50  $\mu\text{l}/\text{cm}^2$ . This ratio enabled uncomplicated handling of patterned substrates and assured the stability of cell suspensions in micro-reservoirs during manipulations.

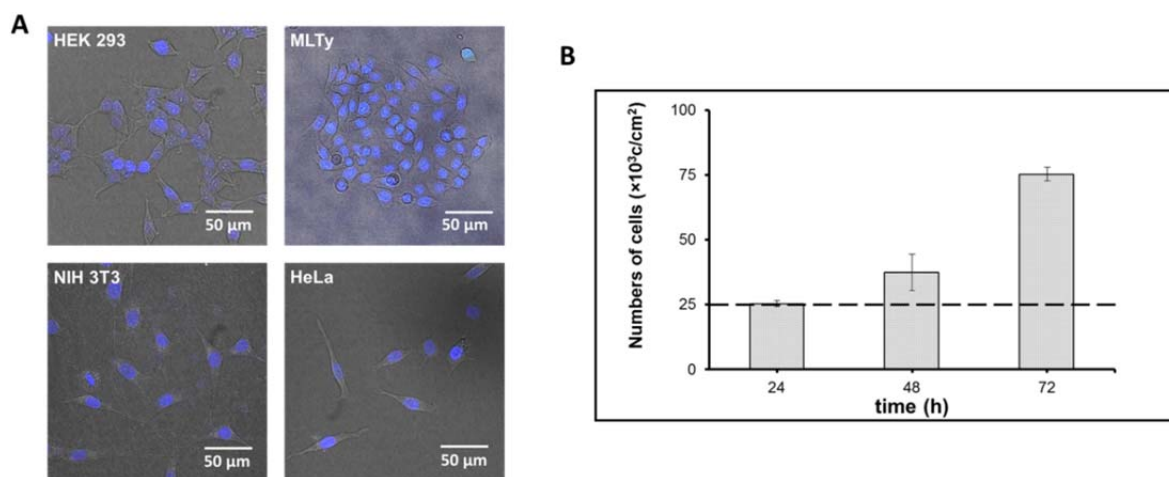


**Fig. 4.2.** Cell viability on HEMA-EDMA polymer. (A) Confocal fluorescence micrographs of Hoechst-stained cells cultured on highly hydrophilic HEMA-EDMA polymer film. Images were obtained after 72h culturing. (B) Number of HEK 293 cells on the highly hydrophilic HEMA-EDMA polymer film cultured for 24, 48 and 72 h.

Cell viability is an important criterion for successful implementation of polymeric surfaces in biological applications. Poly(2-hydroxyethyl methacrylate) [160, 230] and its derivatives [230-232] are well-known biocompatible materials. We tested of the produced nano-porous HEMA-EDMA polymer film for its biocompatibility by culturing several conventional cell lines on the polymeric substrate (Fig. 4.2 A). All tested cell lines showed good spreading and adhesion to the substrate during 3 days of cultivation. Additionally, we tested proliferation of HEK 293 cells on HEMA-EDMA substrate (Fig. 4.2 B). The number

of adherent cells was gradually increasing during 72 h of culturing, thereby confirming good compatibility of the substrate for the cell culture.

#### 4.4 Cross-contamination of cell patterns during co-culturing

Development of an organism requires the emergence of organized tissues from an initially very simple group of cells. During development, mechanisms must exist to keep individual tissues separated and to ensure proper differentiation and growth [233]. One of the mechanisms is the formation and maintenance of cell lineage boundaries to compartmentalize tissues. These compartment boundaries are needed to prevent the intermingling of cells that are fated to contribute to different parts of the embryo [234].

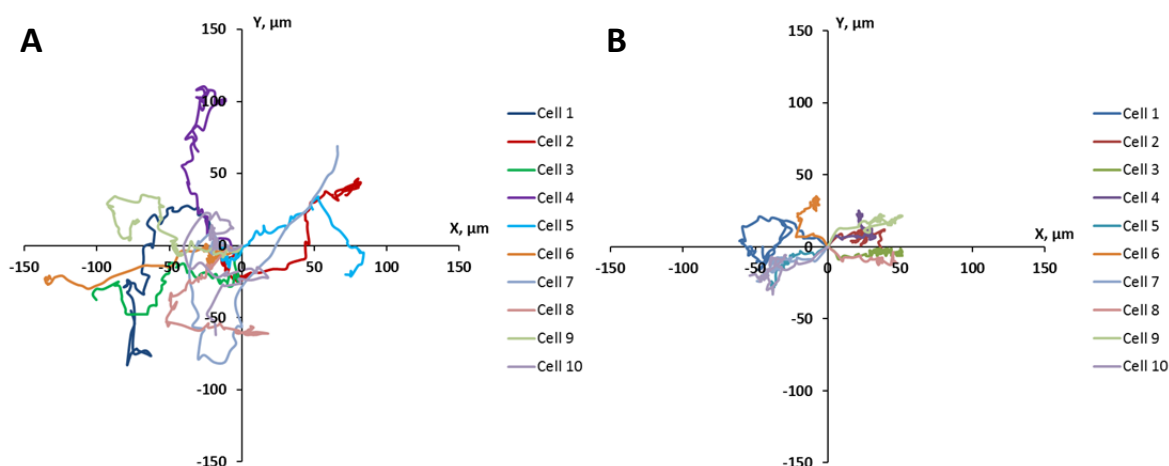


**Fig. 4.3.** Trajectories of HeLa-EGFP cells on (A) HEMA-EDMA and (B) polystyrene surfaces for 24 h.

**Table 4.1.** Parameters of HeLa-EDFP cell motility on HEMA-EDMA and polystyrene substrates.

	Trajectory length, $\mu\text{m}$	Displacement, $\mu\text{m}$	Speed, $\mu\text{m/h}$	Translocation, $\mu\text{m/h}$
HEMA-EDMA	$222 \pm 44$	$97 \pm 30$	$9.3 \pm 1.9$	$4.0 \pm 1.3$
Polystyrene	$122 \pm 35$	$50 \pm 11$	$5.1 \pm 1.6$	$2.1 \pm 0.5$

To estimate the cell motility, green fluorescent cervical cancer cells (HeLa-EGFP) at concentration  $5 \cdot 10^3$  cells/cm<sup>2</sup> were seeded on HEMA-EDMA substrate and monitored during 24 h by time-lapse microscopy. As a control, HeLa-EGFP cells at the same concentration were monitored on polystyrene surface of a cell culture 12-well plate.

Fig. 4.3 shows trajectories of cells during 24h of culturing on the substrates. The average values of trajectory length, displacement from the initial position, cell speed and translocation, which is defined as the ratio of displacement to time, were calculated (Table 4.1). These cell motility parameters obtained from HEMA-EDMA substrate exceed those obtained from polystyrene in 1,8-1,9 times in that cells were more motile on HEMA-EDMA substrate that can be associated by the change of surface roughness and wettability properties of substrate.

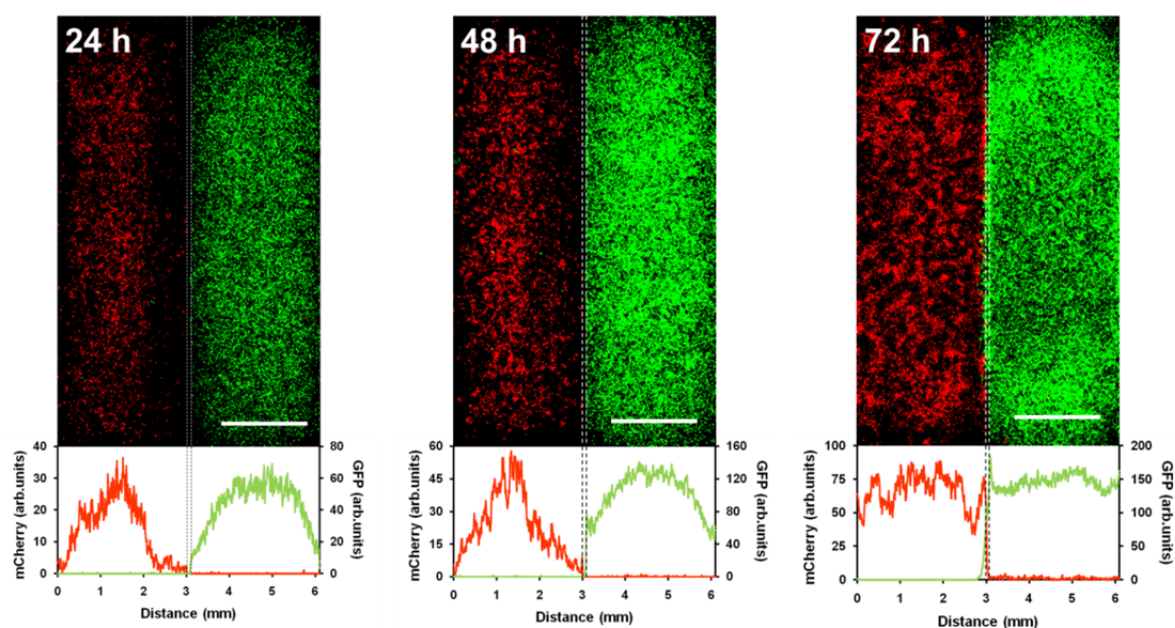


**Fig. 4.4.** Cross-contamination of cell patterns during co-culturing. Fluorescence microscope images and fluorescence intensity plots of MLTy-mCherry (red) and HeLa-GFP (green) cells patterned inside adjacent rectangular highly hydrophilic areas ( $3 \times 10$  mm) separated by a  $100 \mu\text{m}$  superhydrophobic border. Images were taken 24 h, 48 h and 72 h post connection. Scale bar is 2 mm.

To test if the effectiveness of the hydrophobic borders to prevent cell migration is comparable to a biological compartment boundary, we quantified migration of MLTy-mCherry (red fluorescent) and HeLa-GFP (green fluorescent) cell lines across the thin hydrophobic borders during the first three days of co-culturing. Cells at concentration  $5 \cdot 10^4$  cells/cm<sup>2</sup> in  $15 \mu\text{l}$  culture medium were seeded into two adjacent  $3 \times 10$  mm rectangular HEMA-EDMA domains separated by  $100 \mu\text{m}$ -thin PFPMA hydrophobic gap. The cells were cultured during 18 h in individual droplets with following immersion in conjoint culture medium and co-culture for additional 72 h. Generally, a drop placed into

rectangular hydrophilic areas has half-cylindrical shape (Fig. 3.5 C), by this reason the initial cell density has a gradual decrease from the center-line of the rectangular domain to its edges. During co-culture, cells were placed into a conjoint medium and the spatial restriction for cell migration did not exist anymore. However, cells were occupying the area close to the boundary of a hydrophilic domain due to the high cell density and lack of space in the middle region (Fig. 4.4).

Based on the obtained speed and translocation rate of cells motility, cells should cross 100  $\mu\text{m}$ -wide area within 11-25 h after placing in the conjoint medium. However, Levkin and co-authors showed that the cell adhesion can be prevented or significantly retarded on PFPMA hydrophobic domains in comparison with HEMA-EDMA hydrophilic substrate [158, 196, 235], which could be associated with protein repellency or resistance of hydrophobic domains [212, 236]. Fig. 4.4 shows fluorescent microscope images of co-cultured cells and corresponding cross-contamination plots. The plots indicate fluorescent intensity from cells vs. distance over the two compartments. The results showed that approximately 0,6% of MLTy-mCherry and less than 0,1% of HeLa-GFP cells were able to migrate across the border after 48h of culturing. Even after 72h of co-culturing the cross-contamination rate for both cell lines was not exceeding 1,5%. These results confirm the ability of the thin hydrophobic barriers to prevent cell migration and show that developed liquid patterning procedure can be used to precisely position and cultivate different cell groups in separated but adjacent compartments without intermingling. In the performed cell cross-contamination experiments cell seeding density was chosen to obtain 70-80% cell confluence inside the pattern after overnight cultivation in separated droplets. Despite the high initial cell density, the cell cross-contamination between the neighboring reservoirs after 72 h was still less 1,5%. This value is not critical for many biological applications. However, for experiments requiring four or more days, the initial cell density should be reduced to avoid the cell overgrowth.

#### 4.5 Mimicking Wnt-signaling system *in vitro*

By using the hydrophilic/hydrophobic micropatterns, in collaboration with PhD-student Eliana Stanganello and Dr. Steffen Scholpp (ITG, KIT) it was possible to culture Wnt-morphogen expressing zebrafish fibroblast Pac2 cells adjacent to but without direct cell contact with cells expressing a TOPFLASH-based Wnt reporter system (Fig. 4.5 A). To visualize the Wnt protein propagation we used a fluorescently-tagged and bioactive Wnt ligand Wnt8-GFP [237]. To observe the effective signaling of Wnt8-GFP and Wnt-

triggered expression of a transcriptional factor Tcf we transfected cells in the adjacent compartment with a TOPFLASH-mCherry based Wnt reporter system [238]. We found that the fibroblast cell line showed a basic activation of the TOPFLASH reporter on the micropatterned surface (Fig. 4.4 B).

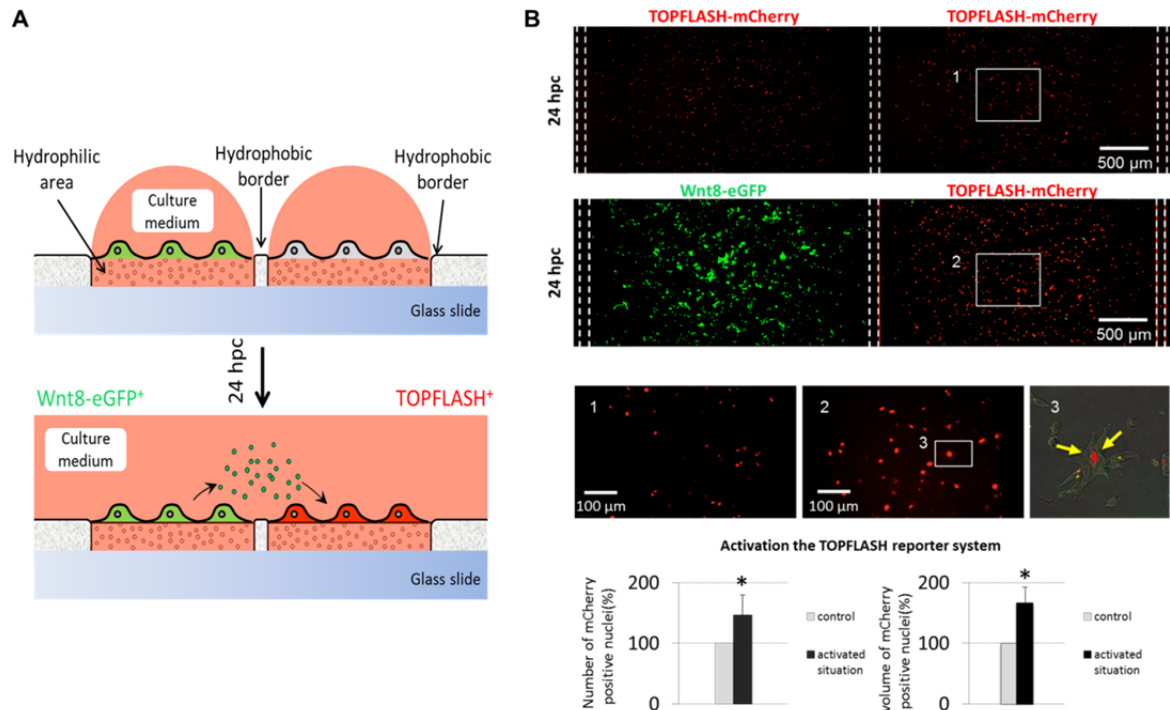


**Fig. 4.5.** Simulation of paracrine signaling system *in vitro*. (A) Schematics showing the setup of the intracellular experiment. One cells population (green) expresses the signaling molecules Wnt8, which influence the transcriptome of cells in adjacent compartment after connection (red). (B) Zebrafish Pac2 fibroblasts were transfected with TOPFLASH reporter and show a basic activation after 24hpc (inset 1 shows high magnification picture). If Wnt8-GFP positive cells are connected to the reporter compartment, we observe a significant increase of reporter expression (inset 2) and simultaneously internalization of Wnt8-GFP aggregates (inset 3, arrows). Graphs show significant increase of stimulated cells and an increase in fluorescence signal after normalization to the cell number.

The reporter activity increased up to 66% compared to the non-connected compartments after 24 hpc (Fig. 4.5 C, n=4). Besides, an accumulation of Wnt8-GFP, in most likely endosomes, within the receiving cells was determined (Fig. 4.5 B, inset 3, arrows). According to results the increase in reporter fluorescence was due to a combination of an increase in the proliferation rate as well as an increase in the activation

of the reporter gene. From these results we suggest that Wnt8 can propagate without cell-cell contact.

## **4.6 Conclusions**

A convenient method for creating complex patterns of multiple (up to tens) different cell types on the same substrate was introduced. The approach is based on a parallel formation of multiple cell-containing microreservoirs confined to the geometry of highly hydrophilic regions surrounded by superhydrophobic borders created inside the thin nanoporous polymer film by a surface grafting technique. Several advantages of the described method, over the existing techniques for cell patterning, include its compatibility with conventional culturing protocols, the patterning is a simultaneous process, i.e. it does not require alternate surface coating and multiple cell seeding steps. The culturing is performed inside a standard incubator for cell cultivation. In addition, cell-containing reservoirs are easily accessible from the outside for performing any kind of cell treatment, such as transfection, washing, or staining operations. These advantages make the developed technique a valuable tool for creating complex cell patterns using conventional means available in any cell biological laboratory. We believe that the developed method will find numerous applications for cell patterning, tissue engineering, studying cell-cell communication and signaling processes.

# Chapter 5

## Digital Liquid Patterning: A Versatile Method for Maskless Generation of Liquid Patterns and Gradients

### 5.1 Summary

Methods for surface patterning are extremely important in a lot of different areas, ranging from microelectronics industry, microfluidics to drug screenings and tissue engineering. The majority of technologies for generation of surface patterns rely on using masks or printing of substances on a surface. There are very few really maskless technologies for creating surface patterns. Here we present the digital liquid patterning method – a novel simple maskless method that allows for the on-demand fabrication of complex patterns of aqueous solutions without the need for changing the substrate or using different photomasks, stamps or stencils. Using this method, liquid and surface patterns with different customized geometries can be created manually by simple pipetting using the same pre-arrayed hydrophilic-hydrophobic substrates. We show applications of this maskless method to create patterns of particles, cells, hydrogels, and complex liquid gradients compatible with cell studies. The technical aspects of the synthesis are accessible to virtually any researcher and may help to simplify the production of variety of chemical, hydrogel, microparticle or cell patterns as well as their gradients.

### 5.2 Introduction

Surface patterning is crucial in a variety of different research and industrial fields such as the microelectronics industry, drug screening, biosensors, and cell biology [3, 207, 239-241]. There are two types of surface patterning methods: mask- and maskless methods. The methods relying on masks, such as photomasks for lithography [241, 242], silicone or metal masks for etching [195] and chemical vapor deposition [241, 242], plastic stencils [210, 219], cutouts [176, 243, 244], or PDMS-stamps [3, 245], require a new mask every time the pattern has to be changed. Maskless methods include printing [246-248], dip-pen nanolithography [249-251], optoelectrowetting [252], laser patterning [253], two-photon lithography [254], dynamic stencils lithography [255], electron beam lithography

[256-258], or projection lithography[259]. The maskless methods have clear advantages, because surface patterns with different geometries can be prepared on-demand without the need for new masks, thereby making experiments and optimizations faster, more convenient, and more affordable. There are only few maskless methods that use complex techniques such as pyroelectrodynamics shooting [260] for creating nano-pico volume liquid patterns of defined geometries; or dispensing a polymeric aqueous two-phase solution in the nanoliter volume regime [261]. Thus, the simple maskless technique for liquid patterning would be very important for making on-demand patterns of live cells for tissue engineering or studying cell-cell communication [196], patterns of nano or micro particles [243, 244], or for creating concentration gradients in surface tension-confined fluidic channels [176, 244].

### 5.3 Experimental Details

The idea of *digital liquid patterning* is similar to the working principal of a computer screen or a digital scoreboard. A digital scoreboard contains an array of bulbs (digits) that can be turned on in a particular pattern to generate the desired symbol. The same scoreboard can show different symbols (Fig. 5.1A). Here we use the same principle for generating different liquid patterns using an array of hydrophilic spots (digits) that can be filled with aqueous solutions to form a desired liquid pattern (Fig. 5.1 B). There are two ways to use such arrays. The hydrophilic spots can be filled individually to form various digital patterns of separated liquids pads similar to that generated on a scoreboard (Fig. 5.1 A). The other way is generation of a continuous liquid pattern over several hydrophilic spots (Fig. 5.1 B, C). In this case, neighboring pads are coalesced by a pipette tip over the hydrophobic border to produce a continuous liquid pattern or channel of desired geometry.

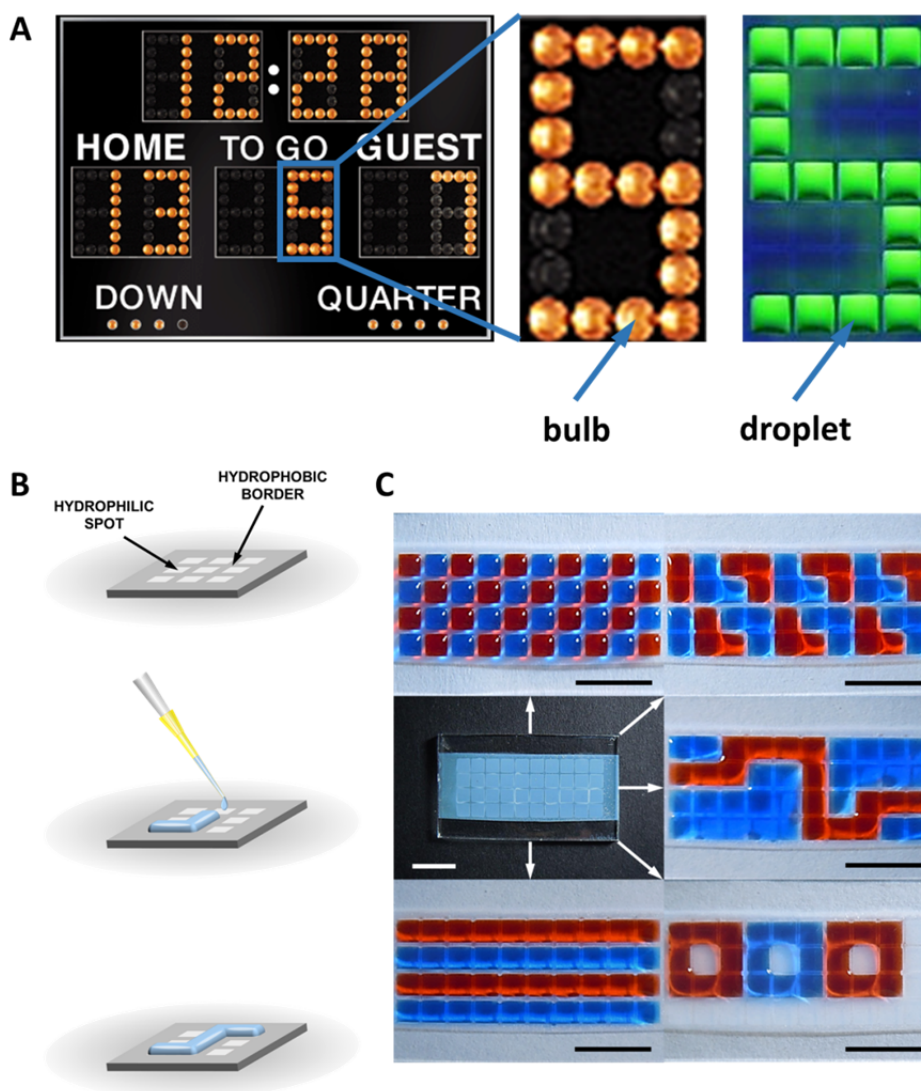


**Fig. 5.1.** Digital liquid patterning. (A) Working principle similarity: a light pattern generated by bulbs on a digital scoreboard and a liquid pattern generated by droplets on an array of hydrophilic spots. Each fluorescent liquid digit is  $3 \times 3$  mm separated by  $500 \mu\text{m}$  hydrophobic barriers. (B) The liquid pattern is generated on an array of hydrophilic spots by consecutive pipetting of droplets into the spots followed by their coalescence to form a continuous liquid pattern. (C) Different water patterns produced using the same template. Scale bar is 1 cm.

Our composite surface has been manufactured by a photolithographic technique described in Section X, Page Y [196]. An array of hydrophilic 3 mm HEMA-EDMA squares separated by  $500 \mu\text{m}$  hydrophobic borders was prepared (Fig. 5.1 A, C). The dimensions of hydrophilic squares and hydrophobic borders can be easily scaled down to  $335 \mu\text{m}$  and  $60 \mu\text{m}$  correspondingly [158, 196]. The static  $\theta_{\text{st}}$ , advancing  $\theta_{\text{adv}}$ , and receding

$\theta_{\text{rec}}$  water contact angles (WCA) of the unmodified porous HEMA-EDMA are  $17.4 \pm 0.5^\circ$ ,  $24.1 \pm 0.2^\circ$ , and  $3.8 \pm 0.1^\circ$ , respectively. The advancing WCA  $\theta_{\text{adv}}$  on the PFPMA barriers is  $128.3 \pm 2.1^\circ$ . The change of advancing WCA was associated with the decreased of UV-light intensity from  $12 \text{ mW/cm}^2$  to  $8 \text{ mW/cm}^2$ . Due to the high difference in hydrophobic properties, the highly hydrophobic barriers confine water to the geometry of the hydrophilic regions. However, in order to create complex liquid patterns of arbitrary shape on an array of hydrophilic spots, water solution should cover hydrophobic regions between individual hydrophilic spots. Therefore, there is a limit for the hydrophobicity of the barriers. If such barriers become superhydrophobic, a phenomenon of discontinuous dewetting can lead to the spontaneous separation of water droplets covering superhydrophobic regions into separated droplets, occupying individual hydrophilic spots [235, 262-265]. In order to visualize this effect, an array of hydrophilic spots separated by superhydrophobic barriers was prepared by roughening the polymer surface through the application of an adhesive tape as described previously [158, 235]. The enhanced roughness increases the advancing water contact angle of the barrier from  $128^\circ$  to  $167^\circ$ . Fig. 5.2 A shows the effect of discontinuous dewetting, which impedes the application of such arrays for digital liquid patterning (Fig. 5.2 B). Thus, the barriers should be hydrophobic in order to prevent spreading of the aqueous solution, but not superhydrophobic to ensure stability of the generated liquid patterns.



**Fig. 5.2.** A. Withdrawing of the water droplet from two coalesced  $3 \times 3 \text{ mm}$  hydrophilic spots separated by  $500 \mu\text{m}$  superhydrophobic barrier ( $\theta_{\text{adv}} = 167^\circ$ ). B. Withdrawing of the water droplets from two coalesced  $3 \times 3 \text{ mm}$  hydrophilic spots separated by  $500 \mu\text{m}$  highly hydrophobic barrier ( $\theta_{\text{adv}} = 128^\circ$ ).

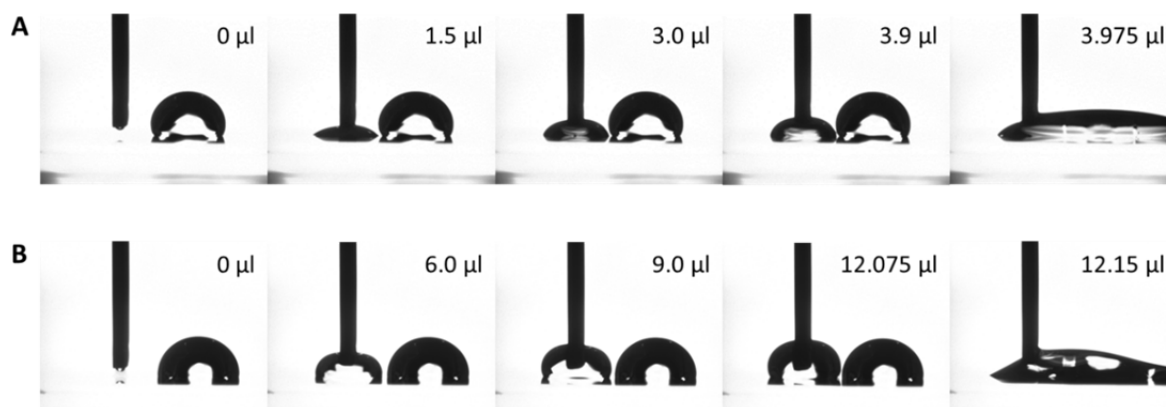


**Fig. 5.3.** Dispensing of water to hydrophilic spot next to another one filled with 15  $\mu\text{l}$  of water. A. The hydrophilic spots are separated by a 100  $\mu\text{m}$  hydrophobic barrier. The coalescence happened at the 3.9  $\mu\text{l}$  volume of the dispensing droplet. B. The hydrophilic spots are separated by a 500  $\mu\text{m}$  hydrophobic barrier. The coalescence happened at the  $\sim 12.1$   $\mu\text{l}$  volume of the dispensing droplet.

It is worth noting that the size of hydrophobic barriers has an influence on the maximal volume of two adjacent droplets because of their possible coalescence upon contact. We compared the maximal volume that could be dispensed into a hydrophilic spot separated by either 100  $\mu\text{m}$  or 500  $\mu\text{m}$  hydrophobic barrier next to another spot filled with 15  $\mu\text{l}$  of water. Thus, although only 3,9  $\mu\text{l}$  could be dispensed into the hydrophilic spot surrounded by a 100  $\mu\text{m}$  barrier (Fig. 5.3 A), the 500  $\mu\text{m}$  hydrophobic gap allowed for dispensing 12.1  $\mu\text{l}$  of water without merging (Fig. 5.3 B). The width of a hydrophobic gap however does not necessarily influence the maximum volume that can be enclosed inside a single hydrophilic spot. The maximum volume in this case is defined by the advancing water contact angle of the hydrophobic gap. Thus, the apparent water contact angle ( $\theta_{\text{app}}$ ) of a droplet formed in a hydrophilic spot increases upon adding more water to this droplet however does not cross the hydrophobic barrier until the  $\theta_{\text{app}}$  becomes equal to  $\theta_{\text{adv}}$  (Fig 5.4 A,B). Although the barrier width is different, the advancing WCAs of 100  $\mu\text{m}$  and 500  $\mu\text{m}$ -wide barriers are virtually identical.

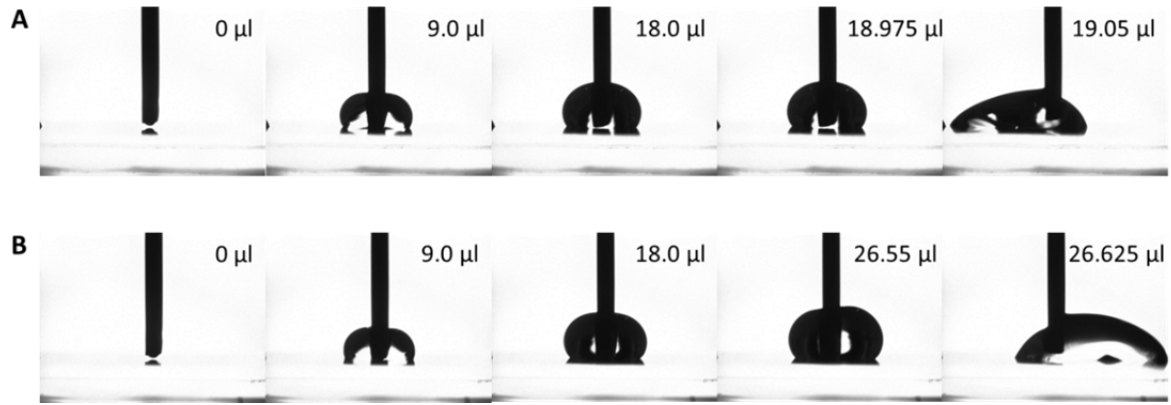


**Fig. 5.4.** A. Dispensing of water to a hydrophilic spot surrounded by a 100  $\mu\text{m}$  hydrophobic barrier. Advancing WCA of the barrier:  $130,9^{\circ} \pm 1,0^{\circ}$ . B. Dispensing of water to a hydrophilic spot surrounded by a 500  $\mu\text{m}$  hydrophobic barrier. Advancing WCA of the barrier:  $128,3^{\circ} \pm 2,1^{\circ}$ .

One of the limitations of the developed digital liquid patterning method is the evaporation of the liquid from a generated liquid pattern. The following section contains both practical and theoretical analysis of the rate of evaporation of liquid droplets formed on hydrophilic patterns of certain geometry. The evaporation of a droplet in still air is slow under the normal conditions in that it can be ascribed a quasi-equilibrium process defined by Fick's law:

$$Q = -DS_d \frac{dC}{dr} \quad (11)$$

where  $Q$  is the net diffusive flux of the molecules of liquid away from the gas-liquid interfaces [kg/sec],  $D$  is the diffusion coefficient of liquid in gas (air) [ $\text{m}^2/\text{sec}$ ],  $S_d$  is the surface area of the droplet [ $\text{m}^2$ ],  $C$  is the vapor concentration [ $\text{kg}/\text{m}^3$ ], and  $r$  is the radial distance [m] (Fig. 5.5). When a liquid is placed on a solid surface, the adjacent air becomes saturated with the vapor due to the exchange of the molecules between the liquid and its vapor [266]. We assume, that at the small distance apart of the droplet, the vapor of the droplet at equilibrium concentration is the same as the saturated vapor ( $C_s$ ) [ $\text{kg}/\text{m}^3$ ] at the same temperature. At the infinite distance from the liquid interface the vapor concentration is equal to the ambient vapor concentration ( $C_a$ ), which is determined by relative humidity. Thus, the following boundary conditions exist [267]:

$$\begin{cases} C = C_s & \text{when } r = R_d \\ C = C_a & \text{when } r = \infty \end{cases} \quad (12)$$

where  $R_d$  is the radius of the droplet (Fig. 5.5). Therefore, from equation (1), the droplet volume change with time can be obtained by [268-270]:

$$Q = -\rho \frac{dV}{dt} = 4\pi D R_s (C_s - C_a) f(\theta) \quad (13)$$

where  $\rho$  is the liquid density [ $\text{kg/m}^3$ ],  $V$  is the droplet volume [ $\text{m}^3$ ],  $t$  is time [sec], and  $R_s$  is spherical radius [m] (Fig. 5.5).  $f(\theta)$  is the contact angle function, which describes the dependency of the evaporation rate on the contact angle.

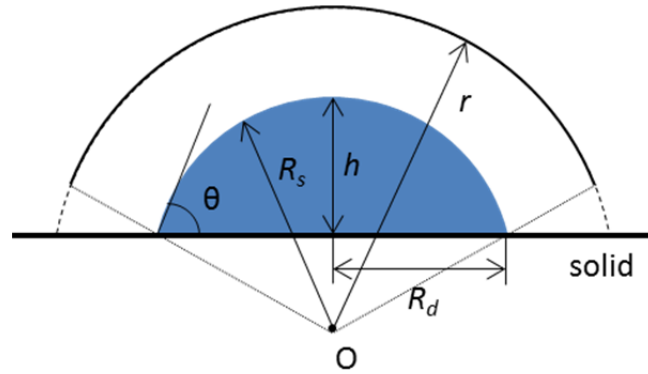


**Fig. 5.5.** Schematics illustration of sessile droplet and its geometrical parameters.

The  $f(\theta)$  - function is an important parameter to describe the temporal evolution of the droplet volume. There are several models proposing an empirical correlation of the droplet volume and evaporation rate. Rowan et. al. [266] assumed that the vapor molecules escape from a curved surface only in the radial direction of the vapor concentration gradient ( $dC/dr$ ), and is equal to  $(C_s - C_a)/R_s$ . Therefore, the effective diffusion area can be described by the solid arc of the radius  $r$  (Fig. 5.5), thus  $S_d = 2\pi r^2(1 - \cos\theta)$ . Noteworthy, the *Rowan model* is correct when the evaporation occurs from a completely unsupported and spherical cap-shaped droplet. By this reason, the vapor flux occurring at the edge of spherical cap-shaped droplet was neglected, and the following  $f(\theta)$ -function was proposed [266]:

$$f(\theta)_R = \frac{1 - \cos(\theta)}{2} \quad (14)$$

Bourges-Monnier and Shanahan [271] also assumed that the evaporation of liquid vapor is radial, but the effective diffusion of molecules into the environment occurs in the entire area of the droplet, including the dashed arcs in Fig. 5.5. Correspondingly, the effective diffusion area was described as  $S_d = 2\pi r^2 \left(1 - R_s \cos\theta / r\right)$ . Considering a spherical cap-shape of surface area (defined by a coordinate system based on the center of the droplet, through which the vapor diffuses) the obtained  $f(\theta)$ -function, in this case, is self-consistent for the concentration gradient ( $dC/dr$ ). *Bourges-Monnier-Shanahan model* proposes the following contact angle function:

$$f(\theta)_{BM\&S} = -\frac{\cos(\theta)}{2\ln(1-\cos(\theta))} \quad (15)$$

The *Bourges-Monnier-Shanahan* model includes the diffusive flux at the edges of spherical cap-shaped droplet and the calculated evaporation rate becomes greater in comparison with the model proposed by Rowan. However, the increase of the radial distance leads to an increase of the subtending angle of spherical cap-shape (Fig. 5.5). This implies that the molecules of vapor are redistributed in the circumferential direction, which is in contradiction with the assumption of a pure radial concentration gradient [272]. In any event, the Bourges-Monnier-Shanahan model leads to the maximal evaporation rate when the droplet surface is a part of a spherical surface [271]. So, the major difference between the *Rowan* and *Bourges-Monnier-Shanahan models* is the treatment of evaporation behavior around the droplet edge. Although the edge effect may be small in comparison with the bulk evaporation rate, ignoring the (*Rowan model*) or overestimating (*Bourges-Monnier-Shanahan models*) such an effect leads to cumulative errors, which can be a reason a severe discrepancy between the theory and the experiment [268-270, 272].

Picknett and Bexton [273] developed a theory to predict evaporation at any time of droplet lifespan, as well based on the spherical cap geometry. However, the *Picknett-Bexton model* implies the conversion of the effective diffusion problem of determining the evaporation rate to a problem of evaluating the capacitance of an isolated conductive body of the same size and shape of the droplet described as an equiconvex lens [269, 270, 272, 273]. Their solution is given by the following equation:

$$f(\theta)_{P\&B} = \frac{1}{2} \frac{\bar{c}}{R_s} \quad (16)$$

where  $\bar{c}$  is the capacitance of the equiconvex lens, which can be described by polynomial functions:

For  $0 \leq \theta \leq 0,175 \text{ rad}$  ( $0^\circ \leq \theta \leq 10^\circ$ ),

$$\frac{\bar{c}}{R_s} = 0,6366 \theta + 0,09591 \theta^2 - 0,06144 \theta^3 \quad (17)$$

and for  $0,175 \leq \theta \leq \pi \text{ rad}$  ( $10^\circ \leq \theta \leq 180^\circ$ ),

$$\frac{\bar{c}}{R_s} = 0,00008957 + 0,6333 \theta + 0,116 \theta^2 - 0,08878 \theta^3 + 0,01033 \theta^4 \quad (18)$$

The *Picknett-Bexton model* gives a more accurate description of the steady-state diffusion equation ( $\nabla^2 c = 0$ ) in comparison with the *Rowan* and *Bourges-Monniner-Shanahan models* [272]. However, all these models were derived from the assumption that a substrate has an ideal flat and non-rough surface and have limitations in explaining the differences in the evaporation rates of liquids on various substrates [268, 269, 272]. Generally, the evaporation of a droplet is influenced by the liquid (e.g. surface tension, viscosity, and volatility), surrounding gas (e.g. relative humidity, temperature and pressure), and substrate (e.g. surface charge, wettability, and roughness) [267, 268, 274, 275]. For instant, *Song et. al.* [272] tested the evaporation of a water droplet on ten different surfaces and reported that the evaporation rate depended on the contact angle of liquid. In addition, it was shown that the evaporation rates varied and depended on the surface material, even for surfaces possessing the same contact angle. *Birdi et. al.* [267] showed that the electrostatic interactions in the liquid-solid interface influence on the contact angle and contact area between the liquid and substrate thereby affecting the evaporation rate. Therefore, it was necessary to perform droplet evaporation experiments in order to find the contact angle function for a HEMA-EDMA patterned substrate and predict the rate and time of evaporation of aqueous solutions from a generated liquid pattern.

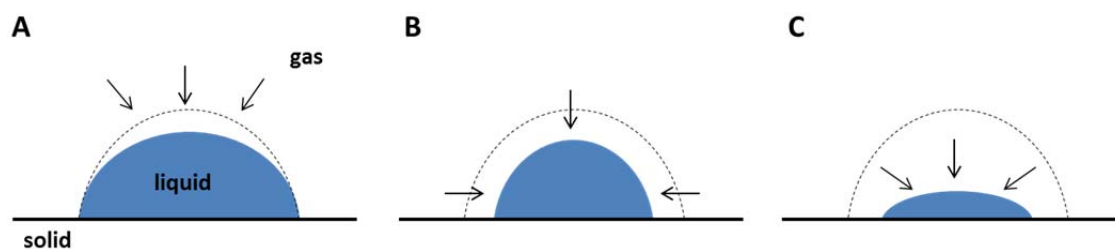


**Fig. 5.6.** Models of conformational changes of evaporating droplet: (A) constant contact radius model; (B) constant contact angle model; (C) shrinkage model.

Once a liquid droplet starts to evaporate, its shape undergoes changes. The changes of the droplet shape can be described using three distinct models [273]: *constant contact radius model* (CCRM), *constant contact angle model* (CCAM), and the *shrinkage model* (SM). In the CCRM model the contact area radius remains the same during the evaporation of the liquid, while the contact angle of the evaporating droplet decreases (Fig. 5.6 A). In the CCAM model, the contact area radius decreases, while the contact angle of the evaporating droplet remains constant (Fig. 5.6 B). In the SM model, both the contact area and contact angle of the evaporating droplet decrease simultaneously (Fig. 5.6 C). Fig. 5.7 shows the change in shape during the evaporation of water droplets placed in hydrophilic patterns of different geometry. In these experiments, the ratio of initial droplet volume per surface area was kept at  $0,5 \mu\text{l}/\text{mm}^2$ . CCRM was clearly observed. Therefore, the contact area radius of a droplet during evaporation was constant, thus based on equations (11) and (12) the evaporation rate and time can be predicted, if the contact angle function is known.

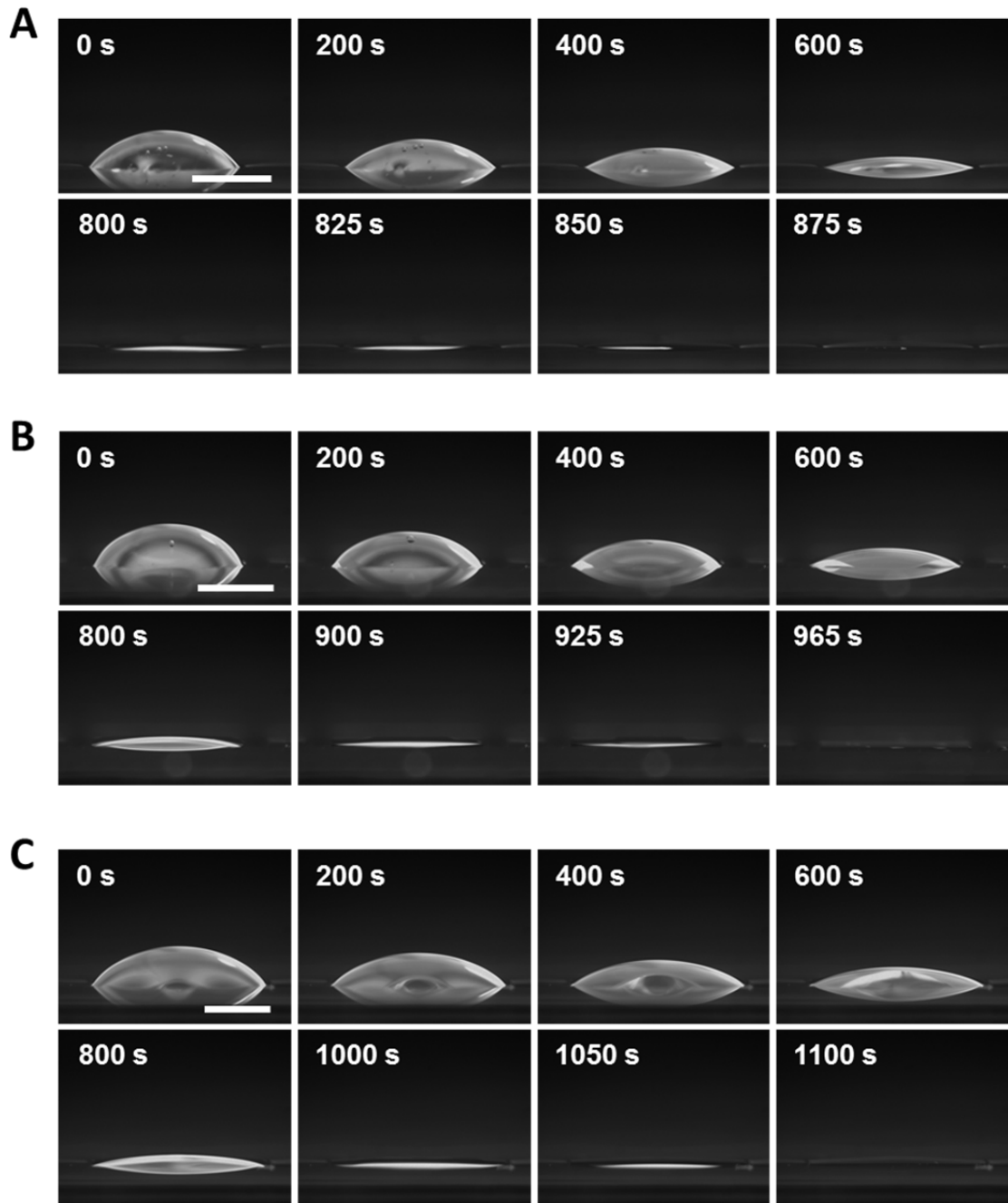


**Fig. 5.7.** Shape of evaporating droplets placed on hydrophilic spots with different geometries as a function of time. Spots geometries: (A) circular (3 mm diameter), (B) square (3 mm side length), and (C) hexagonal (2 mm side length) hydrophilic spots. All spots are surrounded by 100  $\mu\text{m}$  hydrophobic borders. The ratio of water volume per surface area is  $0,5 \mu\text{l}/\text{mm}^2$ . Scale bar is 1,5 mm.

To obtain the contact angle function of the evaporating droplet from a circular pattern (3 mm in diameter) the values of the  $f(\theta)$ -function were calculated using equation (19) derived from equation (13) based on the experimental data at distinct time step:

$$f(\theta) = \frac{V_{i+1} - V_i}{-\left[\frac{4\pi D R_{s,i} (C_s - C_a)}{\rho}\right] \Delta t} \quad (18)$$

where  $\Delta t$  is a time step [sec],  $V_{i+1}$  and  $V_i$  are droplet volumes [ $\text{m}^3$ ], and the subscript  $i$  refers to the value of the parameter at each time step. All experiments were performed at 23 °C and 13-15% relative humidity. The concentration of vapor at the semi-sphere surface [ $\text{kg}/\text{m}^3$ ],  $C_s$ , was calculated by assuming the ideal gas behavior of the water vapor  $C_s = P_v M / \bar{R} T = 0,0204 \text{ kg}/\text{m}^3$ , and the ambient vapor concentration,  $C_a$ , is  $0,0031 \text{ kg}/\text{m}^3$ . The density of water,  $\rho$ , is  $1000 \text{ kg}/\text{m}^3$ . The diffusion coefficient of water molecules in air,  $D$ , is  $2,47 \cdot 10^{-5} \text{ m}^2/\text{s}$  [276]. I assume that a spherical cap-shaped droplet can be characterized by the contact diameter, droplet height, contact angle, and spherical radius. Once two of these parameters are known, the other parameters can be derived [268, 269, 272]. Thus, the spherical radius ( $R_{s,i}$ ) and volume ( $V_i$ ) of evaporating water droplet can be calculated using the following equations:

$$R_{s,i} = \frac{H}{1 - \cos \theta_i} \quad (20)$$

$$V_i = \frac{\pi}{3} R_{s,i}^3 (1 - \cos \theta_i)^2 (2 + \cos \theta_i) \quad (21)$$

where  $h$  is the height of the droplet [m] (Fig. 5.5). At the given ratio of droplet volume per surface area ( $50 \text{ } \mu\text{l}/\text{cm}^2$ ), the droplet volume initially placed in round-shape hydrophilic pattern was  $3,53 \text{ } \mu\text{l}$ . The height,  $H$ , and contact angle of the evaporating droplet,  $\theta$ , were obtained from the captured images. The time-dependent contact angle and volume of the evaporating droplet from a circular pattern are shown in Fig. 5.8 A, B. The values of contact angle ( $\theta_i$ ) and droplet volume ( $V_i$ ) in the graphs were normalized to the initial values of contact angle ( $\theta_0$ ) and droplet volume ( $V_0$ ). The linear decrease of volume and contact angle of the evaporation time implies to approximately linear dependence of the  $f(\theta)$ -function on  $\theta$ :

$$f(\theta) = a \cdot \theta + b \quad (22)$$

where  $a$  and  $b$  are empirical constants inherent to the substrate, which can be determined in conjunction with the evaporation rate.

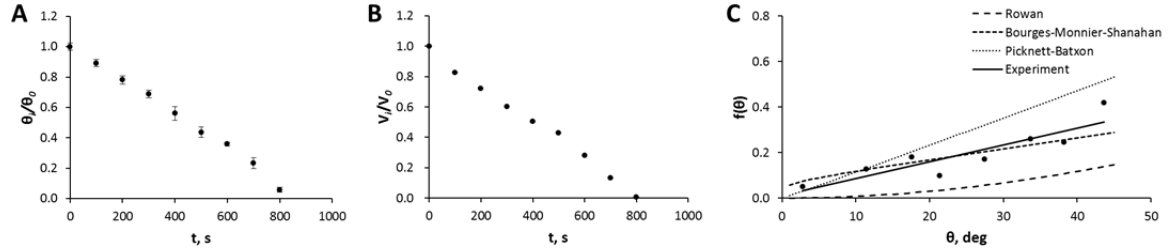


**Fig. 5.8.** (A) Time-dependent normalized contact angle. (B) Time-dependent normalized droplet volume. (C) Dependence of contact angle function on contact angle of the evaporating water droplet.

Using the measured droplet height and contact angle values, the dependence of the contact angle function on the contact angle of the evaporating droplet was determined. Fig. 5.8 C shows the calculated value of  $f(\theta)$ -function and compares the theoretical predictions of the temporal changes of the contact angle function with the experimental results. Based on the plotted results, a linear  $f(\theta)$ -function is proposed:

$$f(\theta) = 0,074 \cdot \theta + 0,00125 \quad (23)$$

Derived from equation (3), the time of evaporation rate can be calculated by the formula:

$$\Delta t = \frac{V_{i+1} - V_i}{-\left[\frac{4\pi DR_{s,i}(C_s - C_a)}{\rho}\right] f(\theta)} \quad (24)$$

Since the volume change ( $dV/dt$ ) is linearly proportional to the spherical radius of droplet ( $R_s$ ) rather than to the surface area ( $S_d$ ), the rate and time of droplet evaporation for the square (3 mm side length) and hexagonal (2 mm side length) spots were also estimated by using the obtained contact angle function, equation (23). Fig. 5.8 B,C show the shape changes of the water droplets, evaporating from the square and hexagonal spots. Utilizing the equations (13), (20-23), and (24) the time and rate of droplet evaporation from circular, square, and hexagonal spots were calculated (Table 5.1, 5.2). The discrepancy of the

theoretically estimated time and rate of evaporation is described as deviations from the experimental values (see also Table 2.1). The *Rowan* and *Bourges-Monniner-Shanahan models* overestimate the values of the evaporation time by 70-100% and 12-40%, respectively. Since the evaporation rate is inversely proportional to the evaporation time, the values of the evaporation rate predicted by these two models were underestimated by 47-49% in case of the *Rowan model*, and 10-29% in case of the *Bourges-Monniner-Shanahan model*. The discrepancy of values obtained by using the *Picknett-Baxton model* gave an underestimation of the evaporation time by 37-44% and overestimated the evaporation rate by 40-70%.

As seen in Table 5.1, 5.2 and in Fig. 5.8 C, the best fit of the experimental evaporation time and rate can be achieved when the contact angle function expressed by equation (23) is applied. In this case, the discrepancy of the estimated values with the experimentally obtained results did not exceed 9% for both the evaporation rate and time. This small discrepancy with the experimental data can be ascribed to the variations of ambient temperature and relative humidity of air. All previous correlations under-predicted the experimental data, which implies that the previous droplet evaporation correlations may have limitations in predicting the droplet volume change and evaporation rate and time for water droplets sessile on a hydrophilic/hydrophobic pattern. The proposed contact angle function, equation (23), correlates well with the experimental data within an error only 4-9%. Thus, the suggested empirical model satisfactorily describes the process of evaporation of a water droplet from the micro-patterned substrate and can be applied for estimating the evaporation rate and time of micro-droplets from hydrophilic spots of different geometries.

**Table 5.1.** Comparison of the experimental time of droplet evaporation with the results estimated by using theoretical approximations of the contact angle function.

Geometry	<i>Efremov</i>		<i>Rowan</i>		<i>Bourges-Monniner-Shanahan</i>		<i>Picknett-Baxton</i>	
	$t_E$ , sec	deviation, %	$t_R$ , sec	deviation, %	$t_{BM-S}$ , sec	deviation, %	$t_{P-B}$ , sec	deviation, %
Circle	820	-6,3	1707	+95,1	976	+11,5	518	-40,8
Square	1045	+8,9	1811	+68,9	1342	+39,8	685	-44,2
Hexagon	1060	-4,1	2105	+98,6	1276	+20,4	671	-36,7

**Table 5.2.** Comparison of the rate of droplet evaporation obtained experimentally with results estimated by using theoretical approximations of the contact angle function.

Geometry	<i>Efremov</i>		<i>Rowan</i>		<i>Bourges-Monniner-Shanahan</i>		<i>Picknett-Baxton</i>	
	$Q_E$ , $10^3 \cdot \text{mg/sec}$	deviation, %	$Q_R$ , $10^3 \cdot \text{mg/sec}$	deviation, %	$Q_{BM-S}$ , $10^3 \cdot \text{mg/sec}$	deviation, %	$Q_{P-B}$ , $10^3 \cdot \text{mg/sec}$	deviation, %
Circle	4,31	+7,0	2,07	-48,6	3,62	-10,2	6,81	+69,0
Square	4,31	-8,8	2,48	-47,1	3,35	-28,6	6,57	+40,1
Hexagon	4,91	+4,5	2,47	-47,6	4,07	-13,6	7,75	+64,5

## 5.4 Results and Discussion

The patterning of cells and particles has attracted attention in the past decade [176, 207, 243, 244] and is often required for screening of drugs or biomolecules [277] as well as for studying cell signaling processes [196] and tissue engineering [209]. Such experiments require fabrication of multiple patterns with different geometries in order to optimize and test different conditions. Printing techniques are usually not compatible with the deposition of microparticles or cells. The method of *digital liquid patterning* presented here offers a convenient way to position particles or cells on a surface in defined and customized two-dimensional patterns without any need to design a new photomask every time the geometry has to be changed. Fig. 5.9 shows three examples of applications of the *digital liquid patterning* technique using hydrophilic arrayed substrates with exactly the same geometry. The first example presents the formation of a 2D pattern of 45-70  $\mu\text{m}$  silica microparticles by pipetting a suspension of the particles to form a desired pattern (Fig. 5.9 A). In the same manner, patterns of green fluorescent HeLa-GFP cells were generated (Fig. 5.9 B). After the cells had settled and adhered to the surface inside individual reservoirs and channels, they were placed in the same medium for further cultivation. The cell proliferation in the patterns was monitored for 4 days. The geometry of the cell pattern did not change even after 4 days of culturing due to the retardation of cell motility by the hydrophobic borders [196]. We suppose that the main reason for the minor spreading of the cells beyond the initial pattern area was the cell overgrowth inside the pattern after 4 days of culturing.

One challenge related to the use of complex liquid droplets for patterning applications is the instability of such droplets, which might lead to mixing or changing the initial distribution of patterned particles or cells caused by even slight movements of the liquid patterns. In order to stabilize such patterns, solution can be gelled after formation of a digital liquid pattern [243] to form a hydrogel pattern. Fig. 5.9 C shows an application of the maskless *digital liquid patterning* technique to create 2% agarose gel patterns dyed with a food color on the array of hydrophilic spots.

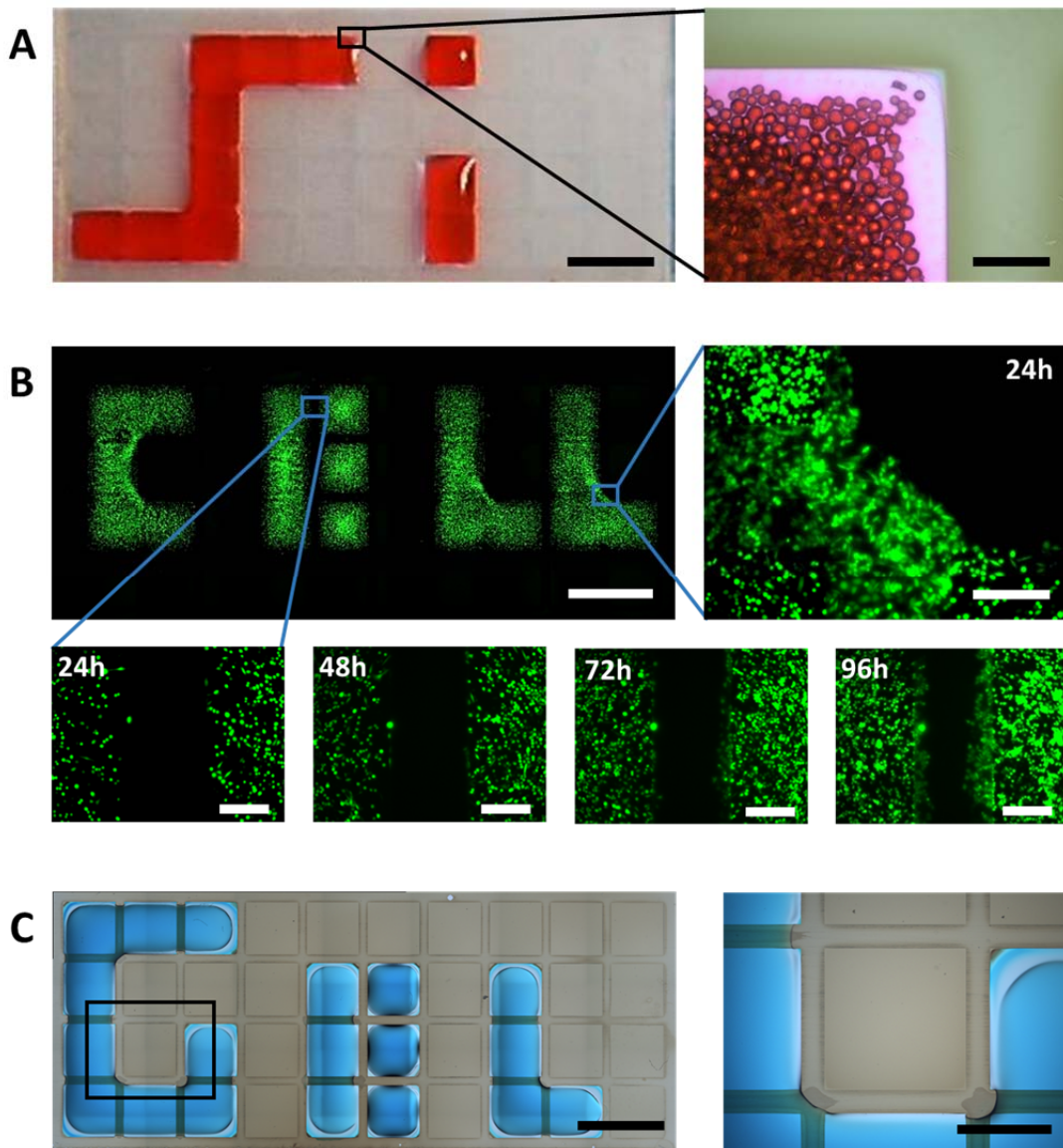


**Fig. 5.9.** Digital liquid patterning: examples of applications. (A) Optical microscope images of silica microparticles. Scale bars are 5 mm (left) and 300  $\mu\text{m}$  (right). (B) Fluorescence microscope images of HeLa cells stably expressing GFP 24h after patterning. Time lapse images of the enlarged region monitored during 96 h post immersion in the same medium. Scale bars are 5 mm (top left) and 300  $\mu\text{m}$  (bottom and right). (C) Hydrogel patterns. Scale bars are 5 mm (left) and 2 mm (right).

Methods for creating gradients of chemical and biochemical properties are important in materials science, biotechnology, and cell biology for rapidly screening physicochemical phenomena, mimicking cellular and tissue microenvironments, or simulating different physical stimuli and biochemical interactions [243, 244, 278, 279]. Here we show that exactly the same substrate can be used to generate single or

multi-gradients of chemicals inside surface tension-confined channels of arbitrary geometry using the *digital liquid patterning* method (Fig. 5.10).

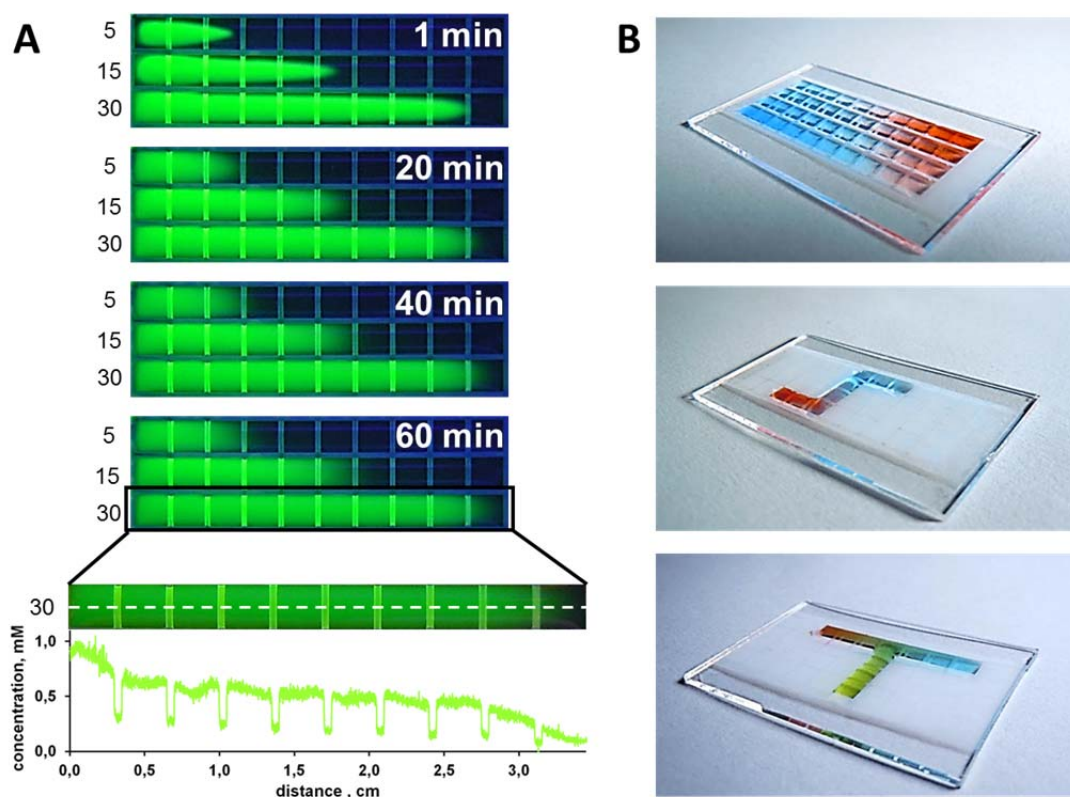


**Fig. 5.10.** Generation of single and multiple concentration gradients inside surface tension-confined liquid channels formed by the digital liquid patterning method. (A) Fluorescence images showing the distribution of fluorescein concentration along the open liquid channels as a function of the volumes (5, 15, or 30  $\mu\text{l}$ ) of 1 mM fluorescein solution injected into the channels. Graph showing the concentration of fluorescein in the channel along the white dashed line after equilibration of a 30  $\mu\text{l}$  fluorescein drop for 60 min (bottom). (B) Multi-gradients in open liquid channels of different geometries prepared using the same array of hydrophilic spots.

All gradients were realized by using the same arrays of 3 mm hydrophilic spots separated by 500  $\mu\text{m}$  hydrophobic barriers. Chemical gradients were generated by injecting 5, 15 or 30  $\mu\text{l}$  of 1 mM fluorescein isothiocyanate (FITC) solution at the end of an open liquid channel (3 mm width and 34.5 mm length) leading to the formation of linear gradients of 10, 20 and 34.5 mm, respectively, after equilibration for 60 min (Fig. 5.10 A). The quantification of the liquid gradients showed a gradual

decrease in the concentration of fluorescein along the channel from 1 mM to 0,1 mM.

The molecular spreading of soluble matter in an open liquid fluidic channel may occur by both advection and diffusion. Generally, in the axial direction the matter transport occurs by advection due to the hydrodynamic stretching along the channel axis, whereas in the perpendicular direction the transport is mainly due to molecular diffusion [280]. From literature it is known [281-283] that the dispersion, i.e. the combined process of advection and diffusion, within a channel with parabolic-shape cross-section with a width  $w$ , height  $h \ll w$  and length  $l \geq w$  can be described in terms of three regimes: a short time regime or *ballistic regime* when  $t \ll w^2/D$ , where  $D$  is molecular diffusion of soluble matter; an intermediate time regime when  $w^2/D \ll t \ll l^2/D$ ; a long time regime or *Taylor regime* when  $t \gg l^2/D$ . At the short time regime, molecular diffusion has no influence in dispersion, because molecules flow with the streamline of hydrodynamic current. The rate of gradient growth in this case is linear. At the intermediate regime, both advection and diffusion have role in propagation of matter along and aside of the channel. At the long time regime, molecular transfer occurs solely by diffusion and molecules distribution is homogeneous the entire channel cross-section. In this study, each liquid channel was composed of ten  $3 \times 3$  mm hydrophilic squares in length and one square in width. The adjacent hydrophilic squares were divided by 0,5 mm hydrophobic border. Thus, the channel had 34,5 mm in length and 3 mm in width. The volume of the channel was kept constant, 30  $\mu$ l in that the channel height is 0,74 mm. FITC diffusion coefficient was calculated using Wilke-Chang equation:

$$D = 7,4 \cdot 10^{-8} \frac{T \sqrt{\varphi_s M_s}}{\eta_s (\tilde{V})^{3/5}} \quad (25)$$

where  $T$  is temperature,  $\varphi_s$  is association factor of solvent with solute,  $M_s$  is molecular mass of solvent,  $\eta_s$  is viscosity of solvent, and  $\tilde{V}$  is molar volume of solute. Molar volume of solute is the volume of one mole of a substance at a given pressure and temperature. For water as a solvent under normal conditions:  $\eta_{H_2O} = 0,890 \cdot 10^{-3}$  Pa·s,  $\varphi_{H_2O} = 2,6$ ,  $M_{H_2O} = 18$  g/mol,  $T = 298$  K. The molecular volume of solute is equal to the molecular mass divided by mass density:  $\tilde{V}_{FITC} = 252,5$   $\text{cm}^3/\text{mol}$ . According to the equation (25)  $D_{FITC} = 6,4 \cdot 10^{-3}$   $\text{cm}^2/\text{s}$  in that  $w^2/D = 14$  sec and  $l^2/D = 31$  min. Thus, the dispersion of FITC molecules occurred mainly by

advection in the first seconds after a droplet entered the channel. Within the half an hour, the impact of advection was minimalized, and molecular transport occurred primary by diffusion (Fig. 5.10 A).

Our method allows for the rapid and facile formation of not only single linear gradients but also gradients of multiple components with non-linear channel geometries. Fig. 5.10 B shows multiple parallel gradients and gradients with non-straight channel geometries formed simply by injecting different solutions into opposite ends of the liquid channels of different geometries. In all examples, the food dyes formed reproducible and stable gradients independent of the channel geometry.

## 5.5 Conclusions

In conclusion, we presented the *digital liquid patterning* technique – a convenient, facile, maskless patterning method for the generation of liquid patterns of different geometries without using any additional masking or printing equipment. This method will be especially useful for biologists who want to create complex patterns of different or the same cell types, or chemical and cellular gradients without the need for complex microfluidic equipment and photomasks. The patterning is based on the manual formation of discrete or combined liquid droplets of user-defined geometry using a hydrophobic substrate arrayed with hydrophilic spots. The advantages of this method are that it does not require clean room or high-precision microfabrication and allows for a simple and manual formation of complex patterns of liquids, cells, particles using the same substrate. The drawback is that due to the manual formation the method is limited to relatively large hydrophilic “digits” reducing the resolution of the produced patterns. Downscaling of the spot size can result in a higher resolution of the produced patterns but is compromised by the possible need for an automated liquid dispenser. The downscaling of this method to create liquid patterns with higher resolution is currently in the development in our lab. In spite of the fact that not all complex geometry can be accessible because of the “digits” size, it does not affect the fidelity of produced patterns that lies in the micrometer range and depends on the “quality” of the hydrophilic-hydrophobic interface and the distance between hydrophilic spots.

We demonstrate that the *digital liquid patterning* method can be used to create micropatterns of aqueous solutions, microparticles, or hydrogels. The biocompatibility of the HEMA-EDMA porous polymer substrates used in this study [158, 196] allows for the biological applications of the method and patterning of live cells. The same substrates can be used to create patterns with different geometries. In addition, we show that the technique also allows for the generation of complex chemical gradients inside surface tension-confined liquid patterns. This method can be used for generation of gradients of particles, hydrogels, or living cells with different geometry without the need for using different photomasks.

# Chapter 6

## Conclusion and outlook

In this work, a new method for patterning of aqueous solutions and suspensions on porous polymer surfaces was described. The fabrication, characterization and implementation of precise micropatterned polymer surfaces were performed. Although variety of surface patterning technologies have been developed for specific applications, there are only few of those that allow liquid patterning. Thus, there is still a clear need for further development and elaboration of methods for generation of liquid surface patterns. The presented method is based on the fabrication of hydrophobic domains around hydrophilic areas on a porous polymer surface, making it possible to confine an aqueous solution in the hydrophilic region of an arbitrary geometry.

Droplets of aqueous solutions or suspensions with pre-defined geometries could be generated by dispensing an aqueous solution into hydrophilic HEMA-EDMA areas surrounded by hydrophobic PFPMA borders. Droplet geometry was limited only by the size of hydrophobic domains and the design of photomask.

It was also shown that up to twenty different cell types could be patterned and co-cultured with only 1,5% of the cross-contamination rate during 96 h of cultivation. In a collaboration with Eliana Stanganello and Dr. Steffen Scholpp (ITG, KIT), the developed patterning approach was used to investigate cell-cell communication. In this subproject, Wnt-morphogen propagation and following activation of Tcf-protein expression between two patterned zebrafish fibroblast Pac2 populations in cell-contact independent manner was for the first time demonstrated in an *in-vitro* system.

In addition, the further development of the method resulted in a new maskless method termed *digital liquid patterning*. The method is based on manufacturing of an array of hydrophilic HEMA-EDMA spots surrounded by hydrophobic PFPMA borders. Dispensing of a liquid into the individual hydrophilic spots with subsequent coalescence of

adjacent droplets leads to the formation of open liquid channels with arbitrary geometry. It was shown that width of hydrophobic borders and volume of individual droplets could affect the coalescence process. The implementation of an array of superhydrophilic HEMA-EDMA spots surrounded by superhydrophobic PFPMA borders could be a reason of spontaneous dewetting at certain droplet volume and instability of formed liquid channels that was not observed in case of the hydrophilic/hydrophobic micropatterned surfaces. The developed *digital liquid patterning* approach was applied to create arbitrary patterns of living cells, microparticles, hydrogels, and multicomponent chemical gradients of complex geometry.

In conclusion, a facile and convenient method for patterning of aqueous solutions and suspensions based on the porous polymers was successfully developed. This method can be implemented in many different industrial and research fields. The micropatterned surfaces can be used as an approach for revealing and testing cell-cell interactions in multi cell type systems *via* propagation of soluble signaling molecules or vesicles. In addition, the developed method can find applications to mimic and study different *in vivo* processes, such as earlier embryogenesis, cancerogenesis and cell differentiation. The *digital liquid patterning* offers simple and maskless approach for manual generation of micrometer precise liquid patterns without the need for manufacturing a new photomasks or changing substrate every time when geometry of liquid pattern has to be changed or modified. Therefore, this approach can reduce experimental time for the production of arbitrary liquid patterns of variety biomaterials and cells. *Digital liquid patterning* is also suitable for the generation of multi-component gradients with complex geometry of different materials compatible with biological studies. In addition, the method does not require special training or sophisticated equipment for generation liquid patterns or gradients, thus the technique is easy accessible to virtually any user. By reducing the size of hydrophilic spots and hydrophobic borders on an array, it can be anticipated that much smaller and complex patterns could be produced.

# Bibliography

1. Falconnet, D., et al., *Surface engineering approaches to micropattern surfaces for cell-based assays*. Biomaterials, 2006. **27**(16): p. 3044-3063.
2. Zhou, X.Z., et al., *Chemically Functionalized Surface Patterning*. Small, 2011. **7**(16): p. 2273-2289.
3. Kane, R.S., et al., *Patterning proteins and cells using soft lithography*. Biomaterials, 1999. **20**(23-24): p. 2363-2376.
4. Michel, R., et al., *Selective molecular assembly patterning: A new approach to micro- and nanochemical patterning of surfaces for biological applications*. Langmuir, 2002. **18**(8): p. 3281-3287.
5. Jang, K., et al., *Micropatterning of biomolecules on a glass substrate in fused silica microchannels by using photolabile linker-based surface activation*. Microchimica Acta, 2012. **179**(1-2): p. 49-55.
6. Hahn, M.S., et al., *Photolithographic patterning of polyethylene glycol hydrogels*. Biomaterials, 2006. **27**(12): p. 2519-2524.
7. Faia-Torres, A.B., et al., *Comprehensive biomaterials*. Choice: Current Reviews for Academic Libraries, 2012. **49**(8): p. 182-199.
8. Ross, A.M. and J. Lahann, *Surface engineering the cellular microenvironment via patterning and gradients*. Journal of Polymer Science Part B-Polymer Physics, 2013. **51**(10): p. 775-794.
9. Ito, T. and S. Okazaki, *Pushing the limits of lithography*. Nature, 2000. **406**(6799): p. 1027-1031.
10. Kinoshita, H., et al., *Soft-X-Ray Reduction Lithography Using Multilayer Mirrors*. Journal of Vacuum Science & Technology B, 1989. **7**(6): p. 1648-1651.
11. Bjorkholm, J.E., et al., *Reduction Imaging at 14 Nm Using Multilayer-Coated Optics - Printing of Features Smaller Than 0.1-Mu-M*. Journal of Vacuum Science & Technology B, 1990. **8**(6): p. 1509-1513.
12. Brady, M.J. and A. Davidson, *Correction for Chromatic Aberration in Microscope Projection Photolithography*. Review of Scientific Instruments, 1983. **54**(10): p. 1292-1295.
13. Kim, M., et al., *Addressable Micropatterning of Multiple Proteins and Cells by Microscope Projection Photolithography Based on a Protein Friendly Photoresist*. Langmuir, 2010. **26**(14): p. 12112-12118.
14. Stadler, B., et al., *Nanopatterning of gold colloids for label-free biosensing*. Nanotechnology, 2007. **18**(15).
15. Turchanin, A., et al., *Fabrication of molecular nanotemplates in self-assembled monolayers by extreme-ultraviolet-induced chemical lithography*. Small, 2007. **3**(12): p. 2114-2119.
16. Shin, Y.M., et al., *Terahertz vacuum electronic circuits fabricated by UV lithographic molding and deep reactive ion etching*. Applied Physics Letters, 2009. **95**(18).

17. Totzeck, M., et al., *Semiconductor fabrication - Pushing deep ultraviolet lithography to its limits*. Nature Photonics, 2007. **1**(11): p. 629-631.
18. de Boor, J., et al., *Three-beam interference lithography: upgrading a Lloyd's interferometer for single-exposure hexagonal patterning*. Optics Letters, 2009. **34**(12): p. 1783-5.
19. Solak, H.H. and Y. Ekinici, *Bit-array patterns with density over 1 Tbit/in.(2) fabricated by extreme ultraviolet interference lithography*. Journal of Vacuum Science & Technology B, 2007. **25**(6): p. 2123-2126.
20. Solak, H.H., *Nanolithography with coherent extreme ultraviolet light*. Journal of Physics D-Applied Physics, 2006. **39**(10): p. R171-R188.
21. Solak, H.H., et al., *Sub-50 nm period patterns with EUV interference lithography*. Microelectronic Engineering, 2003. **67-8**: p. 56-62.
22. Xia, Y.N. and G.M. Whitesides, *Soft lithography*. Annual Review of Materials Science, 1998. **28**: p. 153-184.
23. Whitesides, G.M., et al., *Soft lithography in biology and biochemistry*. Annual Review of Biomedical Engineering, 2001. **3**: p. 335-373.
24. Zaytseva, N.V., et al., *Development of a microfluidic biosensor module for pathogen detection*. Lab on a Chip, 2005. **5**(8): p. 805-811.
25. Jiang, X., et al., *Principles of Tissue Engineering*. 3 ed. 2007, London: Academic Press.
26. Kumar, A. and G.M. Whitesides, *Features of Gold Having Micrometer to Centimeter Dimensions Can Be Formed through a Combination of Stamping with an Elastomeric Stamp and an Alkanethiol Ink Followed by Chemical Etching*. Applied Physics Letters, 1993. **63**(14): p. 2002-2004.
27. Ravoo, B.J., *Microcontact chemistry: surface reactions in nanoscale confinement*. Journal of Materials Chemistry, 2009. **19**(47): p. 8902-8906.
28. Wendeln, C. and B.J. Ravoo, *Surface Patterning by Microcontact Chemistry*. Langmuir, 2012. **28**(13): p. 5527-5538.
29. Kumar, A., et al., *The Use of Self-Assembled Monolayers and a Selective Etch to Generate Patterned Gold Features*. Journal of the American Chemical Society, 1992. **114**(23): p. 9188-9189.
30. Mrksich, M., et al., *Controlling cell attachment on contoured surfaces with self-assembled monolayers of alkanethiolates on gold*. Proceedings of the National Academy of Sciences of the United States of America, 1996. **93**(20): p. 10775-10778.
31. Chakra, E.B., et al., *Grafting of antibodies inside integrated microfluidic-microoptic devices by means of automated microcontact printing*. Sensors and Actuators B-Chemical, 2009. **140**(1): p. 278-286.
32. Das, T., et al., *Microcontact printing of Concanavalin A and its effect on mammalian cell morphology*. Journal of Colloid and Interface Science, 2007. **314**(1): p. 71-79.
33. Xia, Y.N., et al., *Microcontact Printing of Octadecylsiloxane on the Surface of Silicon Dioxide and Its Application in Microfabrication*. Journal of the American Chemical Society, 1995. **117**(37): p. 9576-9577.
34. Yoon, S.S., et al., *Direct metallization of gold patterns on polyimide substrate by microcontact printing and selective surface modification*. Microelectronic Engineering, 2008. **85**(1): p. 136-142.
35. Hynd, M.R., et al., *Directed cell growth on protein-functionalized hydrogel surfaces*. Journal of Neuroscience Methods, 2007. **162**(1-2): p. 255-263.
36. Burnham, M.R., et al., *Biological functionalization and surface micropatterning of polyacrylamide hydrogels*. Biomaterials, 2006. **27**(35): p. 5883-5891.

37. Michel, R., et al., *A novel approach to produce biologically relevant chemical patterns at the nanometer scale: Selective molecular assembly patterning combined with colloidal lithography*. Langmuir, 2002. **18**(22): p. 8580-8586.
38. Csucs, G., et al., *Microcontact printing of macromolecules with submicrometer resolution by means of polyolefin stamps*. Langmuir, 2003. **19**(15): p. 6104-6109.
39. Rolland, J.P., et al., *Solvent-resistant photocurable "liquid teflon" for microfluidic device fabrication*. Journal of the American Chemical Society, 2004. **126**(8): p. 2322-2323.
40. Pla-Roca, M., et al., *Micro/nanopatterning of proteins via contact printing using high aspect ratio PMMA stamps and NanoImprint apparatus*. Langmuir, 2007. **23**(16): p. 8614-8618.
41. Nakamatsu, K., et al., *Mechanical property evaluation of Au-coated nanospring fabricated by combination of focused-ion-beam chemical vapor deposition and sputter coating*. Journal of Vacuum Science & Technology B, 2006. **24**(6): p. 3169-3172.
42. Engler, A.J., et al., *Myotubes differentiate optimally on substrates with tissue-like stiffness: pathological implications for soft or stiff microenvironments*. Journal of Cell Biology, 2004. **166**(6): p. 877-887.
43. Feng, X.Z., et al., *Investigation of microcontact transfer of proteins from a selectively plasma treated elastomer stamp by fluorescence microscopy and force microscopy*. Analyst, 2001. **126**(7): p. 1100-1104.
44. Fiorini, G.S. and D.T. Chiu, *Disposable microfluidic devices: fabrication, function, and application*. Biotechniques, 2005. **38**(3): p. 429-446.
45. Delamarche, E., et al., *Microfluidic networks for chemical patterning of substrate: Design and application to bioassays*. Journal of the American Chemical Society, 1998. **120**(3): p. 500-508.
46. Khademhosseini, A., et al., *Microscale technologies for tissue engineering and biology*. Proceedings of the National Academy of Sciences of the United States of America, 2006. **103**(8): p. 2480-2487.
47. Ostuni, E., et al., *Patterning mammalian cells using elastomeric membranes*. Langmuir, 2000. **16**(20): p. 7811-7819.
48. Khetani, S.R. and S.N. Bhatia, *Microscale culture of human liver cells for drug development*. Nature Biotechnology, 2008. **26**(1): p. 120-126.
49. Tourovskaia, A., et al., *Micropatterns of chemisorbed cell adhesion-repellent films using oxygen plasma etching and elastomeric masks*. Langmuir, 2003. **19**(11): p. 4754-4764.
50. Wright, D., et al., *Reusable, reversibly sealable parylene membranes for cell and protein patterning*. Journal of Biomedical Materials Research Part A, 2008. **85A**(2): p. 530-538.
51. Pla-Roca, M., et al., *Addressable Nanowell Arrays Formed Using Reversibly Sealable Hybrid Elastomer-Metal Stencils*. Analytical Chemistry, 2010. **82**(9): p. 3848-3855.
52. Brugger, J., et al., *Resistless patterning of sub-micron structures by evaporation through nanostencils*. Microelectronic Engineering, 2000. **53**(1-4): p. 403-405.
53. Fostner, S., et al., *Silicon nanostencils with integrated support structures*. Microelectronic Engineering, 2010. **87**(4): p. 652-657.
54. Kolbel, M., et al., *Shadow-mask evaporation through monolayer-modified nanostencils*. Nano Letters, 2002. **2**(12): p. 1339-1343.
55. Langford, R.M. and T.X. Wang, *Fabrication of nickel nanocontacts using nanostencils and electron beam assisted SiO<sub>2</sub> deposition*. Journal of Nanoscience and Nanotechnology, 2006. **6**(8): p. 2468-2473.

56. Lee, M.H., J.Y. Lin, and T.W. Odom, *Large-Area Nanocontact Printing with Metallic Nanostencil Masks*. *Angewandte Chemie-International Edition*, 2010. **49**(17): p. 3057-3060.
57. Tan, C.P., et al., *Nanoscale Resolution, Multicomponent Biomolecular Arrays Generated By Aligned Printing With Parylene Peel-Off*. *Nano Letters*, 2010. **10**(2): p. 719-725.
58. Shin, Y.M., et al., *UV Lithography and Molding Fabrication of Ultrathick Micrometallic Structures Using a KMPR Photoresist*. *Journal of Microelectromechanical Systems*, 2010. **19**(3): p. 683-689.
59. Scotchford, C.A., et al., *Chemically patterned, metal-oxide-based surfaces produced by photolithographic techniques for studying protein- and cell-interactions. II: Protein adsorption and early cell interactions*. *Biomaterials*, 2003. **24**(7): p. 1147-1158.
60. Xue, C.Y. and K.L. Yang, *One-step UV lithography for activation of inert hydrocarbon monolayers and preparation of protein micropatterns*. *Journal of Colloid and Interface Science*, 2010. **344**(1): p. 48-53.
61. Healy, K.E., et al., *Kinetics of bone cell organization and mineralization on materials with patterned surface chemistry*. *Biomaterials*, 1996. **17**(2): p. 195-208.
62. Kleinfeld, D., K.H. Kahler, and P.E. Hockberger, *Controlled Outgrowth of Dissociated Neurons on Patterned Substrates*. *Journal of Neuroscience*, 1988. **8**(11): p. 4098-4120.
63. Christman, K.L., et al., *Submicron streptavidin patterns for protein assembly*. *Langmuir*, 2006. **22**(17): p. 7444-7450.
64. Takahashi, H., et al., *Micropatterned Thermoresponsive Polymer Brush Surfaces for Fabricating Cell Sheets with Well-Controlled Orientational Structures*. *Biomacromolecules*, 2011. **12**(5): p. 1414-1418.
65. Goudar, V.S., S. Suran, and M.M. Varma, *Photoresist functionalisation method for high-density protein microarrays using photolithography*. *Micro & Nano Letters*, 2012. **7**(6): p. 549-553.
66. Bhatnagar, P., et al., *Multiplexed Protein Patterns on a Photosensitive Hydrophilic Polymer Matrix*. *Advanced Materials*, 2010. **22**(11): p. 1242-+.
67. Bhatia, S.N., et al., *Effect of cell-cell interactions in preservation of cellular phenotype: cocultivation of hepatocytes and nonparenchymal cells*. *Faseb Journal*, 1999. **13**(14): p. 1883-1900.
68. Bhatia, S.N., et al., *Microfabrication of hepatocyte/fibroblast co-cultures: Role of homotypic cell interactions*. *Biotechnology Progress*, 1998. **14**(3): p. 378-387.
69. Bhatia, S.N., et al., *Probing heterotypic cell interactions: Hepatocyte function in microfabricated co-cultures*. *Journal of Biomaterials Science-Polymer Edition*, 1998. **9**(11): p. 1137-1160.
70. Bhatia, S.N., M.L. Yarmush, and M. Toner, *Controlling cell interactions by micropatterning in co-cultures: Hepatocytes and 3T3 fibroblasts*. *Journal of Biomedical Materials Research*, 1997. **34**(2): p. 189-199.
71. Loo, Y.L., et al., *Additive, nanoscale patterning of metal films with a stamp and a surface chemistry mediated transfer process: Applications in plastic electronics*. *Applied Physics Letters*, 2002. **81**(3): p. 562-564.
72. Lehnert, D., et al., *Cell behaviour on micropatterned substrata: limits of extracellular matrix geometry for spreading and adhesion*. *Journal of Cell Science*, 2004. **117**(1): p. 41-52.
73. Xia, Y.N., et al., *Microcontact printing of alkanethiols on copper and its application in microfabrication*. *Chemistry of Materials*, 1996. **8**(3): p. 601-&.

74. Mrksich, M. and G.M. Whitesides, *Using self-assembled monolayers to understand the interactions of man-made surfaces with proteins and cells*. Annual Review of Biophysics and Biomolecular Structure, 1996. **25**: p. 55-78.
75. Petrie, T.A., B.T. Stanley, and A.J. Garcia, *Micropatterned surfaces with controlled ligand tethering*. Journal of Biomedical Materials Research Part A, 2009. **90A**(3): p. 755-765.
76. Flynn, N.T., et al., *Long-term stability of self-assembled monolayers in biological media*. Langmuir, 2003. **19**(26): p. 10909-10915.
77. Santhanam, V. and R.P. Andres, *Microcontact printing of uniform nanoparticle arrays*. Nano Letters, 2004. **4**(1): p. 41-44.
78. Hidber, P.C., et al., *Microcontact printing of palladium colloids: Micron-scale patterning by electroless deposition of copper*. Langmuir, 1996. **12**(5): p. 1375-1380.
79. Wu, X.C., A.M. Bittner, and K. Kern, *Spatially selective electroless deposition of cobalt on oxide surfaces directed by microcontact printing of dendrimers*. Langmuir, 2002. **18**(12): p. 4984-4988.
80. Arrington, D., M. Curry, and S.C. Street, *Patterned thin films of polyamidoamine dendrimers formed using microcontact printing*. Langmuir, 2002. **18**(21): p. 7788-7791.
81. Lange, S.A., et al., *Microcontact printing of DNA molecules*. Analytical Chemistry, 2004. **76**(6): p. 1641-1647.
82. Galeotti, F., et al., *Breath figures-mediated microprinting allows for versatile applications in molecular biology*. European Polymer Journal, 2009. **45**(11): p. 3027-3034.
83. Hovis, J.S. and S.G. Boxer, *Patterning and composition arrays of supported lipid bilayers by microcontact printing*. Langmuir, 2001. **17**(11): p. 3400-3405.
84. Bernard, A., et al., *Printing patterns of proteins*. Langmuir, 1998. **14**(9): p. 2225-2229.
85. Hannachi, I.E., et al., *Fabrication of transferable micropatterned-co-cultured cell sheets with microcontact printing*. Biomaterials, 2009. **30**(29): p. 5427-5432.
86. Pan, C.J. and Y.D. Nie, *Microcontact printing of BMP-2 and its effect on human chondrocytes behavior*. Applied Surface Science, 2010. **256**(6): p. 1878-1882.
87. Von Philipsborn, A.C., et al., *Microcontact printing of axon guidance molecules for generation of graded patterns*. Nature Protocols, 2006. **1**(3): p. 1322-1328.
88. Stevens, M.M., et al., *Direct patterning of mammalian cells onto porous tissue engineering substrates using agarose stamps*. Biomaterials, 2005. **26**(36): p. 7636-7641.
89. Schulte, V.A., et al., *A hydrophobic perfluoropolyether elastomer as a patternable biomaterial for cell culture and tissue engineering*. Biomaterials, 2010. **31**(33): p. 8583-8595.
90. Tien, J., C.M. Nelson, and C.S. Chen, *Fabrication of aligned microstructures with a single elastomeric stamp*. Proceedings of the National Academy of Sciences of the United States of America, 2002. **99**(4): p. 1758-1762.
91. Dickinson, L.E., et al., *Patterning microscale extracellular matrices to study endothelial and cancer cell interactions in vitro*. Lab on a Chip, 2012. **12**(21): p. 4244-4248.
92. Hudalla, G.A. and W.L. Murphy, *Chemically well-defined self-assembled monolayers for cell culture: toward mimicking the natural ECM*. Soft Matter, 2011. **7**(20): p. 9561-9571.

93. Koepsel, J.T. and W.L. Murphy, *Patterning Discrete Stem Cell Culture Environments via Localized Self-Assembled Monolayer Replacement*. Langmuir, 2009. **25**(21): p. 12825-12834.
94. Lamb, B.M., et al., *Microfluidic lithography of SAMs on gold to create dynamic surfaces for directed cell migration and contiguous cell cocultures*. Langmuir, 2008. **24**(16): p. 8885-8889.
95. Lovchik, R., et al., *Cellular microarrays for use with capillary-driven microfluidics*. Analytical and Bioanalytical Chemistry, 2008. **390**(3): p. 801-808.
96. Delamarche, E., et al., *Patterned delivery of immunoglobulins to surfaces using microfluidic networks*. Science, 1997. **276**(5313): p. 779-781.
97. Khademhosseini, A., et al., *Cell docking inside microwells within reversibly sealed microfluidic channels for fabricating multiphenotype cell arrays*. Lab on a Chip, 2005. **5**(12): p. 1380-1386.
98. Chiu, D.T., et al., *Patterned deposition of cells and proteins onto surfaces by using three-dimensional microfluidic systems*. Proceedings of the National Academy of Sciences of the United States of America, 2000. **97**(6): p. 2408-2413.
99. Lee, S.H., et al., *Capillary Based Patterning of Cellular Communities in Laterally Open Channels*. Analytical Chemistry, 2010. **82**(7): p. 2900-2906.
100. Torisawa, Y.S., et al., *Microfluidic hydrodynamic cellular patterning for systematic formation of co-culture spheroids*. Integrative Biology, 2009. **1**(11-12): p. 649-654.
101. Kim, G., B. Kim, and J. Brugger, *All-photoplastic microstencil with self-alignment for multiple layer shadow-mask patterning*. Sensors and Actuators a-Physical, 2003. **107**(2): p. 132-136.
102. Folch, A., et al., *Microfabricated elastomeric stencils for micropatterning cell cultures*. Journal of Biomedical Materials Research, 2000. **52**(2): p. 346-353.
103. Wright, D., et al., *Generation of static and dynamic patterned co-cultures using microfabricated parylene-C stencils*. Lab on a Chip, 2007. **7**(10): p. 1272-1279.
104. Kolodziej, C.M. and H.D. Maynard, *Electron-Beam Lithography for Patterning Biomolecules at the Micron and Nanometer Scale*. Chemistry of Materials, 2012. **24**(5): p. 774-780.
105. Mendes, P.M., C.L. Yeung, and J.A. Preece, *Bio-nanopatterning of surfaces*. Nanoscale Research Letters, 2007. **2**(8): p. 373-384.
106. Whelan, C.S., et al., *Improved electron-beam patterning of Si with self-assembled monolayers*. Applied Physics Letters, 1996. **69**(27): p. 4245-4247.
107. Golzhauser, A., et al., *Nanoscale patterning of self-assembled monolayers with electrons*. Journal of Vacuum Science & Technology B, 2000. **18**(6): p. 3414-3418.
108. Eck, W., et al., *Generation of surface amino groups on aromatic self-assembled monolayers by low energy electron beams - A first step towards chemical lithography*. Advanced Materials, 2000. **12**(11): p. 805-808.
109. Geyer, W., et al., *Electron induced chemical nanolithography with self-assembled monolayers*. Journal of Vacuum Science & Technology B, 2001. **19**(6): p. 2732-2735.
110. Schmelmer, U., et al., *Surface-initiated polymerization on self-assembled monolayers: Amplification of patterns on the micrometer and nanometer scale*. Angewandte Chemie-International Edition, 2003. **42**(5): p. 559-+.
111. Kuller, A., et al., *Nanostructuring of silicon by electron-beam lithography of self-assembled hydroxybiphenyl monolayers*. Applied Physics Letters, 2003. **82**(21): p. 3776-3778.
112. He, Q., et al., *Fabrication of controlled thermosensitive polymer nanopatterns with one-pot polymerization through chemical lithography*. Small, 2007. **3**(11): p. 1860-1865.

113. Ballav, N., S. Schilp, and M. Zharnikov, *Electron-beam chemical lithography with aliphatic self-assembled monolayers*. Angewandte Chemie-International Edition, 2008. **47**(8): p. 1421-1424.
114. Schilp, S., N. Ballav, and M. Zharnikov, *Fabrication of a full-coverage polymer nanobrush on an electron-beam-activated template*. Angewandte Chemie-International Edition, 2008. **47**(36): p. 6786-6789.
115. Binnig, G., et al., *Surface Studies by Scanning Tunneling Microscopy*. Physical Review Letters, 1982. **49**(1): p. 57-61.
116. Binnig, G., C.F. Quate, and C. Gerber, *Atomic Force Microscope*. Physical Review Letters, 1986. **56**(9): p. 930-933.
117. Eigler, D.M. and E.K. Schweizer, *Positioning Single Atoms with a Scanning Tunneling Microscope*. Nature, 1990. **344**(6266): p. 524-526.
118. Ross, C.B., L. Sun, and R.M. Crooks, *Scanning Probe Lithography .I. Scanning Tunneling Microscope Induced Lithography of Self-Assembled N-Alkanethiol Monolayer Resists*. Langmuir, 1993. **9**(3): p. 632-636.
119. Liu, G.Y. and M.B. Salmeron, *Reversible Displacement of Chemisorbed N-Alkanethiol Molecules on Au(111) Surface - an Atomic-Force Microscopy Study*. Langmuir, 1994. **10**(2): p. 367-370.
120. Wadu-Mesthrige, K., et al., *Fabrication and imaging of nanometer-sized protein patterns*. Langmuir, 1999. **15**(25): p. 8580-8583.
121. Choi, I., Y. Kim, and J. Yi, *Fabrication of hierarchical micro/nanostructures via scanning probe lithography and wet chemical etching*. Ultramicroscopy, 2008. **108**(10): p. 1205-1209.
122. Kim, S., K.D. Kihm, and T. Thundat, *Fluidic applications for atomic force microscopy (AFM) with microcantilever sensors*. Experiments in Fluids, 2010. **48**(5): p. 721-736.
123. Custance, O., R. Perez, and S. Morita, *Atomic force microscopy as a tool for atom manipulation*. Nature Nanotechnology, 2009. **4**(12): p. 803-810.
124. Piner, R.D., et al., *"Dip-pen" nanolithography*. Science, 1999. **283**(5402): p. 661-663.
125. Rosa, L.G. and J. Liang, *Atomic force microscope nanolithography: dip-pen, nanoshaving, nanografting, tapping mode, electrochemical and thermal nanolithography*. Journal of Physics-Condensed Matter, 2009. **21**(48).
126. Wilson, D.L., et al., *Surface organization and nanopatterning of collagen by dip-pen nanolithography*. Proceedings of the National Academy of Sciences of the United States of America, 2001. **98**(24): p. 13660-13664.
127. Agarwal, G., et al., *Dip-pen nanolithography in tapping mode*. Journal of the American Chemical Society, 2003. **125**(2): p. 580-583.
128. Ginger, D.S., H. Zhang, and C.A. Mirkin, *The evolution of dip-pen nanolithography*. Angewandte Chemie-International Edition, 2004. **43**(1): p. 30-45.
129. Salaita, K., Y.H. Wang, and C.A. Mirkin, *Applications of dip-pen nanolithography*. Nature Nanotechnology, 2007. **2**(3): p. 145-155.
130. Wu, C.C., et al., *Strategies for Patterning Biomolecules with Dip-Pen Nanolithography*. Small, 2011. **7**(8): p. 989-1002.
131. Braunschweig, A.B., F.W. Huo, and C.A. Mirkin, *Molecular printing*. Nature Chemistry, 2009. **1**(5): p. 353-358.
132. Zhang, G.J., et al., *Nanoscale patterning of protein using electron beam lithography of organosilane self-assembled monolayers*. Small, 2005. **1**(8-9): p. 833-837.
133. Mendes, P.M., et al., *Gold nanoparticle patterning of silicon wafers using chemical e-beam lithography*. Langmuir, 2004. **20**(9): p. 3766-3768.

134. Lussi, J.W., et al., *Selective molecular assembly patterning at the nanoscale: a novel platform for producing protein patterns by electron-beam lithography on SiO<sub>2</sub>/indium tin oxide-coated glass substrates*. *Nanotechnology*, 2005. **16**(9): p. 1781-1786.
135. Nakamatsu, K., K. Tone, and S. Matsui, *Room-temperature nanoimprint lithography using photosensitive dry film*. *Japanese Journal of Applied Physics Part 1-Regular Papers Brief Communications & Review Papers*, 2006. **45**(5A): p. 4290-4292.
136. Hong, Y., P. Krsko, and M. Libera, *Protein surface patterning using nanoscale PEG hydrogels*. *Langmuir*, 2004. **20**(25): p. 11123-11126.
137. Hu, W.C., et al., *High-resolution electron beam lithography and DNA nanopatterning for molecular QCA*. *Ieee Transactions on Nanotechnology*, 2005. **4**(3): p. 312-316.
138. Pesen, D., et al., *Electron beam patterning of fibronectin nanodots that support focal adhesion formation*. *Soft Matter*, 2007. **3**(10): p. 1280-1284.
139. Rundqvist, J., et al., *High fidelity functional patterns of an extracellular matrix protein by electron beam-based inactivation*. *Journal of the American Chemical Society*, 2007. **129**(1): p. 59-67.
140. Christman, K.L., et al., *Nanoscale Growth Factor Patterns by Immobilization on a Heparin-Mimicking Polymer*. *Journal of the American Chemical Society*, 2008. **130**(49): p. 16585-16591.
141. Hatakeyama, H., et al., *Patterned biofunctional designs of thermoresponsive surfaces for spatiotemporally controlled cell adhesion, growth, and thermally induced detachment*. *Biomaterials*, 2007. **28**(25): p. 3632-3643.
142. Dos Reis, G., et al., *Direct Microfabrication of Topographical and Chemical Cues for the Guided Growth of Neural Cell Networks on Polyamidoamine Hydrogels*. *Macromolecular Bioscience*, 2010. **10**(8): p. 842-852.
143. Golzhauser, A., et al., *Chemical nanolithography with electron beams*. *Advanced Materials*, 2001. **13**(11): p. 806-+.
144. He, Q., et al., *Fabrication of thermosensitive polymer nanopatterns through chemical lithography and atom transfer radical polymerization*. *Langmuir*, 2007. **23**(7): p. 3981-3987.
145. Steenackers, M., et al., *Morphology control of structured polymer brushes*. *Small*, 2007. **3**(10): p. 1764-1773.
146. He, Q., et al., *Self-assembled molecular pattern by chemical lithography and interfacial chemical reactions*. *Journal of Nanoscience and Nanotechnology*, 2006. **6**(6): p. 1838-1841.
147. Xu, L.S. and D.R. Allee, *Ambient scanning tunneling lithography of Langmuir-Blodgett and self-assembled monolayers*. *Journal of Vacuum Science & Technology B*, 1995. **13**(6): p. 2837-2840.
148. Bano, F., et al., *Toward Multiprotein Nanoarrays Using Nanografting and DNA Directed Immobilization of Proteins*. *Nano Letters*, 2009. **9**(7): p. 2614-2618.
149. Lee, M.V., et al., *Nanografting of silanes on silicon dioxide with applications to DNA localization and copper electroless deposition*. *Chemistry of Materials*, 2007. **19**(21): p. 5052-5054.
150. Tinazli, A., et al., *Native protein nanolithography that can write, read and erase*. *Nature Nanotechnology*, 2007. **2**(4): p. 220-225.
151. Shi, J.J., J.X. Chen, and P.S. Cremer, *Sub-100 nm Patterning of supported bilayers by nanoshaving lithography*. *Journal of the American Chemical Society*, 2008. **130**(9): p. 2718-+.

152. Cheung, C.L., et al., *Fabrication of assembled virus nanostructures on templates of chemoselective linkers formed by scanning probe nanolithography*. Journal of the American Chemical Society, 2003. **125**(23): p. 6848-6849.
153. Curran, J.M., et al., *Introducing dip pen nanolithography as a tool for controlling stem cell behaviour: unlocking the potential of the next generation of smart materials in regenerative medicine*. Lab on a Chip, 2010. **10**(13): p. 1662-1670.
154. Demers, L.M., et al., *Direct patterning of modified oligonucleotides on metals and insulators by dip-pen nanolithography*. Science, 2002. **296**(5574): p. 1836-1838.
155. Sekula, S., et al., *Multiplexed Lipid Dip-Pen Nanolithography on Subcellular Scales for the Templating of Functional Proteins and Cell Culture*. Small, 2008. **4**(10): p. 1785-1793.
156. Lim, J.H., et al., *Direct-write dip-pen nanolithography of proteins on modified silicon oxide surfaces*. Angewandte Chemie-International Edition, 2003. **42**(20): p. 2309-2312.
157. Li, B., et al., *Fabricating protein nanopatterns on a single DNA molecule with Dip-pen nanolithography*. Ultramicroscopy, 2005. **105**(1-4): p. 312-315.
158. Geyer, F.L., et al., *Superhydrophobic-Superhydrophilic Micropatterning: Towards Genome-on-a-Chip Cell Microarrays*. Angewandte Chemie-International Edition, 2011. **50**(36): p. 8424-8427.
159. Zahner, D., et al., *A Facile Approach to Superhydrophilic-Superhydrophobic Patterns in Porous Polymer Films*. Advanced Materials, 2011. **23**(27): p. 3030-+.
160. Levkin, P.A., F. Svec, and J.M.J. Frechet, *Porous Polymer Coatings: a Versatile Approach to Superhydrophobic Surfaces*. Advanced Functional Materials, 2009. **19**(12): p. 1993-1998.
161. Chen, T., I. Amin, and R. Jordan, *Patterned polymer brushes*. Chem Soc Rev, 2012. **41**(8): p. 3280-96.
162. Eeltink, S. and F. Svec, *Recent advances in the control of morphology and surface chemistry of porous polymer-based monolithic stationary phases and their application in CEC*. Electrophoresis, 2007. **28**(1-2): p. 137-147.
163. Geiser, L., et al., *Stability and repeatability of capillary columns based on porous monoliths of poly(butyl methacrylate-co-ethylene dimethacrylate)*. Journal of Chromatography A, 2007. **1140**(1-2): p. 140-146.
164. Eeltink, S., et al., *Controlling the surface chemistry and chromatography properties of methacrylate-ester-based monolithic capillary columns via photografting*. Journal of Separation Science, 2007. **30**(3): p. 407-413.
165. Yao, Z.P. and B. Ranby, *Surface Modification by Continuous Graft-Copolymerization .1. Photoinitiated Graft-Copolymerization onto Polyethylene Tape Film Surface*. Journal of Applied Polymer Science, 1990. **40**(9-10): p. 1647-1661.
166. Zhang, P.Y. and B. Ranby, *Surface Modification by Continuous Graft-Copolymerization .2. Photoinitiated Graft-Copolymerization onto Polypropylene Film Surface*. Journal of Applied Polymer Science, 1991. **43**(4): p. 621-636.
167. Yao, Z.P. and B. Ranby, *Surface Modification by Continuous Graft-Copolymerization .3. Photoinitiated Graft-Copolymerization onto Poly(Ethylene-Terephthalate) Fiber Surface*. Journal of Applied Polymer Science, 1990. **41**(7-8): p. 1459-1467.
168. Yao, Z.P. and B. Ranby, *Surface Modification by Continuous Graft-Copolymerization .4. Photoinitiated Graft-Copolymerization onto Polypropylene Fiber Surface*. Journal of Applied Polymer Science, 1990. **41**(7-8): p. 1469-1478.

169. Goda, T., et al., *Photografting of 2-methacryloyloxyethyl phosphorylcholine from polydimethylsiloxane: tunable protein repellency and lubrication property*. Colloids Surf B Biointerfaces, 2008. **63**(1): p. 64-72.
170. Delville, J., et al., *Solid state photocrosslinked starch based films: a new family of homogeneous modified starches*. Carbohydrate Polymers, 2002. **49**(1): p. 71-81.
171. Laven, P., *Simulation of rainbows, coronas, and glories by use of Mie theory*. Appl Opt, 2003. **42**(3): p. 436-44.
172. Laven, P., *How are glories formed?* Appl Opt, 2005. **44**(27): p. 5675-83.
173. Laven, P., *Atmospheric glories: simulations and observations*. Appl Opt, 2005. **44**(27): p. 5667-74.
174. Lock, J.A. and P. Laven, *Mie scattering in the time domain. Part I. The role of surface waves*. J Opt Soc Am A Opt Image Sci Vis, 2011. **28**(6): p. 1086-95.
175. Lock, J.A. and P. Laven, *Mie scattering in the time domain. Part II. The role of diffraction*. J Opt Soc Am A Opt Image Sci Vis, 2011. **28**(6): p. 1096-106.
176. Hancock, M.J., et al., *Anisotropic material synthesis by capillary flow in a fluid stripe*. Biomaterials, 2011. **32**(27): p. 6493-6504.
177. Hancock, M.J., et al., *Surface-Tension-Driven Gradient Generation in a Fluid Stripe for Bench-Top and Microwell Applications*. Small, 2011. **7**(7): p. 892-901.
178. Hancock, M.J., et al., *Designer Hydrophilic Regions Regulate Droplet Shape for Controlled Surface Patterning and 3D Microgel Synthesis*. Small, 2012. **8**(3): p. 393-403.
179. Xing, S.Y., R.S. Harake, and T.R. Pan, *Droplet-driven transports on superhydrophobic-patterned surface microfluidics*. Lab on a Chip, 2011. **11**(21): p. 3642-3648.
180. Hong, L.F. and T.R. Pan, *Surface microfluidics fabricated by photopatternable superhydrophobic nanocomposite*. Microfluidics and Nanofluidics, 2011. **10**(5): p. 991-997.
181. Jokinen, V., R. Kostianen, and T. Sikanen, *Multiphase Designer Droplets for Liquid-Liquid Extraction*. Advanced Materials, 2012. **24**(46): p. 6240-6243.
182. Jokinen, V., L. Sainiemi, and S. Franssila, *Complex droplets on chemically modified silicon nanograss*. Advanced Materials, 2008. **20**(18): p. 3453-+.
183. Mertaniemi, H., et al., *Superhydrophobic Tracks for Low-Friction, Guided Transport of Water Droplets*. Advanced Materials, 2011. **23**(26): p. 2911-+.
184. Lipowsky, R., et al., *Wetting, budding, and fusion-morphological transitions of soft surfaces*. Journal of Physics-Condensed Matter, 2005. **17**(31): p. S2885-S2902.
185. Brinkmann, M., J. Kierfeld, and R. Lipowsky, *Stability of liquid channels or filaments in the presence of line tension*. Journal of Physics-Condensed Matter, 2005. **17**(15): p. 2349-2364.
186. Lipowsky, R., et al., *Droplets, bubbles, and vesicles at chemically structured surfaces*. Journal of Physics-Condensed Matter, 2005. **17**(9): p. S537-S558.
187. Seemann, R., et al., *Wetting morphologies at microstructured surfaces*. Proceedings of the National Academy of Sciences of the United States of America, 2005. **102**(6): p. 1848-1852.
188. Lipowsky, R., *Morphological wetting transitions at chemically structured surfaces*. Current Opinion in Colloid & Interface Science, 2001. **6**(1): p. 40-48.
189. Lipowsky, R., P. Lenz, and P.S. Swain, *Wetting and dewetting of structured and imprinted surfaces*. Colloids and Surfaces a-Physicochemical and Engineering Aspects, 2000. **161**(1): p. 3-22.
190. Drelich, J., et al., *Contact angles for liquid drops at a model heterogeneous surface consisting of alternating and parallel hydrophobic hydrophilic strips*. Langmuir, 1996. **12**(7): p. 1913-1922.

191. Kim, E. and G.M. Whitesides, *Use of Minimal Free-Energy and Self-Assembly to Form Shapes*. Chemistry of Materials, 1995. **7**(6): p. 1257-1264.
192. Drelich, J., et al., *Wetting Characteristics of Liquid-Drops at Heterogeneous Surfaces*. Colloids and Surfaces a-Physicochemical and Engineering Aspects, 1994. **93**: p. 1-13.
193. Abbott, N.L., et al., *Using Finite-Element Analysis to Calculate the Shapes of Geometrically Confined Drops of Liquid on Patterned, Self-Assembled Monolayers - a New Method to Estimate Excess Interfacial Free-Energies  $\Gamma_{sv}$ - $\Gamma_{sl}$* . Journal of the American Chemical Society, 1994. **116**(1): p. 290-294.
194. Yuan, Y. and T.R. Lee, *Contact Angle and Wetting Properties*, in *Surface Science Techniques*, G. Bracco and B. Holst, Editors. 2013, Springer Berlin Heidelberg. p. 3-34.
195. Liimatainen, V., V. Sariola, and Q. Zhou, *Controlling Liquid Spreading Using Microfabricated Undercut Edges*. Advanced Materials, 2013. **25**(16): p. 2275-2278.
196. Efremov, A.N., et al., *Micropatterned superhydrophobic structures for the simultaneous culture of multiple cell types and the study of cell-cell communication*. Biomaterials, 2013. **34**(7): p. 1757-1763.
197. Zajickova, Z., J. Luna, and F. Svec, *Surface Modification of Silica-Based Monolith with Poly(Pentafluoropropyl Methacrylate) Using Single Step Photografting*. Journal of Liquid Chromatography & Related Technologies, 2010. **33**(18): p. 1640-1648.
198. Viklund, C., et al., *Monolithic, "molded", porous materials with high flow characteristics for separations, catalysis, or solid-phase chemistry: Control of porous properties during polymerization*. Chemistry of Materials, 1996. **8**(3): p. 744-750.
199. Rosenberg, J.E. and P. Flodin, *Macroporous Gels .2. Polymerization of Trimethylolpropane Trimethacrylate in Various Solvents*. Macromolecules, 1987. **20**(7): p. 1518-1522.
200. Steinke, J.H.G., I.R. Dunkin, and D.C. Sherrington, *Transparent macroporous polymer monoliths*. Macromolecules, 1996. **29**(18): p. 5826-5834.
201. Kreppenhof, K., et al., *Formation of a Polymer Surface with a Gradient of Pore Size Using a Microfluidic Chip*. Langmuir, 2013. **29**(11): p. 3797-3804.
202. Hulst, H.C.v.d., *Light scattering by small particles*. Structure of matter series. 1957, New York,: Wiley. 470 p.
203. Kerker, M., *The scattering of light, and other electromagnetic radiation*. Physical chemistry, a series of monographs, 16. 1969, New York,: Academic Press. xv, 666 p.
204. Bohren, C.F. and D.R. Huffman, *Absorption and scattering of light by small particles*. 1983, New York: Wiley. xiv, 530 p.
205. Cassie, A.B.D. and S. Baxter, *Wettability of porous surface*. Transactions of the Faraday Society, 1944. **40**: p. 546-551.
206. Wenzel, R.N., *Surface Roughness and Contact Angle*. Journal of Physical and Colloid Chemistry, 1949. **53**(9): p. 1466-1467.
207. Kaji, H., et al., *Engineering systems for the generation of patterned co-cultures for controlling cell-cell interactions*. Biochim Biophys Acta, 2011. **1810**(3): p. 239-50.
208. Baker, M., *Tissue models: a living system on a chip*. Nature, 2011. **471**(7340): p. 661-5.
209. Ghaemmaghami, A.M., et al., *Biomimetic tissues on a chip for drug discovery*. Drug Discov Today, 2012. **17**(3-4): p. 173-81.

210. Wright, D., et al., *Generation of static and dynamic patterned co-cultures using microfabricated parylene-C stencils*. Lab Chip, 2007. **7**(10): p. 1272-9.
211. Yousaf, M.N., B.T. Houseman, and M. Mrksich, *Using electroactive substrates to pattern the attachment of two different cell populations*. Proc Natl Acad Sci U S A, 2001. **98**(11): p. 5992-6.
212. Ishizaki, T., N. Saito, and O. Takai, *Correlation of Cell Adhesive Behaviors on Superhydrophobic, Superhydrophilic, and Micropatterned Superhydrophobic/Superhydrophilic Surfaces to Their Surface Chemistry*. Langmuir, 2010. **26**(11): p. 8147-8154.
213. Wang, Y., et al., *Micropatterning of living cells on a heterogeneously wetted surface*. Langmuir, 2006. **22**(19): p. 8257-62.
214. Leclair, A.M., S.S.G. Ferguson, and F. Lagugne-Labarthe, *Surface patterning using plasma-deposited fluorocarbon thin films for single-cell positioning and neural circuit arrangement*. Biomaterials, 2011. **32**(5): p. 1351-1360.
215. Yamato, M., et al., *Thermally responsive polymer-grafted surfaces facilitate patterned cell seeding and co-culture*. Biomaterials, 2002. **23**(2): p. 561-567.
216. Yamato, M., et al., *Novel patterned cell coculture utilizing thermally responsive grafted polymer surfaces*. Journal of Biomedical Materials Research, 2001. **55**(1): p. 137-140.
217. Yan, C., J.G. Sun, and J.D. Ding, *Critical areas of cell adhesion on micropatterned surfaces*. Biomaterials, 2011. **32**(16): p. 3931-3938.
218. Kim, J.D., et al., *Piezoelectric inkjet printing of polymers: Stem cell patterning on polymer substrates*. Polymer, 2010. **51**(10): p. 2147-2154.
219. Jinno, S., et al., *Microfabricated multilayer parylene-C stencils for the generation of patterned dynamic co-cultures*. J Biomed Mater Res A, 2008. **86**(1): p. 278-88.
220. Wong, A.P., et al., *Partitioning microfluidic channels with hydrogel to construct tunable 3-D cellular microenvironments*. Biomaterials, 2008. **29**(12): p. 1853-1861.
221. Song, J.W. and L.L. Munn, *Fluid forces control endothelial sprouting*. Proceedings of the National Academy of Sciences of the United States of America, 2011. **108**(37): p. 15342-15347.
222. Hui, E.E. and S.N. Bhatia, *Micromechanical control of cell-cell interactions*. Proceedings of the National Academy of Sciences of the United States of America, 2007. **104**(14): p. 5722-5726.
223. Legant, W.R., et al., *Microfabricated tissue gauges to measure and manipulate forces from 3D microtissues*. Proc Natl Acad Sci U S A, 2009. **106**(25): p. 10097-102.
224. Rettig, J.R. and A. Folch, *Large-scale single-cell trapping and imaging using microwell arrays*. Analytical Chemistry, 2005. **77**(17): p. 5628-5634.
225. Rosenthal, A., A. Macdonald, and J. Voldman, *Cell patterning chip for controlling the stem cell microenvironment*. Biomaterials, 2007. **28**(21): p. 3208-3216.
226. Hagemann, A.I. and S. Scholpp, *The Tale of the Three Brothers - Shh, Wnt, and Fgf during Development of the Thalamus*. Front Neurosci, 2012. **6**: p. 76.
227. Peukert, D., et al., *Lhx2 and Lhx9 determine neuronal differentiation and compartment in the caudal forebrain by regulating Wnt signaling*. PLoS Biol, 2011. **9**(12): p. e1001218.
228. Mattes, B., et al., *Wnt3 and Wnt3a are required for induction of the mid-diencephalic organizer in the caudal forebrain*. Neural Dev, 2012. **7**: p. 12.
229. Port, F. and K. Basler, *Wnt Trafficking: New Insights into Wnt Maturation, Secretion and Spreading*. Traffic, 2010. **11**(10): p. 1265-1271.
230. Goda, T. and K. Ishihara, *Soft contact lens biomaterials from bioinspired phospholipid polymers*. Expert Review of Medical Devices, 2006. **3**(2): p. 167-174.

231. Horak, D., et al., *Poly(2-hydroxyethyl methacrylate)-based slabs as a mouse embryonic stem cell support*. Biomaterials, 2004. **25**(22): p. 5249-5260.
232. Kubinova, S., et al., *The use of superporous Ac-CGGASIKVAVS-OH-modified PHEMA scaffolds to promote cell adhesion and the differentiation of human fetal neural precursors*. Biomaterials, 2010. **31**(23): p. 5966-5975.
233. Lumsden, A. and R. Keynes, *Segmental Patterns of Neuronal Development in the Chick Hindbrain*. Nature, 1989. **337**(6206): p. 424-428.
234. Dahmann, C., A.C. Oates, and M. Brand, *Boundary formation and maintenance in tissue development*. Nat Rev Genet, 2011. **12**(1): p. 43-55.
235. Ueda, E., et al., *Droplet Microarray: facile formation of arrays of microdroplets and hydrogel micropads for cell screening applications*. Lab on a Chip, 2012. **12**(24): p. 5218-5224.
236. Song, W.L. and J.F. Mano, *Interactions between cells or proteins and surfaces exhibiting extreme wettabilities*. Soft Matter, 2013. **9**(11): p. 2985-2999.
237. Schenck, A., et al., *The endosomal protein Appl1 mediates akt substrate specificity and cell survival in vertebrate development*. Cell, 2008. **133**(3): p. 486-497.
238. Domenichini, A., et al., *Isolation and Genetic Characterization of Mother-of-Snow-White, a Maternal Effect Allele Affecting Laterality and Lateralized Behaviors in Zebrafish*. PLoS One, 2011. **6**(10).
239. Zhou, X., et al., *Chemically Functionalized Surface Patterning*. Small, 2011. **7**(16): p. 2273-2289.
240. Liu, W.F. and C.S. Chen, *Cellular and multicellular form and function*. Adv Drug Deliv Rev, 2007. **59**(13): p. 1319-28.
241. Betancourt, T. and L. Brannon-Peppas, *Micro- and nanofabrication methods in nanotechnological medical and pharmaceutical devices*. Int J Nanomedicine, 2006. **1**(4): p. 483-95.
242. Voldman, J., M.L. Gray, and M.A. Schmidt, *Microfabrication in biology and medicine*. Annu Rev Biomed Eng, 1999. **1**: p. 401-25.
243. Hancock, M.J., et al., *Designer hydrophilic regions regulate droplet shape for controlled surface patterning and 3D microgel synthesis*. Small, 2012. **8**(3): p. 393-403.
244. Hancock, M.J., et al., *Surface-tension-driven gradient generation in a fluid stripe for bench-top and microwell applications*. Small, 2011. **7**(7): p. 892-901.
245. Gobaa, S., et al., *Artificial niche microarrays for probing single stem cell fate in high throughput*. Nat Methods, 2011. **8**(11): p. 949-55.
246. Calvert, P., *Materials science. Printing cells*. Science, 2007. **318**(5848): p. 208-9.
247. Carrilho, E., A.W. Martinez, and G.M. Whitesides, *Understanding wax printing: a simple micropatterning process for paper-based microfluidics*. Anal Chem, 2009. **81**(16): p. 7091-5.
248. Roth, E.A., et al., *Inkjet printing for high-throughput cell patterning*. Biomaterials, 2004. **25**(17): p. 3707-3715.
249. Piner, R.D., et al., *"Dip-Pen" nanolithography*. Science, 1999. **283**(5402): p. 661-3.
250. Ginger, D.S., H. Zhang, and C.A. Mirkin, *The evolution of dip-pen nanolithography*. Angew Chem Int Ed Engl, 2004. **43**(1): p. 30-45.
251. Salaita, K., Y. Wang, and C.A. Mirkin, *Applications of dip-pen nanolithography*. Nat Nanotechnol, 2007. **2**(3): p. 145-55.
252. Grier, D.G., *A revolution in optical manipulation*. Nature, 2003. **424**(6950): p. 810-816.
253. Hook, A.L., et al., *Laser-based patterning for transfected cell microarrays*. Biofabrication, 2009. **1**(4): p. 045003.

254. Deubel, M., et al., *Direct laser writing of three-dimensional photonic-crystal templates for telecommunications*. Nature Materials, 2004. **3**(7): p. 444-447.
255. Savu, V., et al., *Dynamic stencil lithography on full wafer scale*. Journal of Vacuum Science & Technology B, 2008. **26**(6): p. 2054-2058.
256. Javey, A. and H. Dai, *Regular arrays of 2 nm metal nanoparticles for deterministic synthesis of nanomaterials*. J Am Chem Soc, 2005. **127**(34): p. 11942-3.
257. Turchanin, A., et al., *Molecular self-assembly, chemical lithography, and biochemical tweezers: A path for the fabrication of functional nanometer-scale protein arrays*. Advanced Materials, 2008. **20**(3): p. 471-+.
258. Grigorescu, A.E. and C.W. Hagen, *Resists for sub-20-nm electron beam lithography with a focus on HSQ: state of the art*. Nanotechnology, 2009. **20**(29): p. 292001.
259. Waldbaur, A., et al., *Maskless Projection Lithography for the Fast and Flexible Generation of Grayscale Protein Patterns*. Small, 2012. **8**(10): p. 1570-1578.
260. Ferraro, P., et al., *Dispensing nano-pico droplets and liquid patterning by pyroelectrodynamics shooting*. Nature Nanotechnology, 2010. **5**(6): p. 429-435.
261. Tavana, H., et al., *Nanolitre liquid patterning in aqueous environments for spatially defined reagent delivery to mammalian cells*. Nature Materials, 2009. **8**(9): p. 736-741.
262. You, A.J., et al., *A miniaturized arrayed assay format for detecting small molecule-protein interactions in cells*. Chemistry & Biology, 1997. **4**(12): p. 969-975.
263. Jackman, R.J., et al., *Fabricating large arrays of microwells with arbitrary dimensions and filling them using discontinuous dewetting*. Analytical Chemistry, 1998. **70**(11): p. 2280-2287.
264. Butler, J.H., et al., *In situ synthesis of oligonucleotide arrays by using surface tension*. Journal of the American Chemical Society, 2001. **123**(37): p. 8887-8894.
265. Xia, Y.N., et al., *Template-assisted self-assembly of spherical colloids into complex and controllable structures*. Advanced Functional Materials, 2003. **13**(12): p. 907-918.
266. Rowan, S.M., M.I. Newton, and G. Mchale, *Evaporation of Microdroplets and the Wetting of Solid-Surfaces*. Journal of Physical Chemistry, 1995. **99**(35): p. 13268-13271.
267. Birdi, K.S. and D.T. Vu, *Wettability and the Evaporation Rates of Fluids from Solid-Surfaces*. Journal of Adhesion Science and Technology, 1993. **7**(6): p. 485-493.
268. Lee, C.Y. and W.K. In, *Prediction of water droplet evaporation on zircaloy surface*. Journal of Nuclear Science and Technology, 2014. **51**(4): p. 448-456.
269. Erbil, H.Y., G. McHale, and M.I. Newton, *Drop evaporation on solid surfaces: Constant contact angle mode*. Langmuir, 2002. **18**(7): p. 2636-2641.
270. Erbil, H.Y., *Evaporation of pure liquid sessile and spherical suspended drops: A review*. Advances in Colloid and Interface Science, 2012. **170**(1-2): p. 67-86.
271. Bourgesmonnier, C. and M.E.R. Shanahan, *Influence of Evaporation on Contact-Angle*. Langmuir, 1995. **11**(7): p. 2820-2829.
272. Song, H., et al., *Prediction of sessile drop evaporation considering surface wettability*. Microelectronic Engineering, 2011. **88**(11): p. 3249-3255.
273. Picknett, R.G. and R. Bexon, *Evaporation of Sessile or Pendant Drops in Still Air*. Journal of Colloid and Interface Science, 1977. **61**(2): p. 336-350.
274. Dugas, V., J. Broutin, and E. Souteyrand, *Droplet evaporation study applied to DNA chip manufacturing*. Langmuir, 2005. **21**(20): p. 9130-9136.

275. Lee, C.Y., et al., *Water droplet evaporation on Cu-based hydrophobic surfaces with nano- and micro-structures*. International Journal of Heat and Mass Transfer, 2012. **55**(7-8): p. 2151-2159.
276. Marrero, T.R. and E.A. Mason, *Gaseous diffusion coefficients*. Journal of Physical and Chemical Reference Data, 1972. **1**(1): p. 3-118.
277. Acharya, A.P., M.J. Clare-Salzler, and B.G. Keselowsky, *A high-throughput microparticle microarray platform for dendritic cell-targeting vaccines*. Biomaterials, 2009. **30**(25): p. 4168-4177.
278. Morgenthaler, S., C. Zink, and N.D. Spencer, *Surface-chemical and -morphological gradients*. Soft Matter, 2008. **4**(3): p. 419-434.
279. Kim, C., et al., *Diffusion- and convection-based activation of Wnt/beta-catenin signaling in a gradient generating microfluidic chip*. Lab Chip, 2012. **12**(24): p. 5186-94.
280. Du, Y.N., et al., *Convection-driven generation of long-range material gradients*. Biomaterials, 2010. **31**(9): p. 2686-2694.
281. Goulpeau, J., et al., *Building up longitudinal concentration gradients in shallow microchannels*. Lab on a Chip, 2007. **7**(9): p. 1154-1161.
282. Bontoux, N., et al., *Experimental characterization of hydrodynamic dispersion in shallow microchannels*. Lab on a Chip, 2006. **6**(7): p. 930-935.
283. Ajdari, A., N. Bontoux, and H.A. Stone, *Hydrodynamic dispersion in shallow microchannels: the effect of cross-sectional shape*. Analytical Chemistry, 2006. **78**(2): p. 387-392.

**Eidesstattliche Versicherung gemäß § 8 der Promotionsordnung  
der Naturwissenschaftlich-Mathematischen Gesamtfakultät  
der Universität Heidelberg**

1. Bei der eingereichten Dissertation zu dem Thema

Fabrication and application of hydrophilic-hydrophobic micropatterned polymer surfaces

handelt es sich um meine eigenständig erbrachte Leistung.

2. Ich habe nur die angegebenen Quellen und Hilfsmittel benutzt und mich keiner unzulässigen Hilfe Dritter bedient. Insbesondere habe ich wörtlich oder sinngemäß aus anderen Werken übernommene Inhalte als solche kenntlich gemacht.

3. Die Arbeit oder Teile davon habe ich wie folgt/bislang nicht<sup>1)</sup> an einer Hochschule des In- oder Auslands als Bestandteil einer Prüfungs- oder Qualifikationsleistung vorgelegt.

Titel der Arbeit:

\_\_\_\_\_  
\_\_\_\_\_

\_\_\_\_\_  
Hochschule und Jahr:

\_\_\_\_\_  
Art der Prüfungs- oder

Qualifikationsleistung: \_\_\_\_\_

4. Die Richtigkeit der vorstehenden Erklärungen bestätige ich.

5. Die Bedeutung der eidesstattlichen Versicherung und die strafrechtlichen Folgen einer unrichtigen oder unvollständigen eidesstattlichen Versicherung sind mir bekannt.

Ich versichere an Eides statt, dass ich nach bestem Wissen die reine Wahrheit erklärt und nichts verschwiegen habe.

\_\_\_\_\_  
Ort und datum

\_\_\_\_\_  
Unterschrift

<sup>1)</sup>Nicht Zutreffendes streichen. Bei Bejahung sind anzugeben: der Titel der andernorts vorgelegten Arbeit, die Hochschule, das Jahr der Vorlage und die Art der Prüfungs- oder Qualifikationsleistung.